Development of SOI-based Thermally Actuated Micromirror

by

In Sik Cho

A thesis

Presented to the University of Waterloo

In fulfilment of the degree of

Master of Applied Science

In

Electrical and Computer Engineering

Waterloo, Ontario, Canada, 2019

Author's Declaration

I hereby declare that I am the sole author of this thesis. This is a true copy of the thesis, including any required final versions, as accepted by my examiners.

I understand that my thesis may be made electronically available to the public.

In Sik Cho

Abstract

Micromirror is a Micro-Electro-Mechanical Systems (MEMS) device used to steer light by tilting or displacing a reflective surface. It is applied in numerous scanning applications and display technologies such as Light Detection And Ranging (LiDAR) and retinal scanning display. To achieve rotational or translational motion in a compliant direction with applied voltage, microactuators are implemented to a mirror. Among four commonly known principles of MEMS actuation, which are electrostatic, thermal, electromagnetic, and piezoelectric actuations, the proposed micromirror device operates based on thermal actuation, more specifically, using an Al/SiO2 bimorph structure. In this thesis, five different designs are proposed including some configurations capable of producing three degree-of-freedoms; tip, tilt, and piston motion. The proposed device also benefits from using Silicon On Insulator (SOI) wafer as a substrate as the buried oxide layer is used as an etch stop for Deep Reactive Ion Etch (DRIE) process, and the device layer enhances the flatness of the mirror surface.

In the final design, mirrors with a diameter of 500 μm consisting of silicon, aluminum, and silicon oxide with actuators made of aluminum and silicon oxide layers are developed, fabricated, and tested. The selection of the dimensions and materials are justified through simulations in response to voltage in various scenarios. Device dimensions are varied to investigate the effect of each parameter as well. In addition, the designs are simulated with other potential materials for the bimorph structure. The fabrication process is optimized to circumvent the curvature of the mirror caused by residual stress. For the final fabrication process, the device Si layer is first patterned and etched for the mirror structure. Then, Al is used as a hard mask for both frontside and backside while the frontside aluminum is also a part of the device. The silicon oxide layer on the frontside, and the handle layer on the backside are etched using Bosch process. In this research, some of the challenges are confronted and resolved during the fabrication, and these include: Al layer deposit and etch, the DRIE process, and residual stress after the release.

Finally, Scanning Electron Microscope (SEM) images of the fabricated devices are taken, and the tilt motion of the mirrors in response to actuation voltages is verified under an optical microscope. The tilt angle of the micromirrors are further investigated with a surface profiler. In conclusion, the SOI-based thermally actuated micromirror device is successfully developed with simple fabrication process while producing noticeable tilt motion with a very low actuation voltage.

Acknowledgements

I would first like to express my sincere gratitude to Professor Raafat R. Mansour for the continuous support during my time as a graduate student at the University of Waterloo. His guidance always helped me in my research and writing of this thesis and steered me in the right direction.

I am also very grateful to have worked with supportive colleagues at the Centre for Integrated RF Engineering (CIRFE). I would like to especially thank Dr. Ahmed Abdel Aziz, Tejinder, Frank, Farzard, Navjot, Geoffrey for always willing to help me for my research. Thanks to Dr. Luis Gutierrez, for maintain the cleanroom lab in a great condition, and training me with microfabrication equipment.

Furthermore, I would like to thank Dr. Eihab Abdel-Rahman and his students, Mohamed Arabi and Amr Kamel for the advice I received about the testing of my devices.

I also would like to acknowledge Quantum Nano Centre (QNC) staffs for training and providing helpful advice with issues during microfabrication.

I am very indebted to my lovely girlfriend, Jessica Ly, who has always believed in me and helped me in every way. I could not have gone through all the pressure and stress from school without her. Lastly, but not least, I am undoubtfully fortunate to have my family who has provided complete support. I cannot imagine completing my degree without my family and my girlfriend.

Dedication

To my beloved family, especially to my mother, Sang Suk Lee,

I could not have achieved this without you.

Table of Content

List of Figures

List of Tables

Chapter 1. Introduction

1.1. Motivation

In the past few decades, Micro-Electro-Mechanical Systems (MEMS) technology has matured significantly and, nowadays, is used in numerous everyday applications such as accelerometer and pressure sensors. Many inventions and advancements in microfabrication also have enabled more affordable and complex MEMS devices. As “electro-mechanical” implies, a lot of times, MEMS are used as electromechanical transducers, devices to convert a mechanical signal into an electrical one or an electrical signal into a mechanical one. The former corresponds to a sensor while the latter is an actuator.

Among various MEMS devices, micromirrors or MEMS mirrors have been researched and developed with great attention since the invention of scanning micromirror in 1980 by Petersen [1]. Micromirrors are MEMS devices used to steer light by tilting or displacing a reflective surface based on actuation mechanisms. The tilt and tip motions can manipulate the light by redirecting the light while the displacement of the mirror in a piston motion can modulate the phase of the light. There is a variety of existing successful applications of micromirrors, and future applications. Micromirrors are useful in a lot of scanning applications such as quality confocal microscopes, Light Detection And Ranging (LiDAR), additive fabrication technologies, machining applications, and non-invasive surgical procedures. In addition, a variety of display technologies, including laser scanning displays, retinal scanning displays, and stereoscopic displays, benefit with the implementation of micromirrors [2].

In general, a micromirror is integrated with MEMS actuators to achieve tilt or piston motion in a compliant direction with voltages applied. MEMS actuators can be classified into four categories by actuation principles: electrostatic, electrothermal, electromagnetic, and piezoelectric actuators. Although electromagnetic and piezoelectric actuators can provide great performance, one of the challenges with implementing electromagnetic and piezoelectric actuation is fabrication process. Micromirrors with electromagnetic actuators can often be bulky or require an external magnet, which make it more difficult to integrate on other components in microscale. Piezoelectric materials can be more expensive than standard thin-film materials. It is challenging to scale down and integrate with microdevices as well. Using electrostatic actuation is another method, and for electrostatic actuation, parallel plates and comb drives are commonly used configurations. Comb drive structures often require complicated flexure

bearings to guide their intended motions, and it is also challenging to produce vertical movement, which is typically required for a micromirror to achieve three Degree Of Freedom (DOF)s; tip, tilt, and piston. Parallel plates often suffer from pull-in effect and stiction issues during fabrication. In contrast, thermal actuators are relatively simple, and can be processed with standard materials. In particular, bimorph thermal actuators, composed of two different layers, can easily produce vertical actuation using the difference in thermal expansion of two materials. Plenty of micromirrors based on thermal actuation with great performance has been developed, however, a lot of them still have complex process steps resulting more cost and difficulty in manufacturing. One of the goals for this work is to simplify the fabrication steps while providing comparable performance.

Another significance of the micromirror device in this project is that the substrate of the device is a Silicon On Insulator (SOI). The popularity in SOI devices is increasing due to the advantage of having an oxide layer as an isolating layer. The proposed process steps also take advantage of the oxide layer as an etch stop during dry etch. Although the cost of SOI wafers is still noticeably higher than bulk silicon wafers, it is expected to decrease with time as SOI technology advances.

Considering the above challenges and potentials, this thesis proposes an SOI-based micromirror capable of producing tip, tilt, and piston motion actuated by thermal Al/SiO_2 bimorph structures. Five different designs of the micromirror are introduced with simulations. The micromirror devices are then fabricated with the proposed designs. The fabrication process is highlighted with some challenges such as residual stress and aluminum etch method, and how these issues are resolved. Finally, the angular displacement of the fabricated samples is characterized, and these experimental results are compared with the simulated results.

1.2. Objective

The primary goal of this research is to develop a micromirror device capable of three DOFs using thermal bimorph actuators. Among many aspects to achieve the objective of this project, the objective can be broken down to three main areas.

Objective 1:

Development of designs and simulations of an SOI-based micromirror device that can produce tip, tilt, and piston motion

Objective 2:

Microfabrication of a proposed micromirror device with commonly used thin-film techniques

Objective 3:

Characterization of the performance of a micromirror device to compare with simulations and other existing devices

1.3. Outline

Chapter 2:

Chapter 2 introduces useful background knowledge to understand micromirror. Four common actuation principles are highlighted and compared. Examples and applications of existing micromirrors are explored. Also, the advantages of using an SOI wafer over bulk-Si wafer are discussed.

Chapter 3:

This chapter proposes the five different designs of micromirror based on thermal bimorphs. They are compared with simulation results. In addition, the modification of these designs is detailed and reasoned. Furthermore, more simulation results are presented with dimension and material sweeps.

Chapter 4:

Following the designs from the previous chapter, the microfabrication process is described including issues in the process and the solutions to them. Moreover, the experimental setup and validation with the final devices are included in this chapter.

Chapter 5:

Lastly, a summary of the design, simulation, fabrication, and results are discussed. Then, conclusions and recommendations drawn from this study are suggested.

Chapter 2. Literature Review

This chapter introduces a literature review of the related topics to micromirrors. To understand micromirrors, the actuation mechanism must be realized. Section 2.1 covers four different mechanisms used for MEMS actuators including electrostatic, thermal, magnetic, and piezoelectric actuators.

Next, Section 2.2 classifies micromirrors and highlights examples and applications of them.

Section 2.3 introduces advantages of using SOI wafers over Si wafers. In addition, the integration of SOI technology with MEMS device is explained.

2.1. Microactuator

A microactuator or MEMS actuator is a device that converts an electrical signal into a motion. There are numerous successful applications of MEMS actuators. One of the most commercially well-known applications is ink-jet nozzle first invented in 1979 by Hewlett-Packard. Since then, attention to MEMS actuators have been growing. During the 1990s, MEMS technology has attracted great attention, and a lot of useful methods of micromachining have been developed. Nowadays, there are many applications of MEMS actuators such as micropumps, microvalves, microshutter, micromirror, microgripper, fiber-optic switch, variable capacitors in various fields like optics, communication, medical, scanning probe microscope [5]. Over the last few decades, a significant number of actuators have been developed using various methods. MEMS actuators can be classified into four categories by actuation mechanisms: electrostatic, thermal, magnetic, and piezoelectric actuations. Each category can further be grouped into subcategories as shown in Table 2.1 [6].

Table 2.1. Families and classes of microactuators [6]

Electrostatic	Thermal	Magnetic	Piezoelectric
Comb drive Scratch drive Parallel plate Inchworm Distributed Repulsive force Curved electrode S-shaped Electrostatic relay	Bimorph Solid expansion Topology optimized Shape memory alloy Fluid expansion State change	Electromagnetic Magnetostrictive External field Magnetic relay	Bimorph Expansion

Suitable actuation principle needs to be carefully considered as each has different advantages and disadvantages. The four mechanisms are shown in Table 2.2 to compare their performances [7].

Table 2.2. Comparison of different actuation principles [7]

	Electrostatic	Thermal	Magnetic	Piezoelectric
Force	Low	High	High	High
Displacement	Low	High	High	Moderately High
Actuation Voltage	High	Low	Low	Moderately Low
Power Consumption	Low	High	High	Low
Response Time	Fast	Moderately fast	Moderately fast	Fast
Fabrication Complexity	Simple	Simple	Complex	Complex
Challenge	- Pull-in effect - Stiction	- Overheating	- Fabrication challenge	- Fabrication challenge

2.1.1. Electrostatic Actuator

Electrostatic microactuators are based on an attractive force between oppositely charged conductors. This requires closely spaced gaps between the conductors. The simplest electrostatic actuator is two plates that are oppositely charged while one plate is fixed and the other is movable. As Figure 2.1 pictures the schematic of two parallel plates electrostatic actuator, the bottom plate is fixed while the top plate is moveable [8].

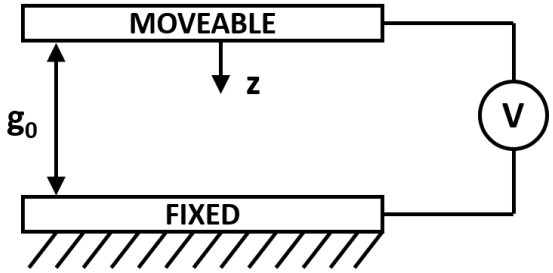

Figure 2.1. Schematic of two parallel plate electrostatic actuation

The relation between the applied voltage and the deflection of the moveable bean can be expressed by balancing the capacitive force and the mechanical spring force of the two plates. First, the energy stored, W of a capacitor is equated:

$$W = \frac{1}{2}CV^2 \tag{2.1}$$

where the capacitance, C, between two plates at a given voltage, V. The capacitance as a function of z displacement of the plates in Figure 2.1 (a) can be found:

$$C = \varepsilon \frac{A}{g_0 - z} \tag{2.2}$$

where ε, A, g_0 are permittivity of dielectric material, cross-sectional area, and the initial gap between two plates. Finally, the electrostatic force is obtained by taking the derivative of the stored energy with respect to z , which results as following [8]:

$$F_{z,electrostatic} = -\frac{dW_e}{dz} = \frac{1}{2}V^2\frac{dC}{dz} = \frac{1}{2}\varepsilon\frac{A}{(g_0 - z)^2}V^2 \tag{2.3}$$

Then, the force is balanced with the mechanical force with the spring constant of the movable structure, k:

$$F_{mechanial} + F_{electostatic} = 0 \tag{2.4}$$

$$-kz + \frac{1}{2}\varepsilon\frac{A}{(g_0 - z)^2}V^2 = 0 \tag{2.5}$$

The spring constant depends on the geometric constraints and the material properties of the moveable plate. As Equation (2.3) shows, the attractive force increases with the applied voltage, which will reduce the gap, $(g_0 - z)$, between the plates. When the gap is decreased with the actuation voltage, the reduced gap increases the attractive force. This implies that the system undergoes positive feedback and will be unstable at some point. This effect is called pull-in effect, and the calculation shows that when the gap between the two plates reaches one-third of the original gap, the pull-in occurs. Pull-in effect is typically not desired because the system becomes unstable. Therefore, the displacement of electrostatic actuator is often limited by a third of the gap, which is one of the disadvantages of electrostatic actuators. Another common issue is called stiction during microfabrication process. Often, sacrificial layer is released by wet etch, and this can cause the suspended structure to collapse due to the capillary force from the rinse liquid as shown in Figure 2.2. Stiction can be resolved by dry etching instead of wet etching, or by critical point drying after wet etch [9].

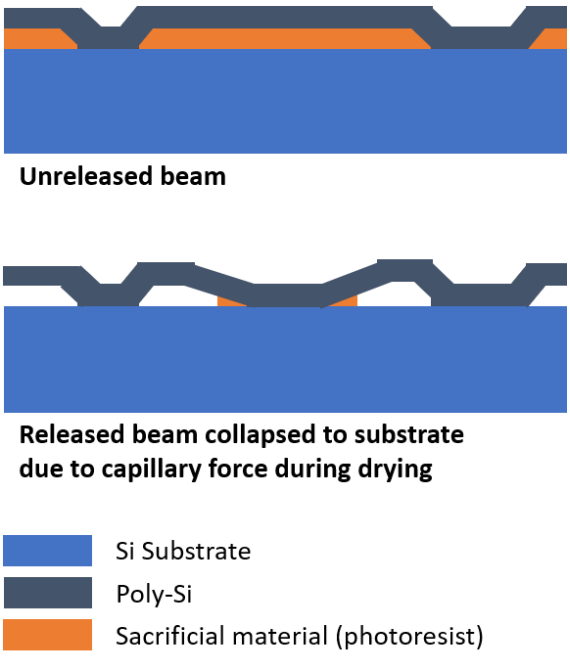

Figure 2.2. Stiction during release process

Comb-drive is another actuator design using the principle of electrostatic force. Comb-drives take an advantage of interdigitated structures to maximize the overlapping area of capacitance. Unlike two parallel plates, where the force is out-of-plane, it is easier to generate in-plane longitudinal force. Similarly, to Equation (2.2), the capacitance of each finger can be equated and used to find out the force of comb drive as following:

$$C_{finger} = \frac{\varepsilon(L_0 - y)t}{x_0} \tag{2.6}$$

$$F_y = \frac{1}{2}V^2\frac{dC}{dy} = -\frac{n\varepsilon t}{2x_0}V^2 \tag{2.7}$$

The dimensions of the structure for Equation (2.6) and (2.7) are shown in Figure 2.3(a), and t denotes the thickness of the comb drive. C_{finger} represents the capacitance between two fingers, which needs to be multiplied by the number of fingers, n. F_y is the total electrostatic force, not the force of a pair of comb fingers [10]. Note that the force is independent of the separation distance between the two comb bodies. In addition, the force can be increased with a greater number of fingers. It is also possible to produce lateral or vertical force using comb drive. Thus, comb drive, in general, can exhibit a larger range of motion than two parallel plates, and it has more feasibility of producing more degrees of freedom [11]. However, comb drive generally requires more complex geometry with flexures to direct the actuator as intended as Figure 2.3 (b) shows an example of typical comb drive actuator.

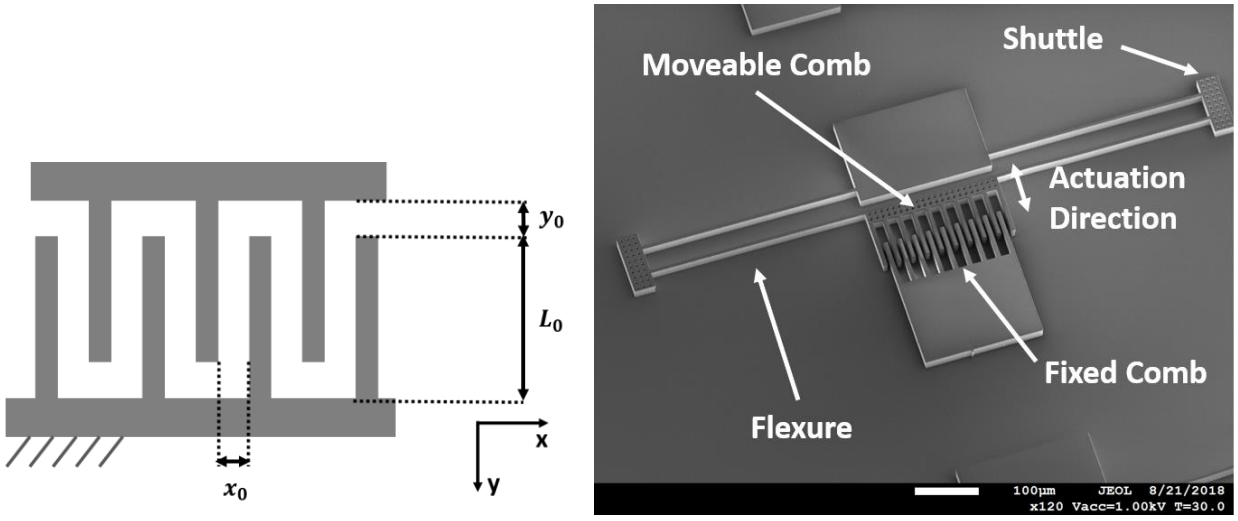

(a) (b)

Figure 2.3. (a) Schematic and parameters of comb drive (b) SEM image of a comb drive actuator

As a result, two commonly used configurations, parallel plates and comb drive structures, are introduced. As mentioned in Table 2.1, advantages of electrostatic actuators are low power operation, fast response, and simple fabrication. In contrast, the required actuation voltage is typically high. Pull-in effect needs to be addressed in some cases. Additionally, when removing the sacrificial layer for releasing, dry etch process or critical point drying is required to avoid stiction.

2.1.2. Thermal Actuator

Thermal microactuators incorporate thermal effects in MEMS elements. Although thermal effect in MEMS can cause unintended stress, deformation, or overheating, it can be used to lead to mechanical output. Several actuation methods exist such as bimorph actuation, hot arm actuation, thermopneumatic actuation, and shape memory alloy actuation. Bimorph or bimetallic actuators take advantage of different coefficient of thermal expansion (CTE) of different materials, usually involving metals. The simplest structure can be a bilayer cantilever made of two thin layers of different materials with one fixed end while the other end is movable as described in Figure 2.4 [12].

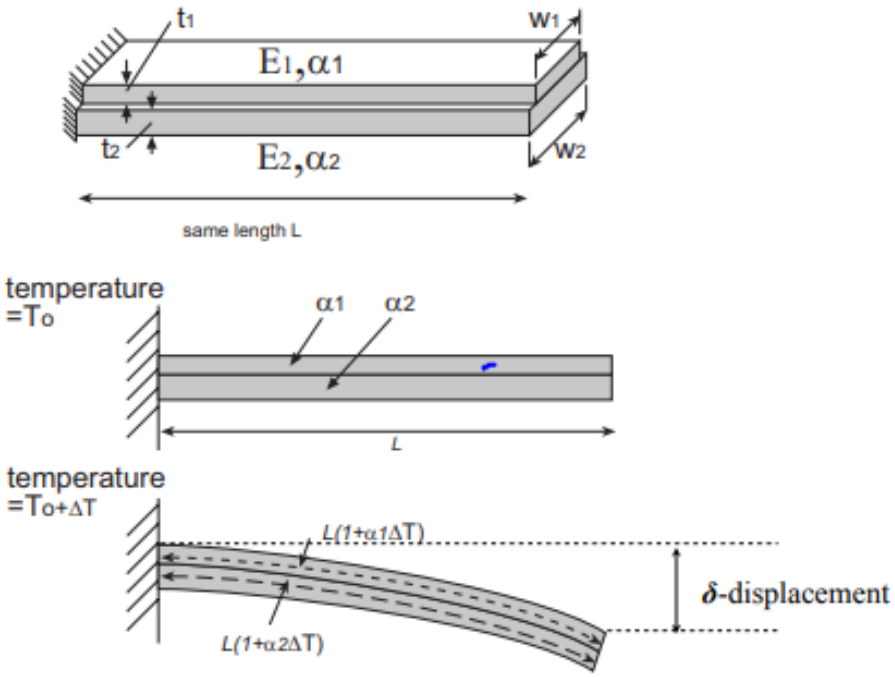

Figure 2.4. Deflection of thermal bimorph actuator [12]

The actuator is heated by resistive heating with applied voltage. Due to the difference in thermal expansion coefficient of two layers, one of them expands more than the other. This expansion leads to compressive stress on the top layer and cause the cantilever to bend. In Figure 2.4, the top layer expands more due to higher CTE and causes the beam to bend downward. Although it is possible to obtain an analytical solution of the deflection and the radius of curvature [12], the solution is quite tedious and long. In addition, the temperature difference between two layers needs to be known, which is not uniform throughout the layers. Typically, finite element analysis (FEM) software is employed to simulate more complex structures.

While bimorph actuation is generally easier to produce vertical displacement, two-hot-arm actuator is another simple design, more suitable for lateral actuation. Two-hot-arm actuation makes use of geometry by varying widths of two beams. A simple hot arm actuator has two arms with different cross-sectional areas while keeping the lengths the same. In fact, since varying thickness of a layer is more challenging, different widths can be used consisting thin arm and wide arm as presented in Figure 2.5. Unlike bimorph actuator, a single metal layer that is suspended can be used.

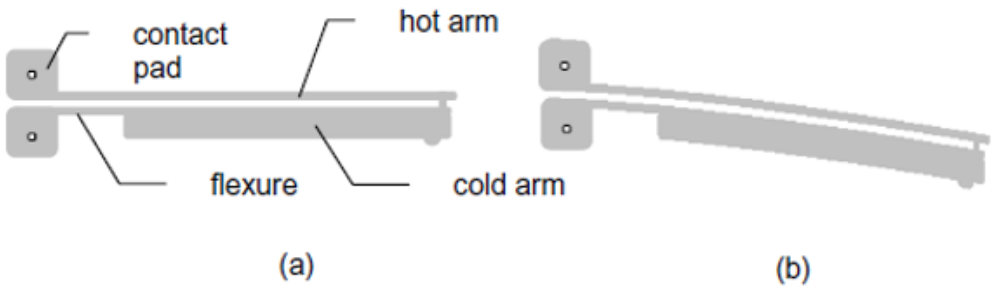

Figure 2.5. A typical two-hot-arm thermal actuator (a) Undeflected position, (b) Deflected position [13]

When current flow through beams, different cross-sectional areas result the difference in electrical resistance because electrical resistance is governed by the following equation:

$$R = \frac{\rho l}{A} \tag{2.8}$$

where R, ρ, l, and A notate electrical resistance, material resistivity, length, and cross-sectional area, respectively. When voltage is applied between the two contact pads, both arms will expand due to resistive heating. As hot arm is thinner, it produces more resistive heating for higher resistance as the name “hot arm” implies. The hot arm will expand more than the cold arm, which leads the actuator to bend towards the cold arm.

Another widely known thermal actuator design is chevron structure, which is again based on thermal expansion. The structure consists of a shuttle, which connects beams that are angled and anchored to the substrate. When current flow through the beams, the beams heat and expand, then actuate the shuttle towards the intended direction. Figure 2.6 presents the simulation of typical chevron thermal actuator made of aluminum with applied voltage of 0.1V. The simulation software used is COMSOL Multiphysics.

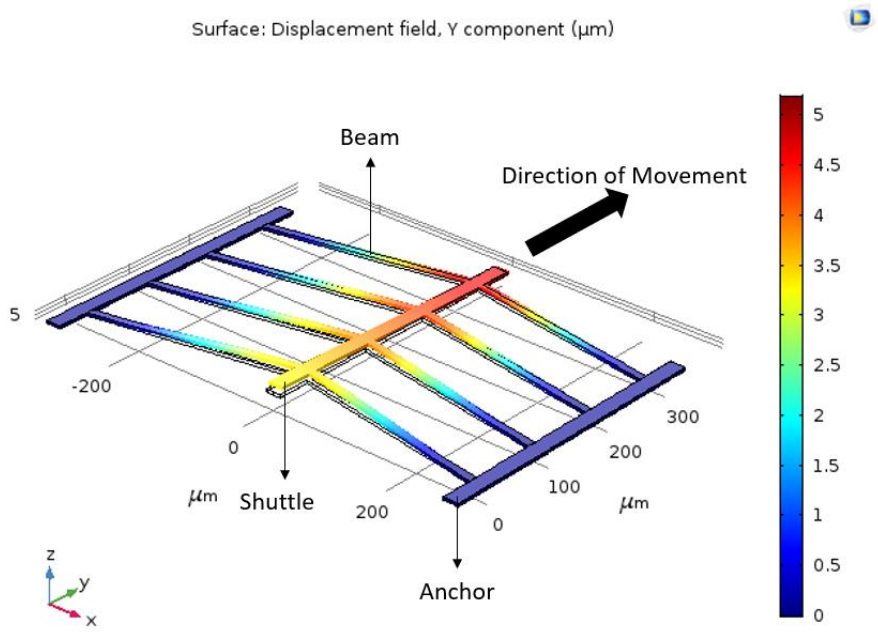

Figure 2.6. Simulation of typical chevron actuator

In conclusion, numerous configurations of thermal actuators such as two-hot-arm, chevron, bimorph structures are available with simple fabrication. Thermal actuation can generate high force and displacement with relatively low applied while the fabrication process is typically not complex. On the other hand, the response time is slower than electrostatic or piezoelectric actuators, and the power consumption is high. In addition, thermal effect should be considered to avoid melting of the device due to overheating.

2.1.3. Electromagnetic Actuator

The principle of magnetic actuation is based on the electromagnetic force, more specifically, Lorentz force, created by the interaction between magnetic fields. Lorentz force can be generated in several different ways, and typical variation of components are the following: [7]

- Interaction between permanent magnets and an external field
- Interaction between permanent magnets and current carrying conductor
- Interaction between current carrying conductor and an external field

Figure 2.7(a) and (b) both describe the interaction between permanent magnets and current carrying coils [14]. In Figure 2.7(a), current carrying conductor is movable and magnets are fixed, while in Figure 2.7(b), it is vice versa. I, B, and F_L denote current, magnetic field, and Lorentz force, respectively.

Variable reluctance (VR) force principle is another method of electromagnetic actuation and is based on the force generated to minimize the magnetic reluctance. The interaction between surfaces with different permeability produces reluctance force. For instance, as pictured in Figure 2.7(c), the movable part actuates because the normal force, F_N, is much greater than the tangential force, F_T.

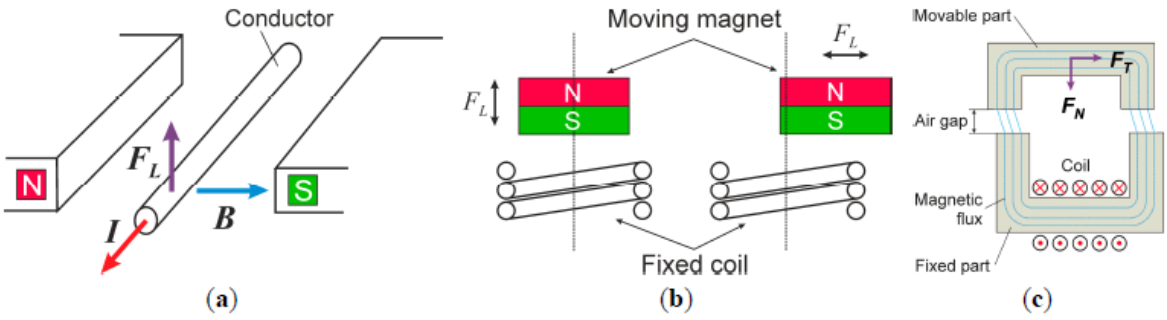

Figure 2.7. Principles of electromagnetic actuation: (a) Lorentz force on current carrying conductor with permanent magnets. (b) Lorentz force on moving magnet with current carrying conductor. (c) Variable reluctance force [14]

To understand the forces of the above configurations, The electromagnetic force density of these actuators can be obtained from the Korteweg-Helmholtz force density equation: [14]

$$\vec{f}_m = \vec{j} \times \vec{B} - \frac{1}{2} \cdot \vec{H}^2 \nabla \mu \qquad (2.9)$$

where $\vec{f}_m$ is the electromagnetic force per unit volume, $\vec{j}$ the volume current density, $\vec{B}$ the magnetic flux density, $\vec{H}$ the magnetic field intensity, and μ the magnetic permeability. The first term of the equation is responsible for the Lorentz force. In contrast, the second term corresponds to the variable reluctance force.

Often, conductive coils are used as a current carrying conductor, which interact with permanent magnets. Common designs of electromagnetic actuators with current carrying coils are presented in Figure 2.8 where I andΦ represents electric current and magnetic flux, respectively [14].

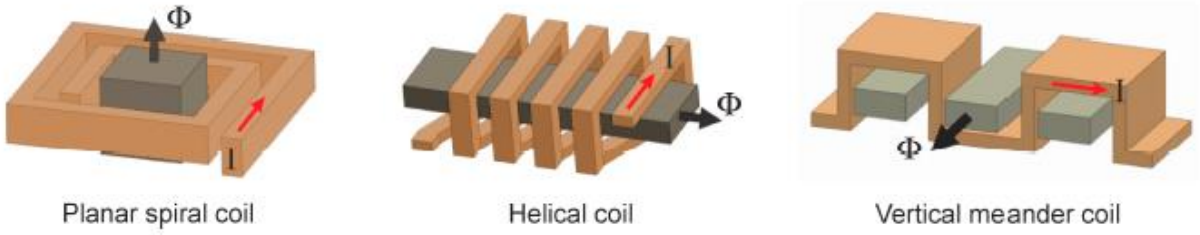

Figure 2.8. Commonly used designs of electromagnetic actuators with current conducting coils [14]

Microfabrication of electromagnetic actuator designs is quite challenging unlike the designs previously introduced for electrostatic and thermal actuators. As seen in Figure 2.8, the designs involving coils are generally bulky and complex. Another challenge is the integration of magnetic materials because high quality magnets of suitable size are often not readily available [15].

There are still several methods to integrate permanently magnetic materials in MEMS such as micromachining of bulk magnets, electro-deposition, plasma spraying, pulsed laser deposition (PLD), and sputtering. Metal-alloy-magnets are popularly used to fabricate magnetic material in MEMS as they are inexpensive and relatively simple to integrate. Commonly used metal-alloy-magnets by electro-deposition include Co-Ni-X, FePt, CoPt, CoPt, where X is usually a nonmagnetic element like P and W. In addition, SmCo and NdFeB are other magnetic materials which can be sputtered or deposited by PLD [16]. Even though the above processes and materials are available for magnetic MEMS devices, appropriate process and material must be carefully considered as they have limitations and compatibility issues. Although magnetic actuators can exhibit comparatively large displacement with a low actuation voltage, there is still a challenge in the process integration of magnetic materials.

2.1.4. Piezoelectric Actuator

Piezoelectric materials generate an electric charge from applied mechanical stress. Piezoelectric effect is reversible meaning piezoelectric materials can be applied to an actuator as well as a sensor. With the potential difference, electrically induced displacement or strain can be generated proportionally [13]. Although piezoelectric materials can transform electric charges to mechanical stress, piezoelectric structure by itself will only exhibit small motion. Once the piezoelectric material is prevented from expanding itself, a stress is generated with the voltage, which results noticeable motion. This indicates

that piezoelectric material can be effectively used as a bimorph structure similarly to a thermal bimorph introduced in Section 2.1.2. Figure 2.9. displays schematic of two types of bimorph piezoelectric [17].

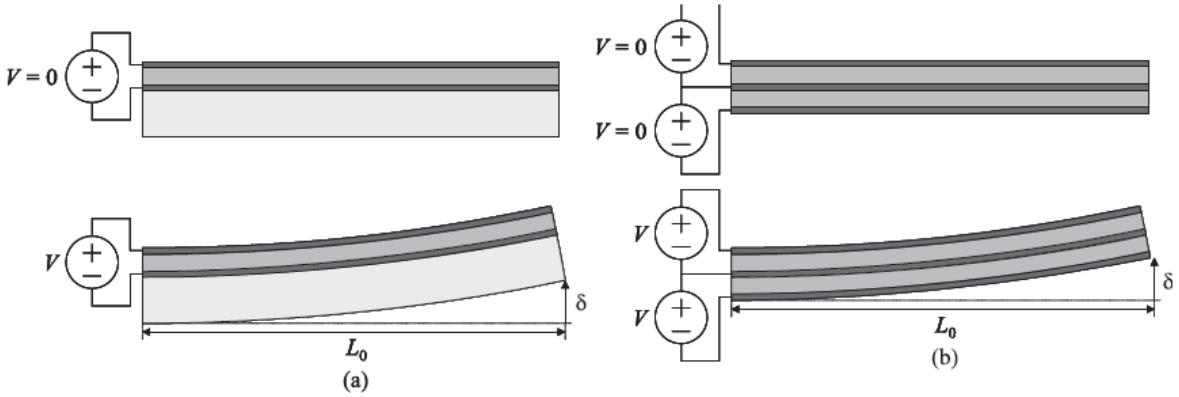

Figure 2.9. Schematic of bimorph piezoelectric actuators with one piezoelectric layer with (a) a passive mechanical layer, (b) another piezoelectric layer [17]

For passive bimorph, piezoelectric material is sandwiched between the two electrode layers, which are deposited on top of the non-piezoelectric substrate. On the other hand, active bimorph is composed of two piezoelectric material layers with oppositely induced polarization. The electrodes are mechanically insignificant as they are thin and flexible. For the case of Figure 2.9(a), assuming that the passive layer is much thicker than the piezoelectric layer, the equation for the tip deflection can be obtained using Stoney's equation. Similarly, for the active bimorph in Figure 2.9(b), with the assumption that both piezoelectric layers are the same materials with the same thickness, the tip deflection can be equated [17].

For the tip deflection of passive layer, $\delta_{passive}$,

$$\delta_{passive} = \frac{1 - v_s}{E_s} \frac{3L_0^2}{t_s^2} \sigma_{piezo} t_{piezo} \tag{2.10}$$

And for the tip deflection of active layer, δ_{active},

$$\delta_{active} = \frac{3d_{31}L_0^2}{8t^2} V \tag{2.11}$$

Where v_s, E_s, t_s refer to the Poisson ratio, Young's modulus, and thickness of the substrate, L_0 the beam length, σ_{piezo}, t_{piezo} the stress and thickness of piezoelectric layer, d_{31} piezoelectric material constant in

the unit of pC/N, t piezoelectric thickness, which is assumed to be the same for both layers, and finally V applied field. The stress in piezoelectric layer in Equation (2.8) can be obtained by [18]:

$$\sigma_{piezo} = E_s\left(e_{srain} - d_{31}E_{field} - \alpha_T \Delta T\right) \tag{2.12}$$

Where e_{strain} represents the axial strain, E_{field} the electric field, α_T, ΔT the thermal expansion coefficient and temperature variation from nominal. In Equation (2.12), the second term corresponds to the piezoelectric coupling relating z electric field to x strain. The third term is responsible for the thermal stress from thermal expansion variation. As seen in equations, several piezoelectric properties determine the deflection of the actuators. Table 2.3 lists commonly used piezoelectric materials such as zinc oxide, lead zirconate titanate (PZT), and polyvinylidene fluoride (PVDF), and their piezoelectric properties.

Table 2.3. Piezoelectric and other properties of commonly used piezoelectric materials [17]

Material	d31 [pC/N]	d33 [pC/N]	Relative Permittivity ($\varepsilon^T_{33}/\varepsilon_0$) [-]
ZnO	-4.7	12	8.2
Sol-Gel PZT	-88.7	220	1300
PVDF	-23	-35	4
PZT-5	-171	80 to 593	1700

Like electromagnetic actuators, microfabrication of piezoelectric material is one of the challenges for piezoelectric actuators. Common deposition methods of piezoelectric material are sputtering and sol-gel deposition [17]. It is also possible to bulk micromachine piezoelectric materials, which are commercially available. It is still difficult to scale down and integrate with microdevices. Even though piezoelectric actuators exhibit great performance of high force, fast switching with low power consumption, these challenges in fabrication remain.

2.2. Micromirrors

Micromirror is a MEMS device that are used to steer light, which can be applied to scanning or projecting beams. Numerous micromirrors have been successfully developed for various applications such as optics, telecommunications, astronomy, biology, and additive fabrication [2]. Micromirrors began to attract great attention in the late 1980s. The first micromirror using torsional motion with electrostatic force has been invented by K. E. Petersen in 1980 [1]. Since then, micromirrors have significantly advanced with creative designs and microfabrication technologies. Now days, one of the most known examples of

micromirror devices is perhaps Digital Micromirror Devices (DMD) created by Texas Instruments in 1987. DMD is a key technology for an application of Digital Light Projectors (DLP). DMD has an array of mirrors, which can be on and off states when electrostatic force tilts the mirror while each mirror is used as each pixel. Furthermore, DMD can be processed over CMOS architecture and the processing of the DMD structure shares many similar processes in integrated circuit (IC) fabrication [19].

2.2.1. Classifications

Typically, the surface of micromirror is designed to elastically displace in compliant directions. Degree of freedom refers to the number of compliant directions of tip, tilt and piston motion. Tip and tilt motions are rotational while piston motion is translational. A paper by Song, Y. *et al*. notates these motions as tip, tilt, and piston as presented in Figure 2.10 [2]. Micromirrors are generally designed to achieve some combination of these motions. With this classification, micromirrors can be categorized into 5 different groups: tip-tilt-piston, tip-tilt, tip-piston, tip only, and piston only.

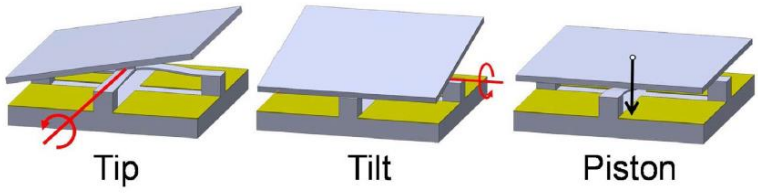

Figure 2.10. Schematic of tip, tilt, and piston motion of micromirror [2]

MEMS actuation can also be classified to three different operation modes: digital, analog, and resonant. A digital actuation utilizes a discrete set of signals, typically on and off states. DMD is a good example of micromirror array based on a digital actuation approach. On the other hand, analog actuation uses continuous and variable input to actuate mirrors. Lastly, a resonant actuation approach takes advantage of a harmonic driving signal, often at a natural frequency or a resonant frequency, to produce a large range of motion. Although the motion of the mirror can be largely amplified at a resonant frequency, the mirrors are usually limited to move with sinusoidal motions only. Micromirrors with this approach can also be used with an analog approach. The principle of actuation as discussed in Section 2.1 is obviously another classification. In conclusion, with large number of micromirrors developed, a micromirror can be grouped in different categories such as degree of freedom, actuation approach, and actuation principle.

2.2.2. Examples and Applications of Micromirrors

Four examples of micromirrors with different actuation mechanisms will be introduced. For micromirror applications, electrostatic actuation principle is the most widely used method for its advantages previously mentioned. Still, each mechanism is numerous micromirror devices developed using all these four approaches.

The first example is the resonant electrostatic micromirror for the application of reflective scanning picoproejctors, by Silva, G. *et al.* from STMicroelectronics shown in Figure 2.11 [20].

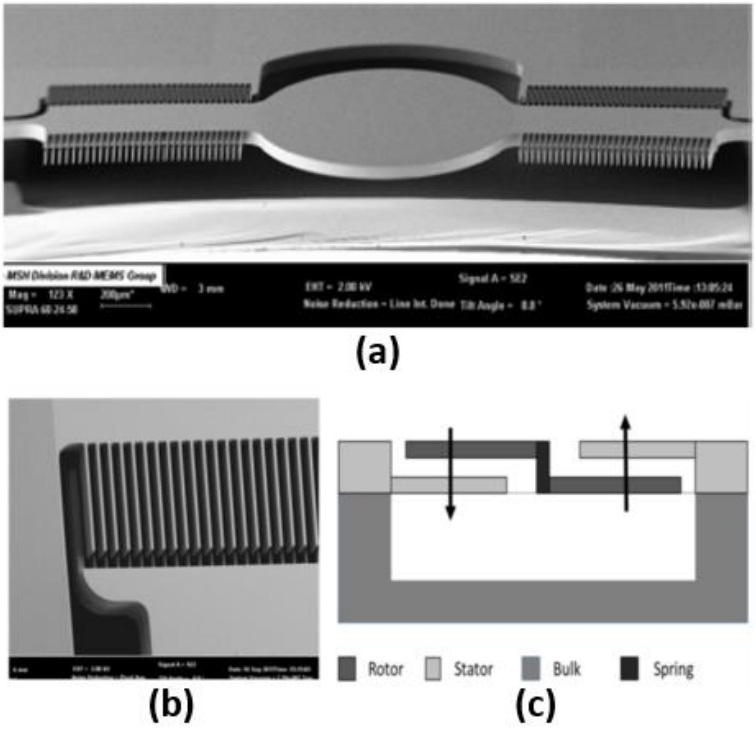

Figure 2.11. (a) SEM Images of the resonant electrostatic micromirror. (b) SEM image of comb drive of the micromirror. (c) Cross-sectional view of actuator configuration [20]

In this resonant electrostatic micromirror, comb drive structure is used at a resonant frequency to accomplish single-axis rotational motion and tip motion. The comb drive operates vertically as the two sides of fingers are offset to produce rotational motion as described in Figure 2.11 (c) [20]. This kind of structure with offset comb fingers is accomplished by wafer bonding. The author reports that the device can produce the optical scanning angle of 48° at the resonant frequency of 25 kHz with square wave of 190 V. The resonant mirror can also operate statically to provide the optical scanning angle of 36° with 200 V_{DC}.

Another example is a thermally actuated micromirror by Jia, K. *et al.* from University of Florida [21]. This paper presents tip-tilt-piston micromirror using folded dual S-shaped (FDS) bimorph with aluminum and silicon oxide. The reported optical scanning angle is 25° in both the x- and y-axes with applied voltage of V_{DC}. The schematic and the Scanning Electron Microscope (SEM) image of the devices are presented in Figure 2.12.

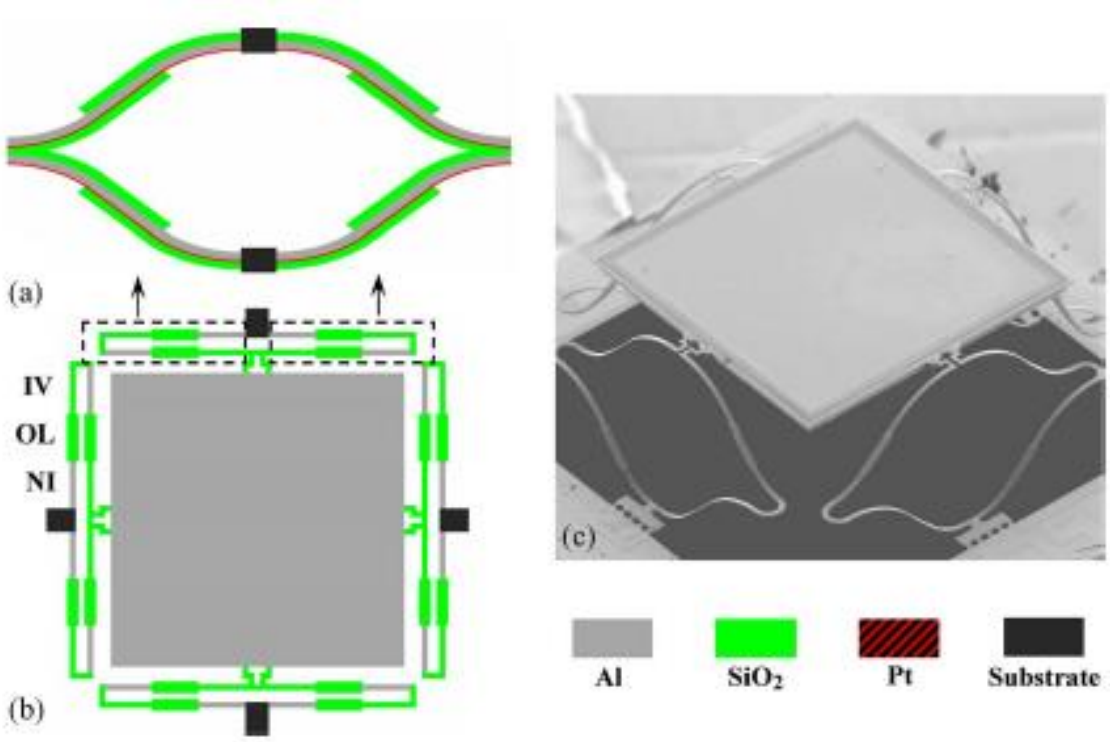

Figure 2.12. (a) Cross-sectional side view of bimorph actuator. (b) Top view of micromirror design. (c) SEM image of micromirror device [21]

Due to residual stress of thin film layers, the mirror is elevated after the fabrication. The device is also capable of piston actuation of 300 µm with 8 V_{DC}. Although in this paper, the mirror is demonstrated with a digital approach, the device can also operate at a resonant frequency as the author provides resonant characterization. The author suggests that the device is especially suitable for optical phase array applications.

It is quite challenging to create a simple design of electromagnetically actuated device in micro scale due to the requirement of magnetic field. Often, the device becomes bulky, therefore, it may be suitable to implement magnetic actuation for a large mirror. Among a few different magnetic actuation methods of introduced in Section 2.1.3, micromirror designed by Aoyagi I. *et al.* employs electromagnetic interaction

between permanent magnets and current-carrying coils similarly to the configuration in Figure 2.7(b). In this paper, the application of scanning micromirror is a laser range finder. [22] Figure 2.13 presents the top view of the layout of the micromirror and the image of the device.

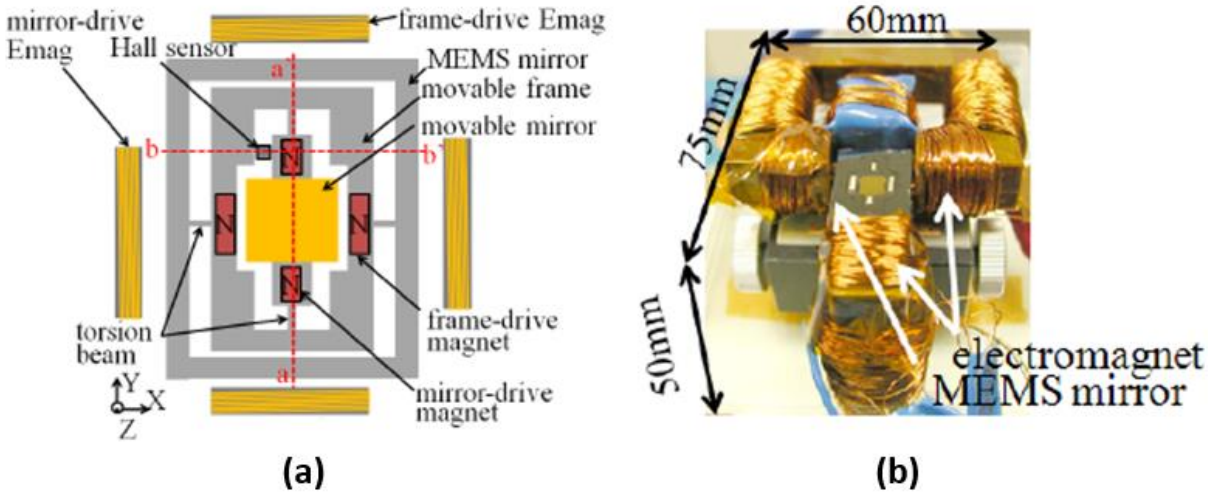

Figure 2.13. (a) Layout of micromirror device with electromagnetic actuators. (b) Image of fabricated micromirror device [22]

The interaction of magnetic field from the four permanent magnets and the alternating electric current on the four coils exhibit the Lorentz force. Figure 2.13(a) shows two frames, inner and outer, on the mirror to provide tip-tilt motion. Figure 2.13(b) suggests that the device is relatively bulky. In this paper, the permanent magnets are mounted after microfabrication. The reported optical scanning angle about X axis is 20° with applied current of 242 mA_{P-P} at 30 Hz (non-resonant mode) to the "frame-drive Emag" as labelled in Figure 2.13(a). Similarly, for scanning angle about Y axis, the optical scanning angle is 48° with 18 mA_{P-P} at 1122 Hz (resonant mode).

Last example is the micromirror device developed using piezoelectric layers to tilt the mirror by Baran, U. *et al.* [23]. Piezoelectric materials, PZT, are layered between two electrodes. The main components of the design are the inner frame, outer frame, and the mirror. The inner frame is connected to the outer frame via torsional flexures while the outer frame is anchored to the substrate. This cascaded two-frame structure can contribute to provide larger tilt angle while minimizing mirror deformation. The image of PZT based micromirror is shown in Figure 2.14.

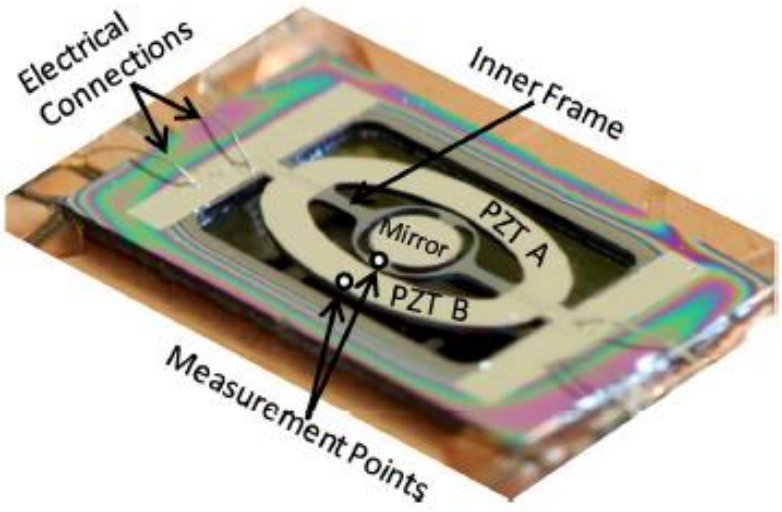

Figure 2.14. Image of micromirror device with piezoelectric actuators [23]

In this paper, the PZT layer has been deposited by sol-gel technique. The final device provides an optical scan angle of 38.5° with sinusoidal actuation voltage of 24 V at the resonance frequency of 40 kHz [23]. As seen from the examples of micromirrors in the previous section, micromirrors are mainly applied to scanning applications. The scanning or steering beam by micromirrors can be applied to a variety of technologies such as picoprojectors, optical phase arrays, laser range finders, LiDar technologies. In addition, it can also be used in multi-laser scanning to cure liquid photopolymer in 3D, steering laser beams for machining applications, noninvasive surgical applications, retinal scanning, and so on [2].

2.3. SOI MEMS Technology

SOI structure consists of silicon thin film on an insulating layer on top of silicon substrate. One of the most common materials used as an insulating layer is silicon dioxide, which is also called the buried oxide (BOX) in SOI. Recently, SOI technology has been regarded as a promising competitor of bulk-Si technology in microdevices as the use of SOI substrate can overcome some limitations of standard bulk silicon technology. The advantages of integrating SOI technology to CMOS transistor over bulk Si technology is widely known. Commonly known limitations and challenges of bulk Si technology include high leakage current, parasitic capacitance, and interference between individual devices or circuits on the same integrated substrate. The insulating layer in SOI substrate, however, inhibits these undesired effects. The insulation layer also allows applications in radiation and high temperature environment. Furthermore,

the device density can be higher due to the improved isolation between devices, which allows continuous miniaturization of devices. Lastly, the low parasitic capacitance and leakage current enables better performance at high frequency while keeping low power consumption than bulk Si devices. Numerous applications of field-effect transistors have shown SOI CMOS devices are 20% to 30% faster than bulk devices while consuming only one-third to half the power [24-26]. Figure 2.15 compares CMOS devices using bulk-Si and SOI technologies.

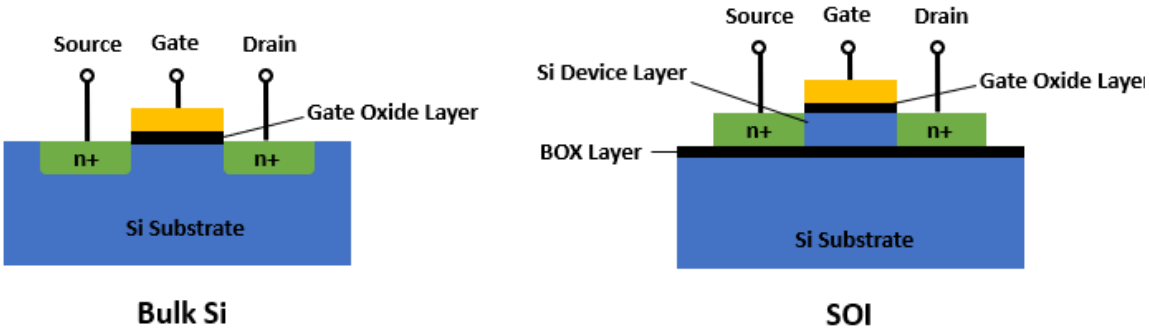

Figure 2.15. Cross section of CMOS devices using bulk Si (left) and SOI (right) technologies

SOI substrates are not only growing in IC industry, but also in MEMS industry. The market size of SOI substrates in MEMS devices has been expanding consistently and rapidly since 2000s. Figure 2.16 compares the market sizes of Si substrates and SOI substrates.

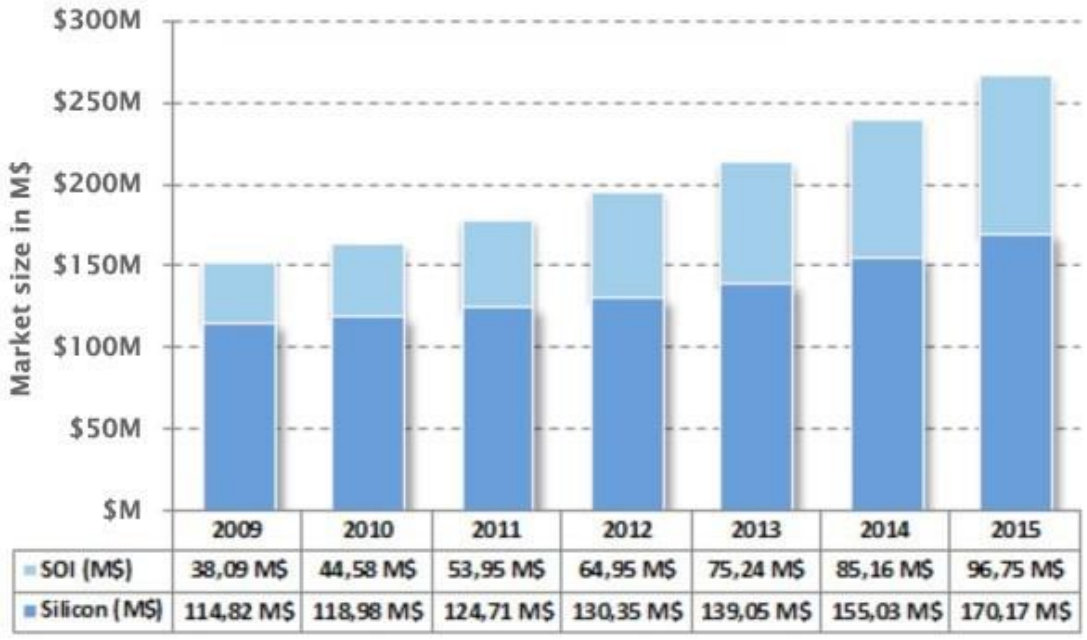

Figure 2.16. Trend of substrate market for MEMS devices [27]

SOI substrate market in MEMS technology as well as in other areas is expected to continue to expand for several reasons. One of the primary reasons is more design freedom. For example, high aspect ratio etch by Deep Reactive Ion Etch (DRIE) can be achieved with a BOX layer as an etch stop. The invention of DRIE process and the widespread availability of SOI wafers have enabled integration of SOI technology to MEMS devices [28]. Other reasons cited by other contributors for using SOI substrates for MEMS devices include the need for the smallest possible package, tight control and precision of the structure allowing well-defined and thin structures, high temperature and pressure tolerance with longer lifetime [29]. It is also possible to include additional functionalities such as pre-etched cavities, trench isolation, and/or Through Silicon Vias (TSV) on SOI substrates to simplify MEMS design and manufacturing [27].

Although one of the drawbacks of SOI technology compared to bulk Si technology is the expensive initial costs of SOI wafers, which is 3 to 4 times as costly as bulk silicon wafers, this initial cost is counterbalanced with the higher packing density and the reduction of process steps. Also, the cost of SOI wafers is expected to largely decreases as the volume of production increases over time.

In conclusion, SOI technology is emerging as a great alternative of bulk silicon technology in numerous microdevice applications. The oxide layer of SOI devices inhibits several unwanted effects in bulk silicon technology. There are countless advantages of using SOI substrates over bulk Si substrates in MEMS applications and the cost of SOI wafers is expected to reduce continuously. Therefore, SOI technology is a promising, cost-effective solution for the state-of-the-art MEMS devices.

Chapter 3. Design and Simulation of Micromirror Device

This chapter discusses the design and simulation of a thermally actuated micromirror device. Section 3.1 highlights the design of the device in detail including the material selection, design consideration, and parameters. Section 3.2 introduces the simulation results of the device using the software COMSOL. A micromirror device is mainly composed of two important structures: the mirror and the actuators. Fabrication and design of mirror are relatively straightforward as its primary requirement is to reflect to steer beam. The main challenge is to implement actuators to provide rotational and/or translational motion to the mirror. Among numerous actuation principles suggested in Section 2.1, the micromirror device presented in this thesis employs thermal bimorph actuation to accomplish tip-tilt-piston motion. Thermal bimorph, as previously mentioned, can produce large out of plane displacement using the temperature difference between the thermal coefficient constants of bilayers. The bimorph-based micromirror device is simulated with the aid of COMSOL to verify the design before fabrication.

3.1. Material Selection

Since thermal bimorph actuates using the thermal expansion of two different materials, the difference of the thermal expansion coefficient of the material is one of the most critical factors determining the performance of the actuator. The device is based on SOI wafer, and the bimorph makes use of silicon oxide layer as a bottom layer. Metal is a good candidate for a top layer as it provides enough current flow through the bimorph. Because the oxide layer has lower CTE than the metal layer, it is beneficial to have a high CTE for the metal material. Another consideration is melting temperature as the device will fail to operate and get damaged once the structure starts to melt. Considering the CTE and melting point, Table 3.1 lists the thermal properties of silicon oxide and possible metal material choices for the top layer [30-32]. In addition, Figure 3.1 compares the reflectance of various metals with respective the wavelengths.

Table 3.1. Thermal properties of silicon oxide and metals [30-32]

Material	CTE [10^{-6}]	Melting Point [°C]
SiO_2	0.56	1700
Al	23.6	660
Cr	5.94	1860
Ag	19.8	961
Au	14.2	1063
Cu	17.6	1084

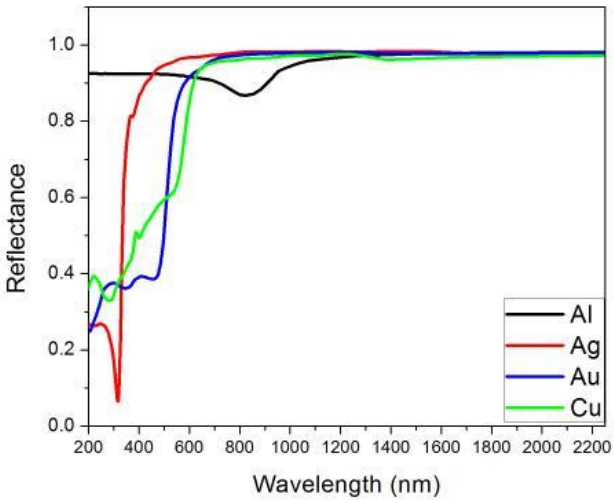

Figure 3.1. Reflectance spectra of the metals for mirror [33]

Most metal elements shown in Table 3.1 have sufficiently high coefficient of thermal expansion compared to silicon oxide. Although aluminum has the highest CTE, because it has a lower melting point, it will start to melt at lower temperature. Another consideration is fabrication feasibility. One of the most essential microfabrication processes in this work is Deep Reactive Ion Etch (DRIE) to dry etch silicon, which will be discussed in detail in Chapter 4. During the DRIE process, only certain metals are authorized to be exposed in the equipment due to the risk of chamber contamination. Among the metal elements in Table 3.1, only aluminum and chromium are allowed. Later, the actuation performance is simulated with COMSOL software for comparison. Even though chromium may be a suitable candidate for the top layer of the bimorph, for the material of the mirror, the reflectivity is critical. Figure 3.1 above suggests that aluminum is also an excellent material for the mirror [33]. Unfortunately, although not shown, the reflectivity of chromium is below 0.7 [34].

In conclusion, for the micromirror device, silicon oxide is chosen for the bottom layer of the bimorph actuator for its low CTE and its availability from the initial substrate. For the top metal layer, only few metal elements are available due to the risk of contamination during the DRIE process. Commonly used metal elements in DRIE are aluminum and chromium. Aluminum is a great candidate for the mirror material for its high reflectivity, high CTE, and process compatibility.

3.2. Initial Design and Simulation

Five different designs, labelled as A, B, C, D, and E, of the micromirror devices are considered and compared. The difference between the designs are number of anchors and beams, and the shape of the beam. In addition, the beams are curved for more deflection and higher fill factor. There is only one additional layer required on top of the SOI substrate. Figure 3.2 shows the top view of the micromirror designs, where yellow is the metal layer and blue is the silicon substrate from the handle layer. For the devices shown in Figure 3.2, only two masks are used one for the frontside and the other for the backside. The pattern of the silicon oxide layer is identical to the metal layer implying that the oxide layer is covered below the metal layer. From the backside etch, enough areas around the mirror are removed for the space when the mirror operates. The square contact pads are anchored to the substrate while all the other structures are suspended from the release of the handle layer. The dimensions of each design are listed in Table 3.2 with the corresponding parameters shown in Figure 3.3. Most dimensional parameters are the same among designs for comparison. Al and SiO_2 thickness are critical dimension for actuation performance, and for the initial design, their values are 1 μm and 2 μm, respectively.

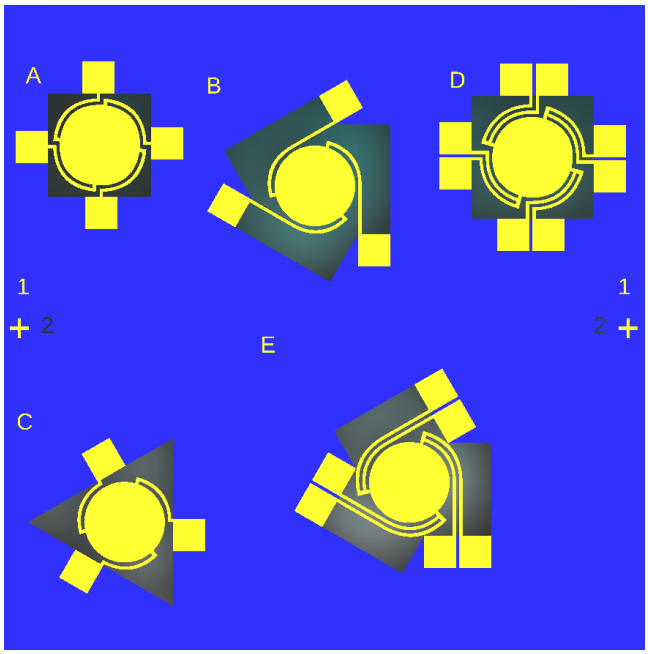

Figure 3.2. Top view of micromirror design layout

Table 3.2. Dimensions of micromirror designs

Design	Parameter	Dimension [μm]
Design A	D	500
	W	20
	L	30
	g	20
Design B	D	500
	W	20
	L	300
	g	20
Design C	D	500
	W	20
	L	30
	g	20
Design D	D	500
	W	20
	L	50
	g1 (= g2)	20
Design E	D	500
	W1 (= W2)	20
	L	330
	g1 (= g2)	20

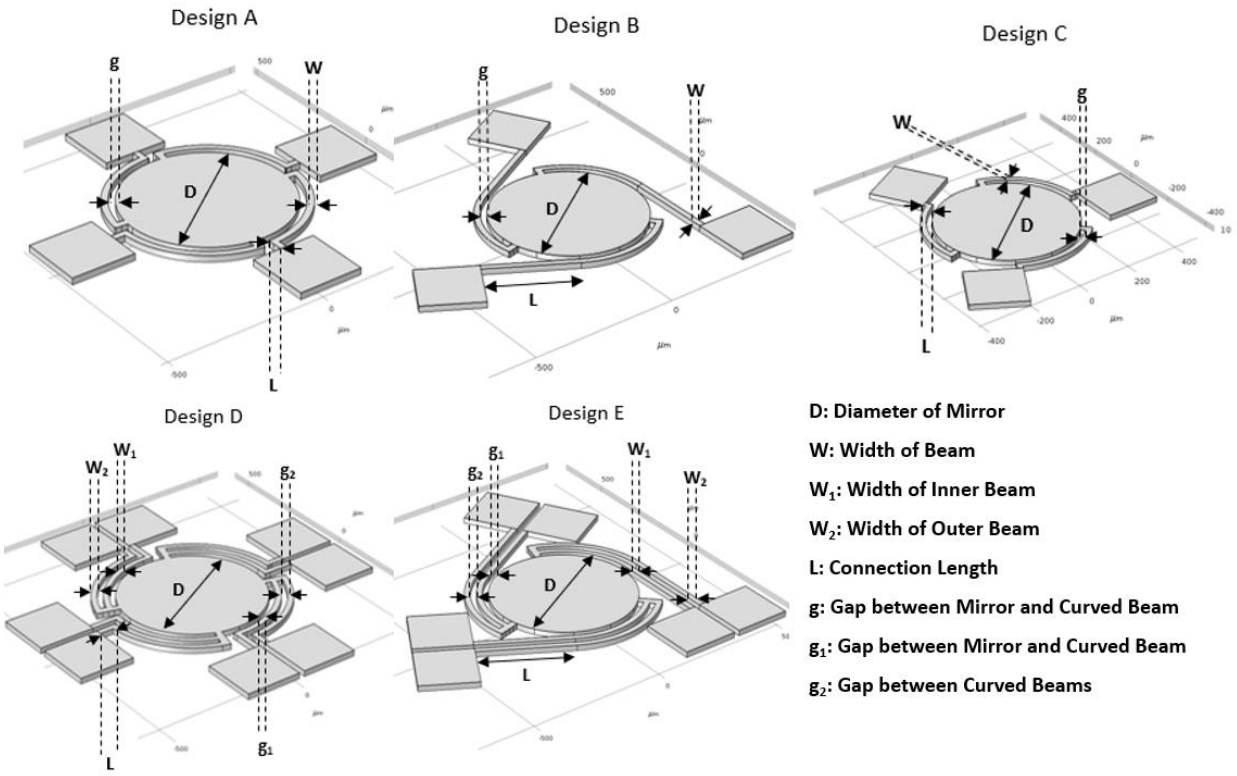

Figure 3.3 Schematic of micromirror design with dimensions parameters

The total dimension of each design including the contact pads can be found with the mask layout design in Appendix A. Using the COMSOL software, each design is simulated with the voltage applied to only one pair of contact pads. Because the simulation does not take into account the melting of the materials, one must ensure that the maximum temperature is lower than the melting point of the materials. The melting points of Al and Cr are 930 K and 2100 K, respectively. Hence, to prevent the operational failure due to melting, the maximum temperature must be marginally lower than 930 K. Using COMSOL, the designs with Al and SiO_2 bilayers are modelled. The simulated maximum temperature as a function of applied voltage of each design is plotted in Figure 3.4.

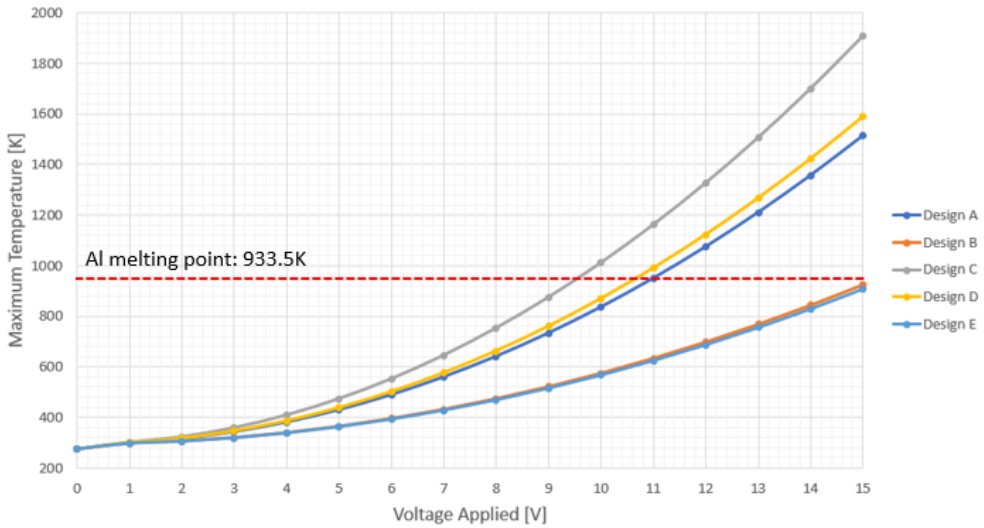

Figure 3.4. Maximum temperature as a function of applied voltage for Al/SiO2 bilayer devices

Simulation results suggest that approximately 9 volts applied to Design C will heat some part of device up to 900 K and eventually lead to melting and failure of the device. Similarly, the maximum applicable voltages can be estimated for other designs from Figure 3.4. After the microfabrication process, the Al and SiO_2 bilayer is deformed due to thermal residual stress resulting the mirror to be deformed. Therefore, the stress must be considered for the simulation. Figure 3.5 shows the simulation of designs with residual stress assuming no voltage applied.

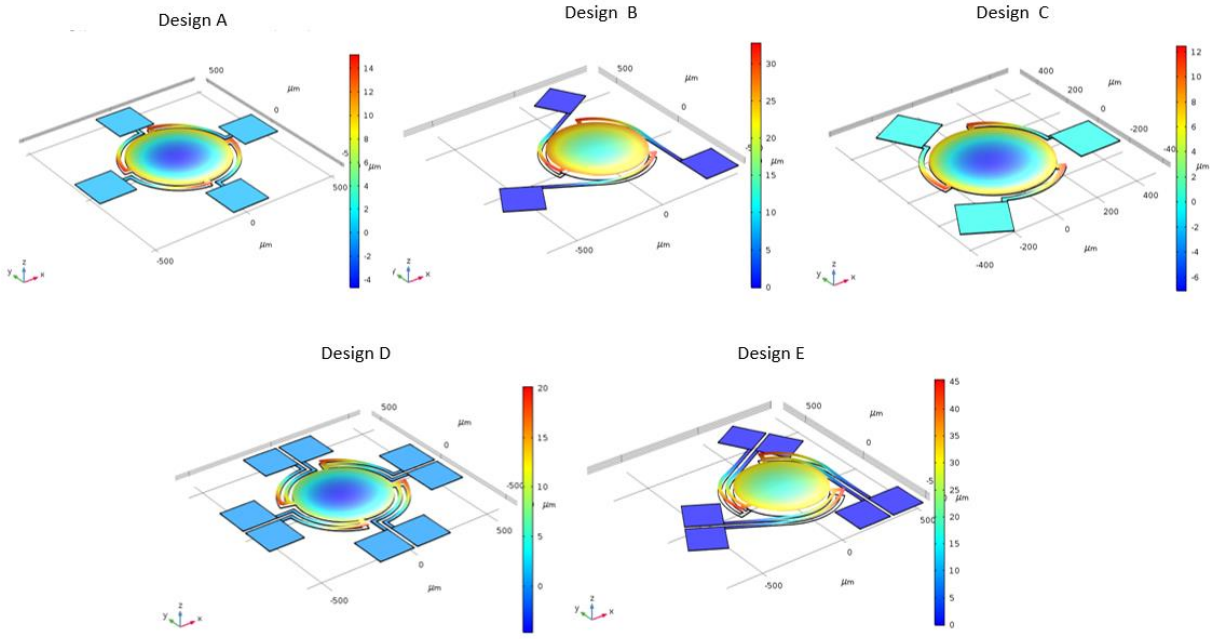

Figure 3.5. Vertical displacement of initial designs with residual stress

As seen in Figure 3.5, the mirror surfaces are curved from the thermal residual stress, which is not desired for mirrors. The device is vertically deflected up to 45 μm depending on designs. The value of the residual stress used for the simulation is chosen to be approximately 200 MPa and is also assumed to be isotropic and uniform. These values, however, will be different from the actual devices and can only be obtained experimentally. The residual stress significantly depends on process conditions and vary within a wafer as well. The issues with thermal residual stress will be revisited in Chapter 4. To evaluate the tilt degree of the mirror of each design, the models are similarly simulated, but with voltages as shown in Figure 3.6.

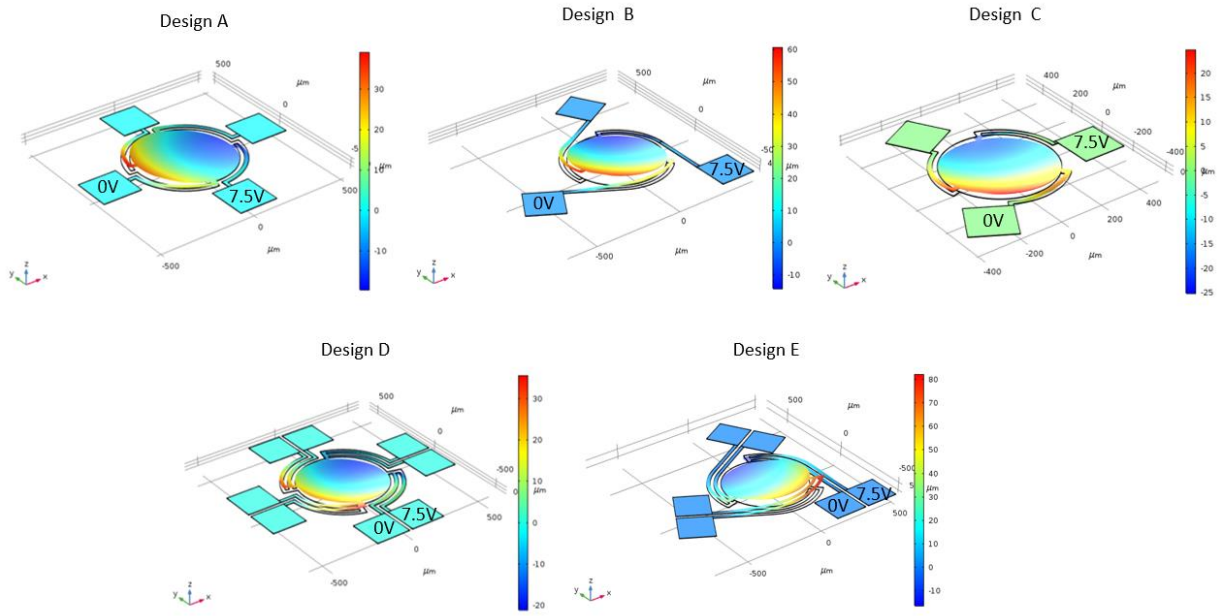

Figure 3.6 Vertical displacement of initial designs with residual stress and voltage applied

In Figure 3.6, 7.5 volts are applied between two contact pads as indicated, and the mirror tilts accordingly. Although higher voltage can be applied, it is kept as 7.5 V_{DC} for comparison and to avoid melting with some margins. Nevertheless, these devices are not applicable for micromirrors because the surfaces of the mirrors are not flat. This deformation makes the reflection of the beam unpredictable. Therefore, the simulation results of the initial designs suggest that the mirrors will not remain flat. The designs need to be modified so that the mirrors are still flat while the beams provide enough actuation for the tilt.

3.3. Modified Design and Simulation

To address the issue of the curved surface of the mirror, a silicon layer is added to the mirror. The Si device layer from SOI substrate is used as the additional layer. The silicon layer should be thick enough to prevent the curvature of the mirror from the stress. The modified designs include 20 μm of silicon layer between the oxide and the metal layer for the mirror structure. In Figure 3.7, these are again simulated with residual stress and without voltage applied similarly to Figure 3.5.

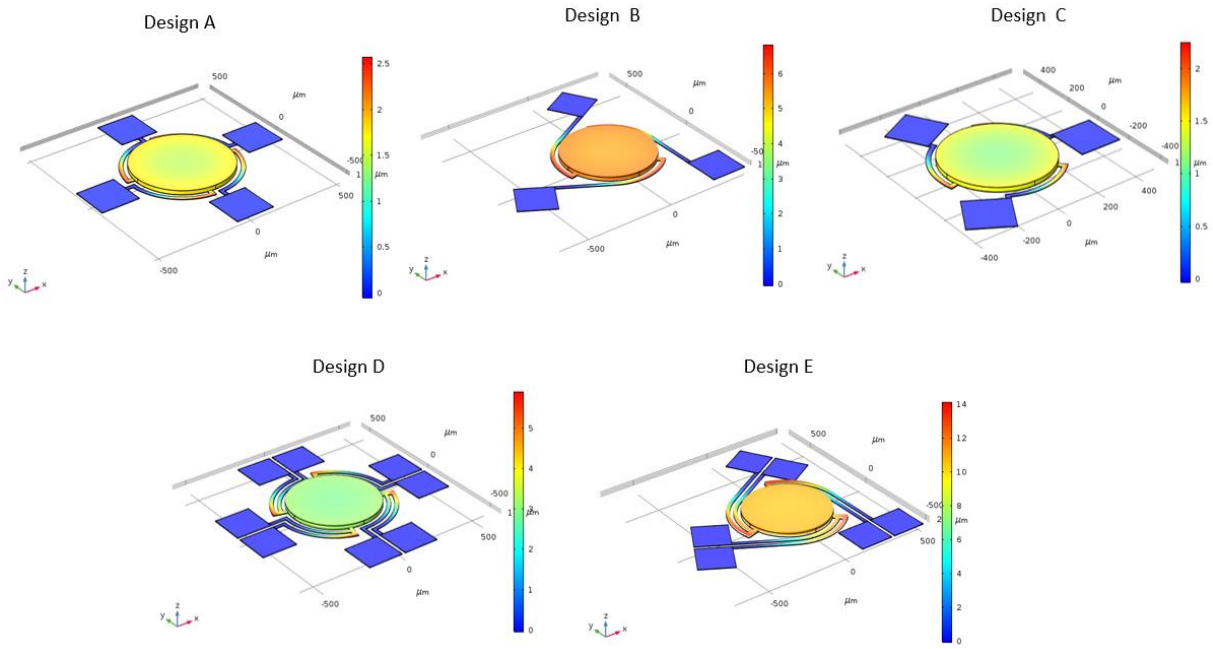

Figure 3.7. Vertical displacement of modified designs with residual stress

All dimensions and material properties remain identical as the initial designs other than the additional Si layer. The simulation results show the uniform displacement of the mirror, which convinces that the additional Si layer will keep the mirror surface flat. These designs are likewise simulated with the residual stress while 7.5 volts of voltage are applied as described in Figure 3.8.

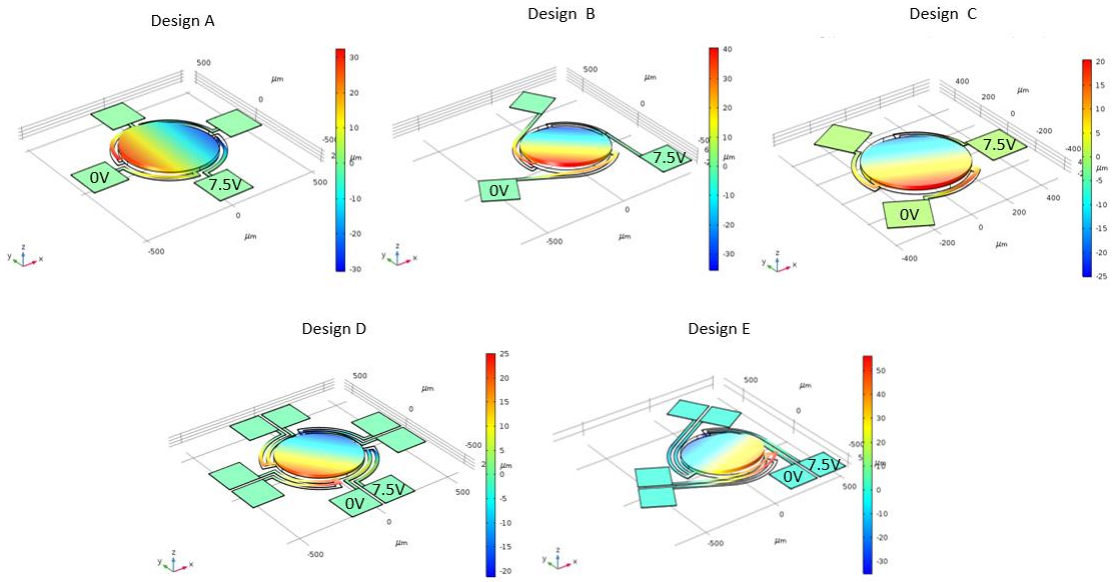

Figure 3.8. Vertical displacement of modified designs with residual stress and voltage applied

The results suggest that the micromirrors can tilt while the mirror remains flat. With the same voltage applied, among the five designs, Design E provides the maximum total vertical displacement, approximately 80 µm. To quantify the actuation with respect to the voltages, the total vertical displacement is obtained by summing the maximum upward and downward displacement. Then, the total vertical displacement is plotted as a function of applied voltage in Figure 3.9. The voltage is varied up to the point where the aluminum starts to melt.

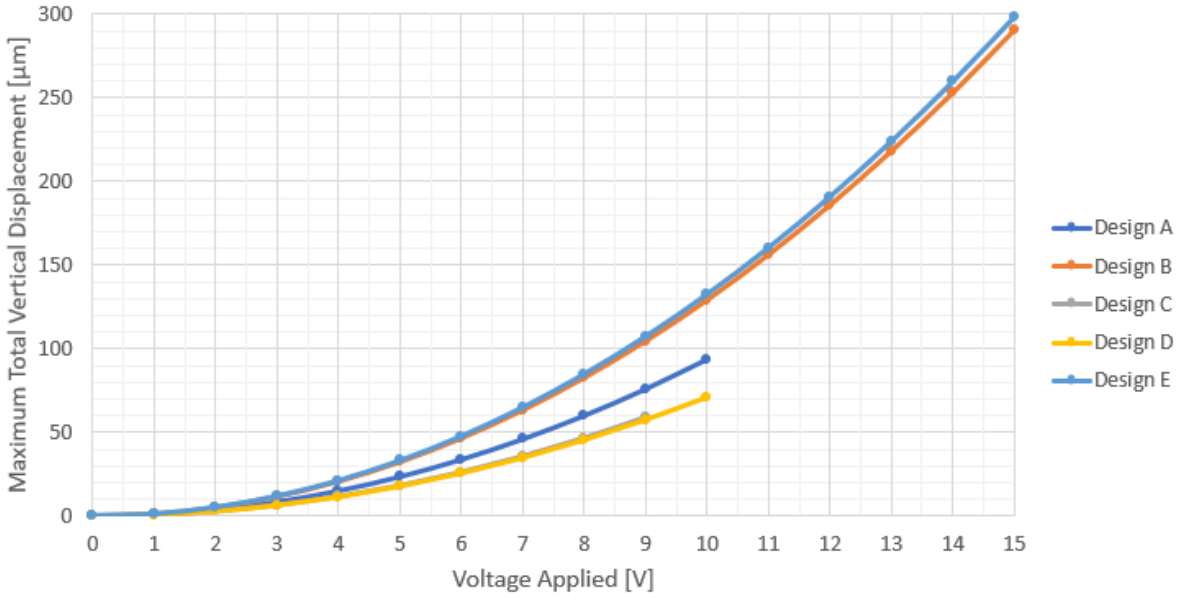

Figure 3.9. Total vertical displacement of each micromirror design as a function of applied voltage

The plot in Figure 3.9 shows that the Design B and E yield the largest deflection providing approximately 300 µm of total vertical displacement. The resistive heating of these designs is also not as significant as the other designs allowing the maximum voltage to be up to 15 V_{DC}. In addition, depending on where the voltage is applied, the rotation axis can be changed. For instance, for Design D in Figure 3.10, there are four pairs of contact pads. And two pairs; top left and bottom right results in one rotation axis while the other two pairs; top right and bottom left produces the other rotation axis shown in Figure 3.10.

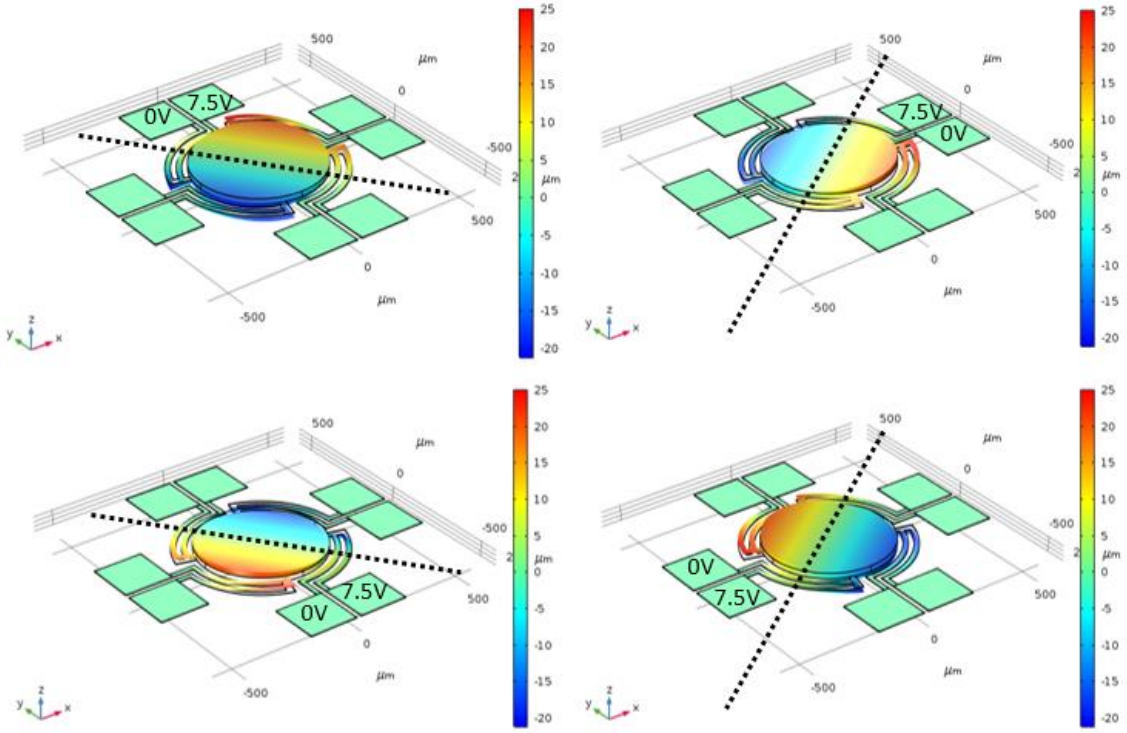

Figure 3.10. Tilt motion about two different rotation axes depending on where the voltage is applied

In Figure 3.10, voltage is applied to each pair of contact pads. It is also possible to apply voltages on multiple pairs of contact pads for Design D and E, and these variations allow more degrees of freedom. Tip-tilt motion with perpendicular axes can be achieved for Design D and A as they have even number of actuation points and symmetric structure. On the other hand, for the other designs, there are 3 axes of tilt which are 60° to each other. It is also important to realize, for Design D and E, when the voltages are applied to all the contact pads, piston motion can be achieved. Figure 3.11 presents the simulation of the piston motion from 0 V to the maximum voltages before the metal melts, which are 10 V_{DC} and 15 V_{DC} for Design D and E, respectively.

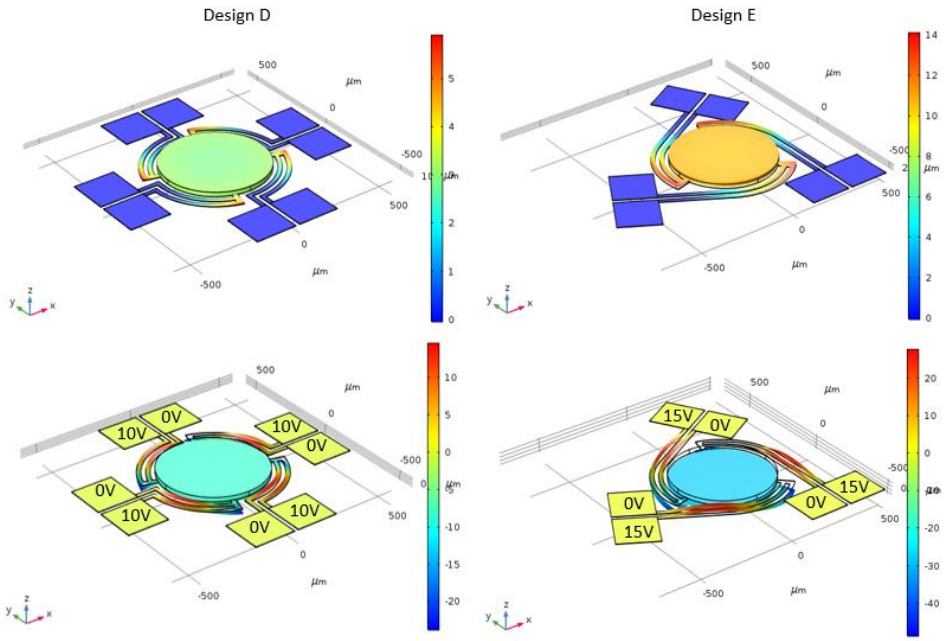

Figure 3.11. Piston motion of Design D and E without and with voltages applied to all the pads

Before applying any voltage, the mirrors for both designs are elevated due to residual stress. As the applied voltages increase, the beams heat up and bend the mirror downwards. The vertical displacement as a function of the voltage are plotted in Figure 3.12.

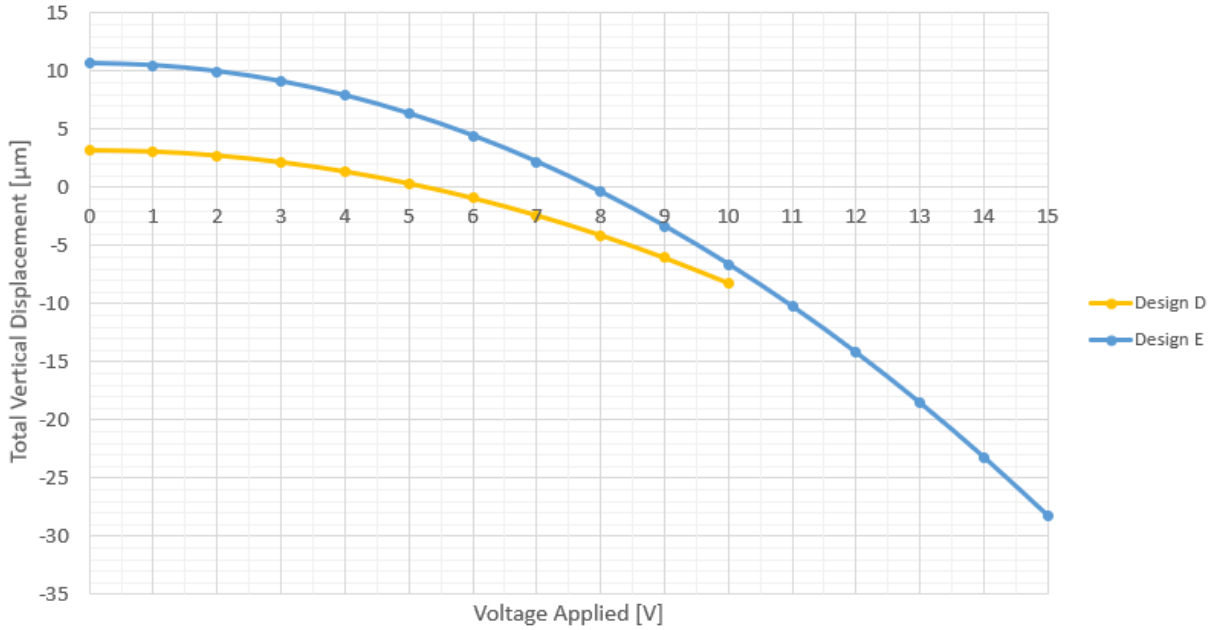

Figure 3.12 Piston motion displacement of mirror as a function of applied voltages for Design D and E

The plot in Figure 3.12 shows that the initial out-of-plane displacements of Design D and E are, respectively, 3 µm and 11 µm. As the voltages are applied to all the contact pads, the beams actuate to move the mirror downwards. For Design D, the maximum applicable voltage is 10 V, which results 8 µm downward displacement. The maximum voltage for Design E is 15 V with the maximum downward displacement of 28 µm. Therefore, the maximum total vertical displacements of the mirrors for Design D and E are approximately 11 µm and 39 µm, respectively. It is reasonable that Design E has much larger displacement than Design D as the latter has more beams attached, which mechanically constraints the motion of the mirror.

3.4. Dimension Sweep Simulation

The tip-tilt-piston motion of the different designs are simulated and compared. It is also beneficial to understand how each dimensional parameter affects the performance of the device. The dimensions mentioned in Figure 3.3 include the size of the mirror, the width and length of beams, thickness of each layer, and the gap between mirror and beam or between beams. Through the variation of different dimensions, the simulation results will be beneficial for the optimization of the next iteration of devices. The thickness of each layer in the bimorph structure affects the deflection as well. The values of thickness of silicon dioxide and aluminum layers are varied and plotted in Figure 3.13.

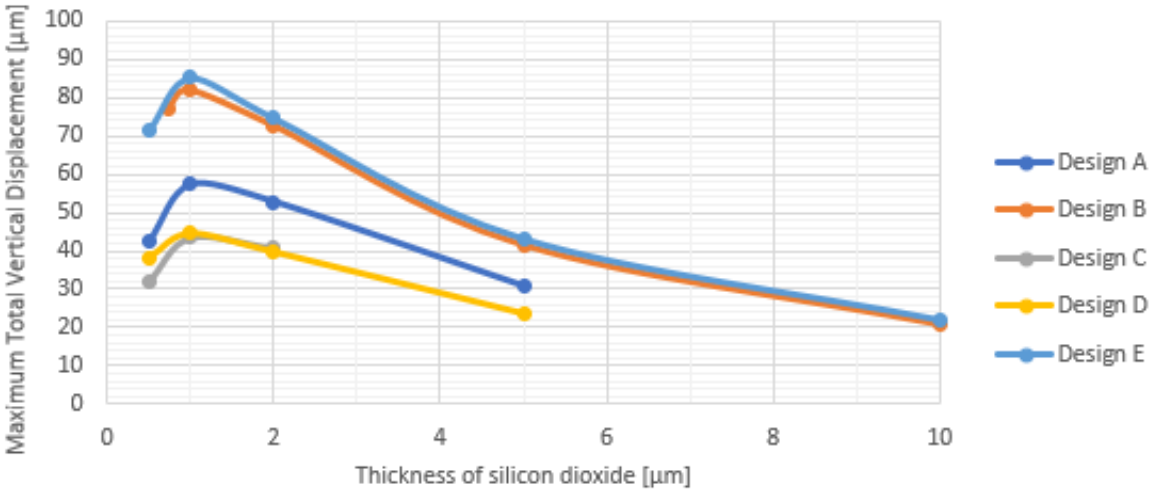

(a)

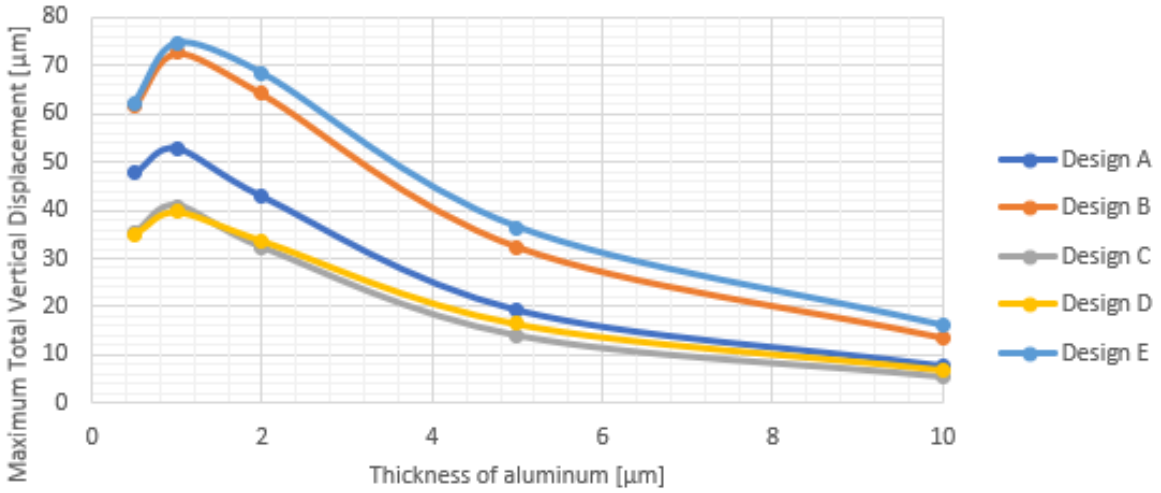

(b)

Figure 3.13. Maximum total vertical displacement as a function of (a) SiO_2 thickness, (b) Al thickness

The plots in Figure 3.13 suggest that the total vertical deflection or out-of-plane displacement will be smaller as one of the layers become thicker while the thickness of the other layer remains constant. However, less than 1 µm of thickness will decrease the deflection. Based on the simulation results, the bimorph with 1 µm of Al and 1 µm of SiO_2 would provide the largest deflection of the mirror. Nevertheless, as mentioned previously, fabricating such thin bimorph is quite challenging. For now, 1 µm of Al and 2 µm of SiO_2 are structured for the bimorph for robustness. In contrast, the thickness of the Si layer does not affect the deflection noticeably as Figure 3.14 suggests.

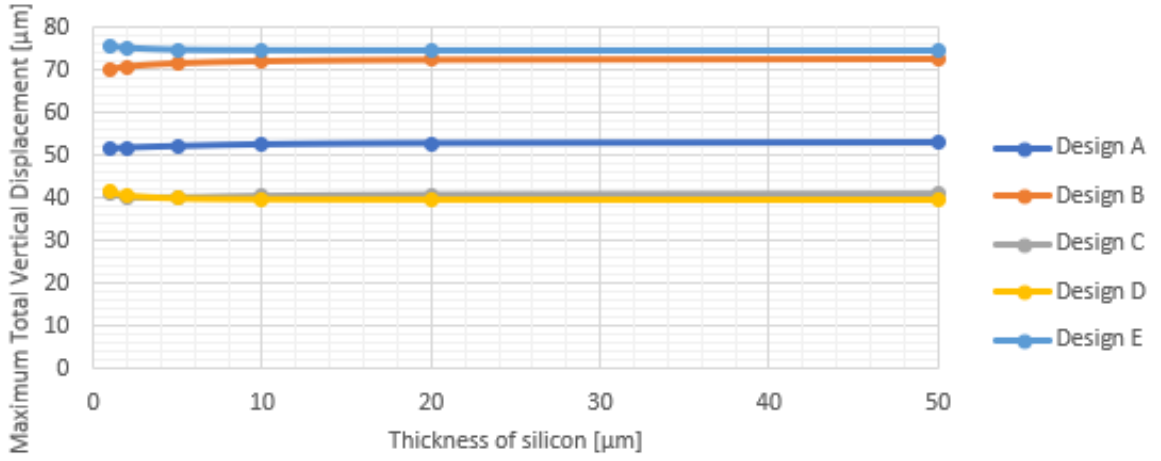

Figure 3.14 Maximum total vertical displacement as a function of Si thickness

The primary role of the silicon layer in the device is to flatten the mirror. As long as it is not so thin that the mirror will deform from the residual stress, the thickness of the silicon is not very critical for motion of mirrors.

The size of micromirror can be important depending on the applications and the size of the beam for reflection. The original radius of the mirror is 250 μm. Like the previous plots, the radius of the mirror is varied in a way that the length of the curved beams will elongate as the mirror enlarges, while the gap between the mirror and the curved beam remain constant. Figure 3.15 relates the vertical deflection and the size of the mirror for each design.

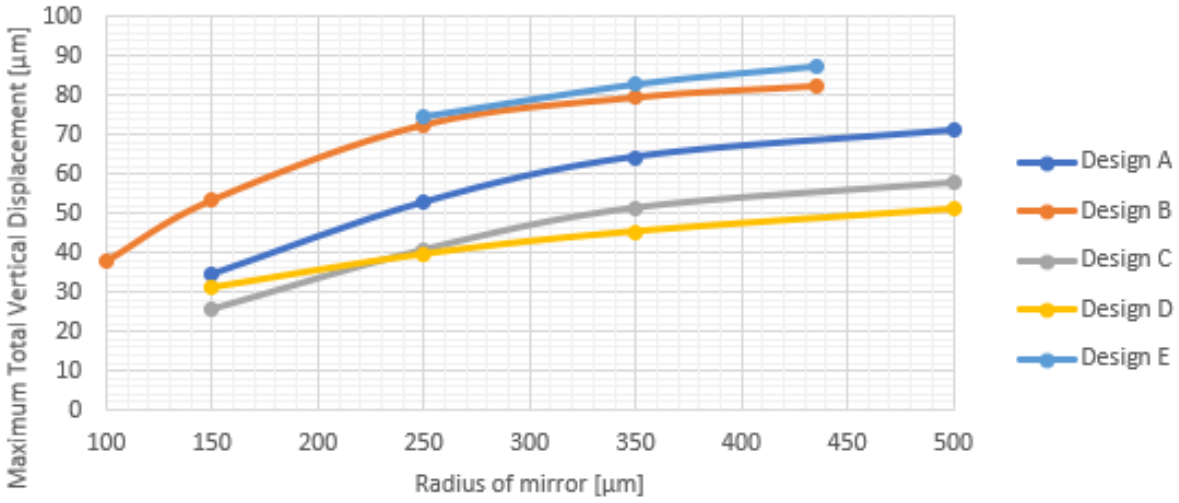

Figure 3.15. Maximum total vertical displacement as a function of mirror radius

For some designs, when the mirror becomes too small, some structures will overlap with each other making the design invalid. Also, the maximum temperature of the device is above the melting point for some cases. These data points are not plotted as they are not realistic. Figure 3.15 suggests the larger deflection can be achieved with larger mirrors at a gradual slope. However, for micromirrors, tilt angle is generally used as performance metrics rather than the vertical displacement. The tilt angle not only depends on the vertical displacement, but also the size of the mirror. Therefore, larger mirrors will not necessarily produce larger tilt. The dimensions of the beams are another important parameter that affect the actuation. Figure 3.16 depicts the vertical displacement as functions of (a) the width of the beam and (b) the length of the connecting beam.

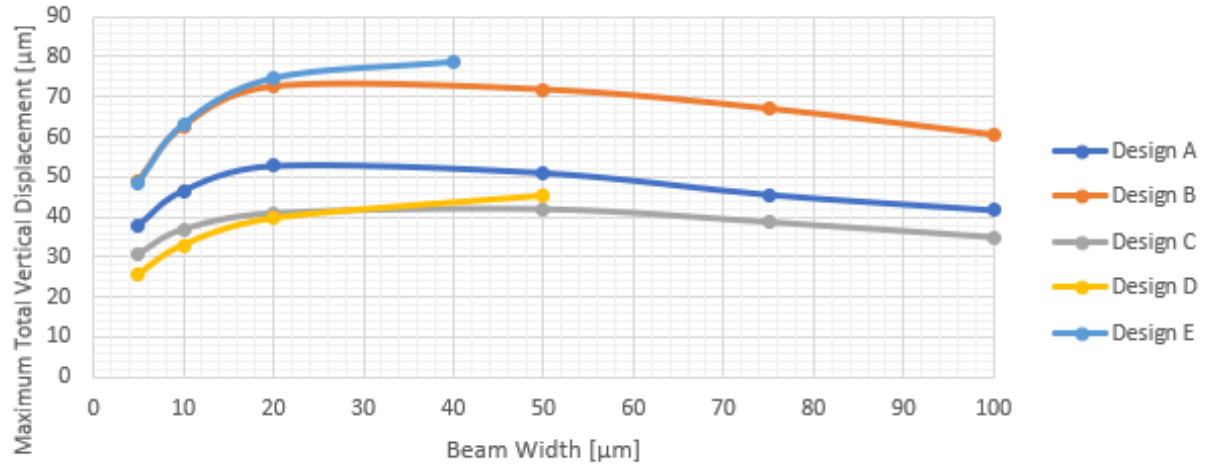

(a)

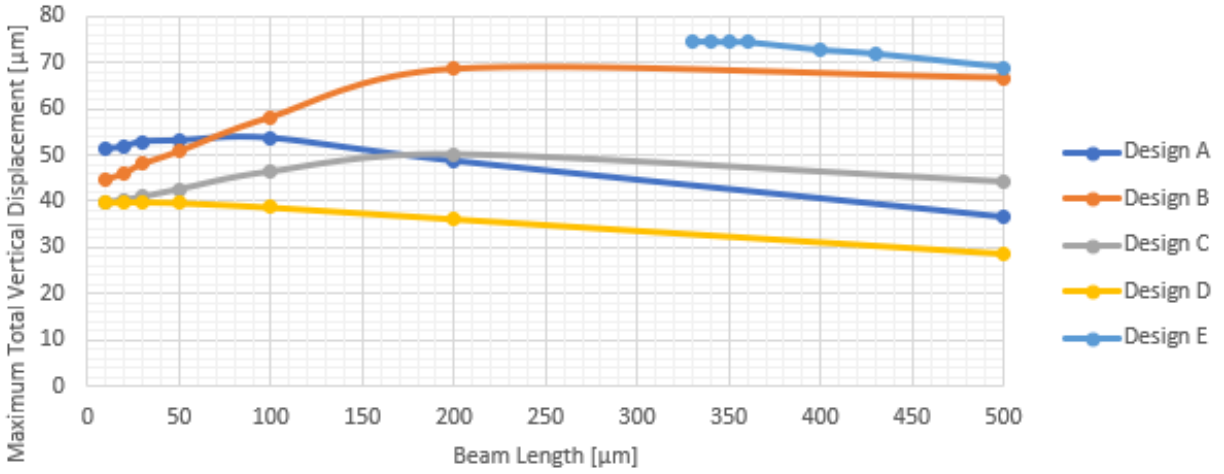

(b)

Figure 3.16. Maximum total vertical displacement as a function of (a) beam width, (b) beam length

Again, considering the melting points and the structural constraints, only valid data points are plotted. The increase in the beam width increases the vertical displacement noticeably up to 20 µm approximately, then decreases it after. The beam length is defined as the length of the beam between an anchor and a curved beam, which depends on each design. Design A, D, and E show that the increase in the length of the connecting beam gradually decrease the vertical displacement. In contrast, for design B and C, the increase in beam length increases the displacement up to 200 µm, and then gradually decrease after. Considering 500 µm of beam is quite long, the variation of the connecting beam length does not affect the displacement as much as other previous parameters.

Next, the gap between the mirror and the curved beam is varied. When this gap enlarges, the beam that connects the mirror with the curved beam automatically elongates as well. For design D and E, which

have two curved beams, another gap, g2, is present between the two curved beams. The total vertical displacement is plotted as a function of (a) the gap between the mirror and the beam, and (b) outer gap between the two beams for design D and E in Figure 3.17.

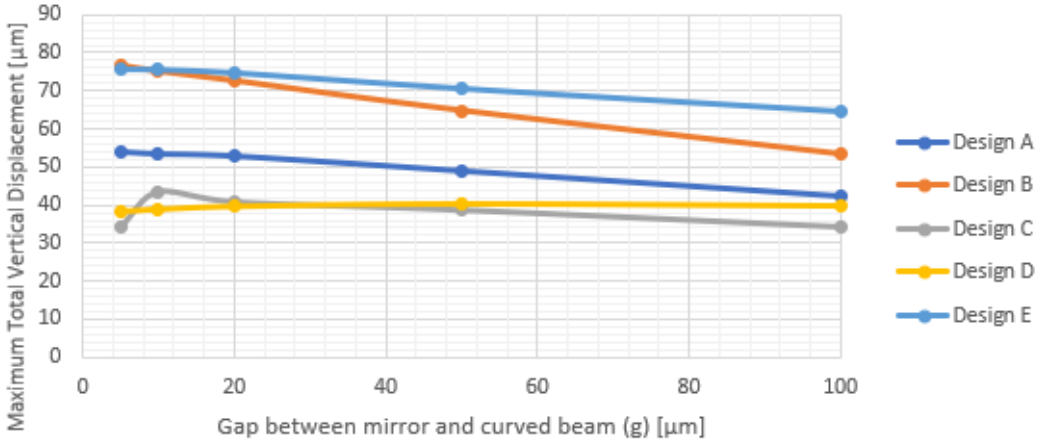

(a)

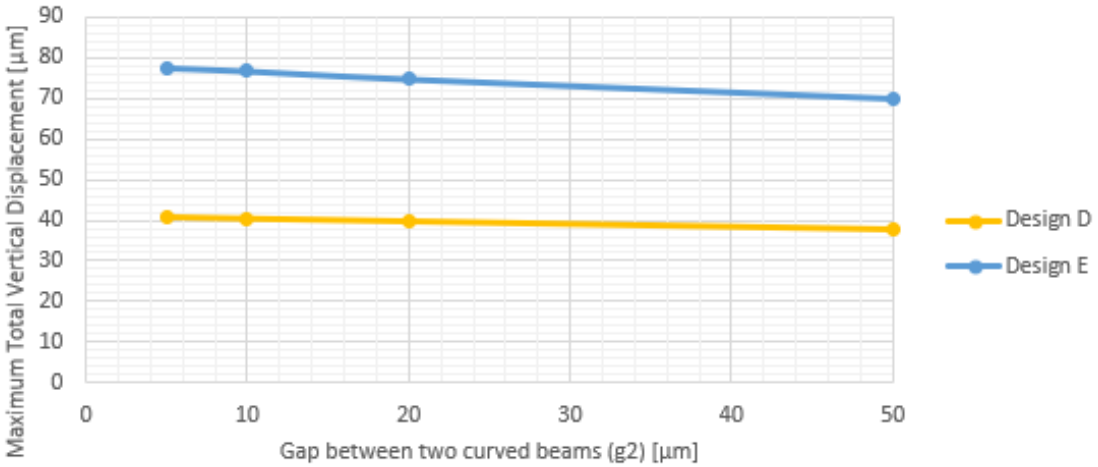

(b)

Figure 3.17. Maximum total vertical displacement as a function of (a) gap between mirror and curved beam, (b) gap between two curved beams

The trend in Figure 3.17 shows that the increase in gap gradually reduces the vertical displacement. Hence, the gaps do not significantly affect the vertical deflection of the mirror result in comparison to other dimensions.

In conclusion, the dimensions such as thickness, width, and the radius of mirror make appreciable difference in vertical displacement when the values are varied. In contrast, other dimensional parameters do not result as much difference in deflection. These simulation results will help for the design of the next iteration.

3.5. Material Sweep Simulation

The bimorph actuator includes aluminum as the top layer and silicon dioxide as the bottom layer. As mentioned previously, the reason for the two materials is due to the high difference in coefficient of thermal expansion. Aluminum is also appropriate as a mirror material for its high reflectance. It is still beneficial to study how other materials perform instead of Al and SiO_2. While the bottom layer is still SiO_2, the top layer material is swept with other metals such as silver, gold, chromium, and copper, and the total deflections with 7.5 V_{DC} using these metals and aluminum are shown for each design in Figure 3.18.

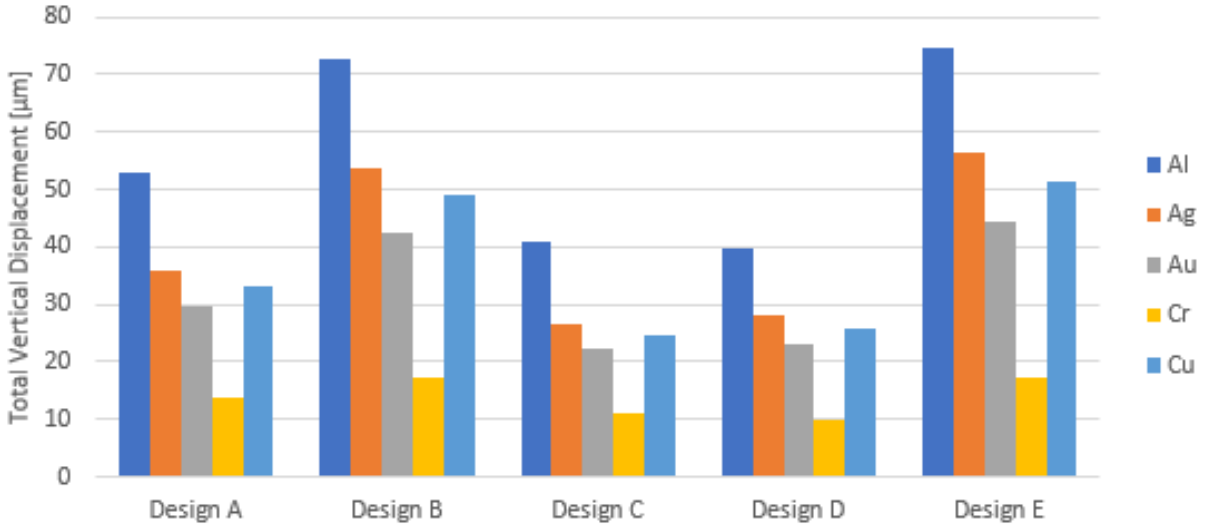

Figure 3.18. Comparison of material options for top layer of bimorph with 7.5 V_{DC} applied

As expected, the trend of the displacement follows the trend of the thermal expansion coefficient while the same voltage is applied. Even though other metals do not deflect as much as aluminum, it should be noted that the melting point of the ones with low CTE is high, which implies that the maximum applicable voltage is higher. Considering the melting points of each metal, the maximum total vertical displacement can be found. Note that the applied voltage is 7.5 V for all the cases. However, the maximum applicable voltages are different for each metal as the melting point of each material varies. For instance, the melting point of aluminum is 933 K while chromium melts at 2133 K. This implies that the applicable voltage for chromium is significantly higher. In fact, silicon will melt first as the melting point of silicon is approximately 1687 K. Although required voltage will be higher for the device with chromium layer than the one with aluminum, it may result larger displacement as it can stand higher temperature. To compare the displacement, with the maximum applicable voltage, of different materials,

DC voltage is varied with an increment of 1 V for the simulation. Table 3.3 compares the displacement of the five designs using different metals for the top layer considering the melting points of the materials.

Table 3.3. Comparison of maximum total displacement of different metals for top layer with maximum applicable voltage

Metal	Design A		Design B		Design C		Design D		Design E	
	V [V]	d [μm]	V [V]	d [μm]	V [V]	d [μm]	V [V]	d [μm]	V [V]	d [μm]
Al	10	93.847	14	253.1	9	58.7	10	70.6	15	298
Ag	13	107.61	18	309.5	12	68.2	13	84.7	19	363
Au	13	89.309	19	273.1	12	57.2	13	68.9	19	284
Cr	14	47.663	21	134.4	12	28.2	14	33.8	22	147
Cu	14	115.07	19	314.2	13	74.1	14	89.9	20	365

While the same voltage is applied for all the scenarios for Figure 3.18, the total vertical displacements shown in Table 3.3 represent the maximum displacement. For instance, for Design A with aluminum as a top layer, with 10 V applied to the electrodes, the maximum temperature of the structure is 878 K, which is below the melting point of aluminum, 933 K. When 11 V is applied to the same structure, the temperature is above 933 K, which implies the failure of the device. For the case of chromium, melting point of silicon is considered instead since the melting point of chromium is higher than the one of silicon. For Design A with chromium, the maximum temperature is 1632 K with 14 V while the melting point of silicon is 1687 K. The actuation using aluminum does not show the largest displacement anymore despite high thermal expansion coefficient because the melting point of aluminum is lower than other metals. While other metals can produce larger motion, the required voltage is also higher.

In addition, silicon dioxide can be replaced with other materials while the aluminum is the top layer. In most cases, SiO_2 is acceptable and available for the bottom layer of the bimorph in the micromirror devices as it is a commonly used material in microfabrication and also is already available in the SOI substrate. However, for comparison purpose and some special cases, the devices are simulated with other possible materials, Si_3N_4 and Al_2O_3, which is described in Figure 3.20.

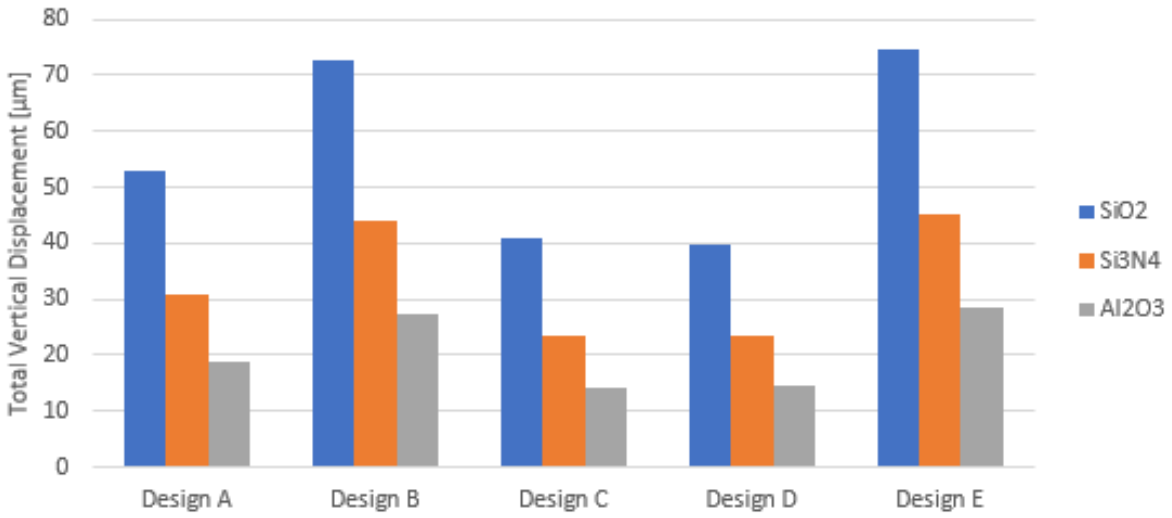

Figure 3.20 Comparison of material options for bottom layer of bimorph

While the coefficient of thermal expansion of SiO_2 is 0.56e-6, the ones of Si_3N_4 and Al_2O_3 are 3.3e-6 and 8.2e-6, respectively [35,36]. As suggested in Figure 3.20, larger displacement is achieved for bottom layer material with lower CTE as the difference in thermal expansion will be greater.

The simulation results with material sweeps have shown how various materials for the bimorph influence the deflection of the mirror. The material sweep for the top layer suggests that other metals can potentially provide actuation performance comparable to Al. Nevertheless, most of them require higher actuation voltage as their CTEs are not high as Al. Also, some of alternative metals have challenges in fabrication as they are prohibited in a DRIE chamber. For the bottom layer, SiO_2 is the most suitable material as it is readily available in SOI wafers and has low CTE. As a result, for the thermal bimorph in micromirror devices, Al and SiO_2 are excellent choices for top and bottom layers, respectively. Other materials may be more advantageous for future applications.

3.6. Summary

The final design of the device includes Al/SiO_2 bimorphs for actuation while the mirror has an additional Si layer between the Al and SiO_2 layers, this additional Si layer is added from the initial design to prevent the mirror to curve. There are five different designs with various number of beams and configurations. The simulation results convince that 2D rotational motion can be achieved for all the designs and the Design D and E can also produce translational motion. According to the simulation, Design E shows the

largest vertical displacement of approximately 300 μm for tilt motion with 15 V_{DC} while producing 38 μm displacement in piston motion with 15 V_{DC} applied to all three pairs of pads. In addition, the dimension parameters are varied during the simulation to study the effect of some dimensions. The results suggest the parameters like the thickness of Al or SiO_2, width of beams, and the radius of mirror make noticeable difference in actuation while others do not influence as much. The original dimensions still produce notable motion for the mirror. In addition, simulation including the material sweep convinces that aluminum and silicon dioxide are the most appropriate choice for the performance of the micromirror in terms of vertical displacement and required voltage although other materials may replace them depending on applications. As a result, the five designs are proposed and compared with some variations in dimensions and materials. The simulated results promise excellent performance of the micromirrors.

Chapter 4. Microfabrication and Results

Microfabrication is an important aspect of this research as a delicate process is required to produce a micromirror. Although most microfabrication tools and materials used in this study are commonly used, there are still some challenges encountered during the fabrication. One of the most important tools in the process is DRIE (Deep Reactive Ion Etch) equipment, which is used multiple times in this fabrication. The deposition and etch of aluminum layer are also essential steps, and lift-off technique is selected to process aluminum layer. In addition, thermal residual stress, which is briefly mentioned as a common issue in thin-film process, is addressed by having an additional silicon layer. The goal of the first half of this chapter is to describe the fabrication process, the issues faced during the process, and the solutions to them.

After multiple runs of microfabrication processes, the process is finalized and executed. In the second half of this chapter, the characterization methods and the results are highlighted. The fabricated micromirrors are characterized visually with SEM (Scanning Electron Microscope), and experimentally quantified with data acquired from an optical profiler. Additionally, the temperature of the device is measured in response to applied voltage. Finally, these results are compared with the simulation results from Chapter 3.

4.1. Fabrication Process

An SOI wafer, composed of silicon device layer, silicon oxide layer, and silicon handle layer, is processed to create the micromirror devices. The thickness of silicon device layer determines the thickness of the additional layer below the mirror, and the oxide layer will be the bottom layer of the Al/SiO_2 bimorph structure. The thickness of the handle layer is not critical for the performance of the micromirror device, but thinner substrate layer is desired as the backside etch will require less cycles with thinner substrate. For this study, the thickness values of the device, oxide, and handle layers are 20 μm, 2 μm, and 400 μm, respectively.

For the initial devices described in Section 3.2, either oxide coated Si or SOI wafers can be used. SOI wafers are cleaned with RCA clean process and the device layer is completely etched to oxide layer using DRIE. The fabrication process, starting with silicon oxide coated silicon wafer, is described in Figure 4.1.

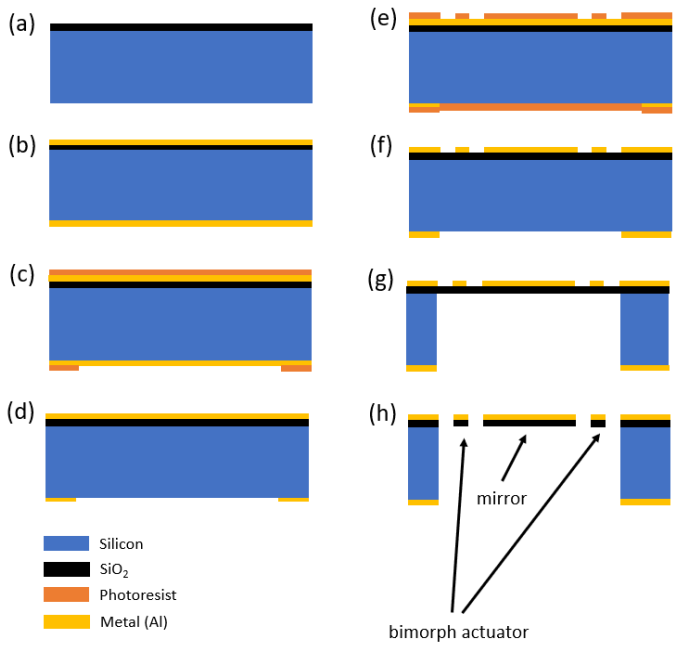

Figure 4.1. Microfabrication steps of the initial micromirror device:

(a) 2 µm SiO_2 on Si wafer
(b) 1 µm and 0.5 µm Al deposition on frontside and backside, respectively
(c) Backside lithography and photoresist spin coat on frontside
(d) Al etch and photoresist strip
(e) Frontside lithography and photoresist spin coat on backside
(f) Al etch and photoresist strip
(g) Backside Si-DRIE up to oxide etch stop
(f) Frontside oxide etch with RIE to release

After (a) RCA cleaning and dehydration at 120°C for 5 minutes on a hot plate, (b) 1 µm and 0.5 µm of aluminum is deposited on the frontside and then the backside of the wafer by sputtering. Then, (c) AZ3330 positive photoresist (Integrated Micro Materials) is spin-coated at 2000 rpm on the frontside and prebaked at 90°C for 1 minute. The prebaked sample is patterned and exposed with 375nm and developed by AZ 300MIF developer (Integrated Micro Materials). The wafer is post-baked at 110°C for 2 minutes. The backside of the wafer is then spin coated at 2000 rpm and baked at 110°C for 2 minutes again to prevent Al etch during wet etch. Next, (d) the Al layer on the frontside is patterned via phosphoric, acetic, and nitric acids (PAN) etch, and the photoresist on both sides is stripped with acetone and isopropyl alcohol (IPA). Like step (c), (e) after spin coating and prebaking, the backside is aligned to the frontside pattern, exposed, and developed with the photoresist. And the frontside is covered by spin coating for protection. The wet etch using the PAN solution is preceded for the backside. Once both sides are patterned with Al, the wafer is diced into an individual die, and (g) the backside Si is etched with DRIE until it reaches the oxide layer. Finally, (h) the oxide is etched from the frontside with RIE to release the device. The process requires two masks; one for the frontside and the other for the backside. The layout of the masks used for the initial design is shown in Figure 4.2 (a). However, due to residual stress from fabrication, which causes the mirror to be curved, the initial design needs to be modified. The modified design discussed in Section 3.3 requires three masks including the same two masks from the initial layout and an additional mask for the mirror as described in Figure 4.2 (b).

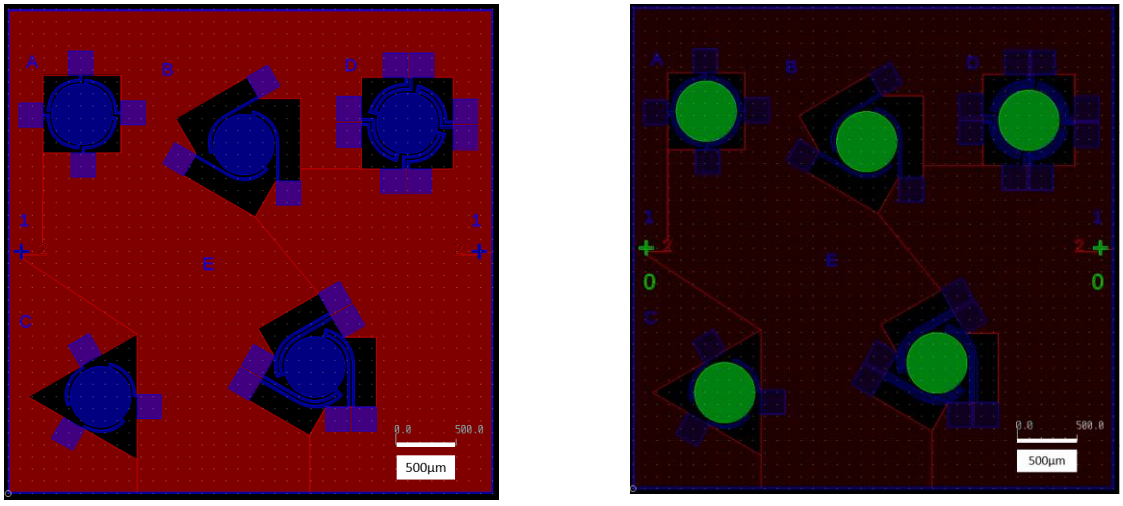

Figure 4.2. (a) Mask layout: Frontside (blue) and Backside (red). (b) Mask layout with an additional mask (green) for mirror structure

As discussed previously, the device needs to include an additional layer to avoid the mirror to be curved, and Figure 4.2 (b) corresponds to the additional mask for the Si layer. With the additional mask, the microfabrication steps for the modified designs are described in Figure 4.3.

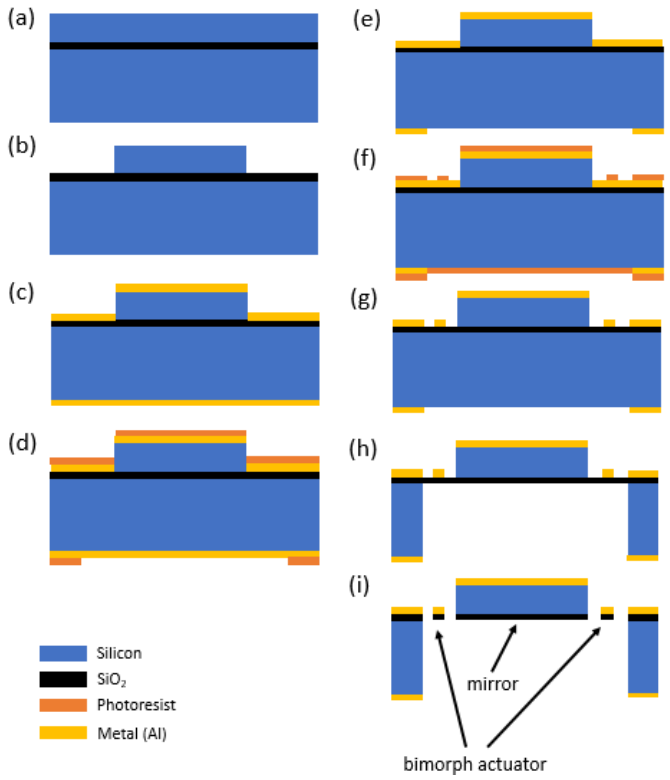

Figure 4.3. Microfabrication steps of the modified micromirror device:

(a) SOI wafer
(b) Si patterned for mirror structure via Si-DRIE
(c) Al deposition on both sides (1 µm frontside and 0.5 µm backside)
(d) Backside Mask lithography and photoresist spin coat on frontside
(e) Al etch and photoresist strip
(f) Frontside Mask lithography and photoresist spin coat on backside
(g) Al etch and photoresist strip
(h) Backside Si-DRIE up to oxide etch stop
(i) Frontside SiO_2 etch with DRIE to release

The fabrication process in Figure 4.3 includes some variations from the steps in Figure 4.1. Starting with an SOI wafer, (b) the additional mask is patterned to the device layer via photolithography and DRIE. The next steps (c)-(i) in Figure 4.3 are almost identical to the steps (b)-(h). For the steps (f)-(g) in Figure 4.1, the aluminum layer is patterned on the frontside and etched with the PAN (Phosphoric acid, Acetic acid, and Nitric acid) etchant. However, these steps are later replaced with lift-off process due to issues with wet etch, which will be addressed in the next section.

The thickness ratio of Al and SiO_2 is important for the actuation, and according to the simulation, the thickness of 1 μm for both layers provide large deflection. Nevertheless, 1 μm of Al and 1 μm of SiO_2 are not sufficiently thick for the stability of the structure. A bimorph with the total thickness of 2 μm will be very fragile. To produce more robust structure, 2 μm is used for the oxide layer while the metal layer is still 1 μm thick. The thickness of aluminum is also limited to approximately 1 μm due to the fabrication capability of the sputtering method. Therefore, 2 μm of silicon oxide and 1 μm of Al are used for the microfabrication process. For the backside Al, on the other hand, since aluminum layer is only used as a hard mask, 0.5 μm of Al is deposited.

4.1.1. Aluminum Deposition and Etch

There are several variations to deposit and etch aluminum layers. For Al thin film deposition, sputtering and E-beam evaporation are the most commonly used Physical Vapour Deposition (PVD) methods in microfabrication. For this device, sputtering process is used due to its capability to deposit thick Al. It is quite challenging to deposit 1 μm of aluminum with E-beam evaporation. The issue is that the Al pellets in the crucible will run out before the deposition completes and the beam will start to melt the crucible.

To etch aluminum layer after patterning, possible options are wet etch or dry etch. Photoresist patterned for the layer needs to be stripped after the etch process. Wet etch is inexpensive, simple and selective, however, suffers from undercutting due to its isotropic etch profile. To wet etch aluminum, the PAN solution, composed of phosphoric acid, acetic acid, and nitric acid, are typically used. Due to isotropic etch, the PAN solution etches aluminum laterally and results in undercutting. In addition, wet etching is relatively non-uniform through the wafer, due to the temperature variation in the etch solution. Moreover, the formation of bubbles from the etch reaction may worsen the non-uniformity and undercutting for some areas. In contrast, dry etch provides anisotropic profile with no or unnoticeable undercutting. Metal-

RIE (Reactive Ion Etch) and Ion milling processes are possible tools to dry etch aluminum. Metal-RIE is preferred for much higher etch rate compared to ion milling process because longer etch duration will harden the photoresist more. Nevertheless, even for metal-RIE, the use of plasma heat and cross-link the photoresist making the photoresist difficult to remove after. Stripper solution can be used to remove the photoresist, and ultrasonic treatment can also help the removal. O_2 descum process as well can assist for stripping. However, as 1 μm of aluminum is quite thick and requires relatively long etch duration, which causes more heating and hardens the photoresist, stripping photoresist becomes a problematic issue. As shown in Figure 4.4, even after all the stripping methods mentioned previously, some residues of photoresist remain bonded on the surface.

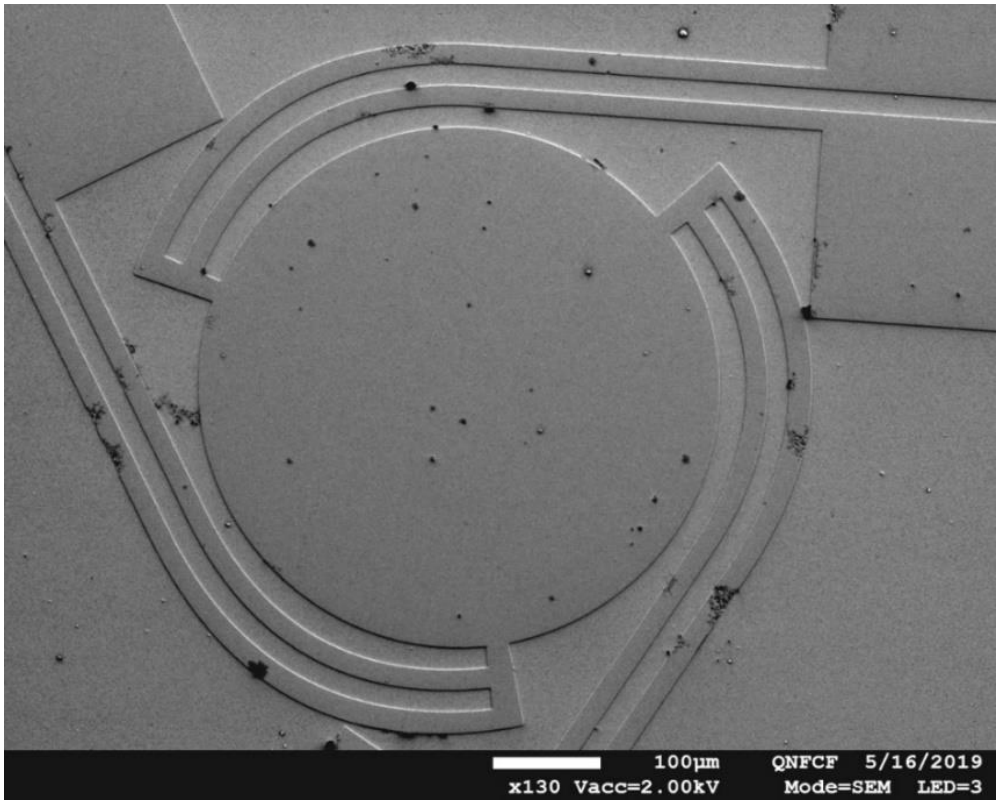

Figure 4.4. SEM image showing residues of photoresist after metal RIE etching 1 μm of Al layer

To overcome the challenges of both wet and dry etch, lift-off process is a suitable alternative. In lift off process, photoresist is spin-coated and inversely-patterned prior to the metal deposition. Next, metal is deposited on the patterned photoresist. Finally, using stripper, the photoresist is easily removed with metal. The pattern must be inversed since where the photoresist remains will be stripped. Figure 4.5 describes the fabrication steps with the lift-off process. Figure 4.5 (d)-(f) correspond to the lift-off step.

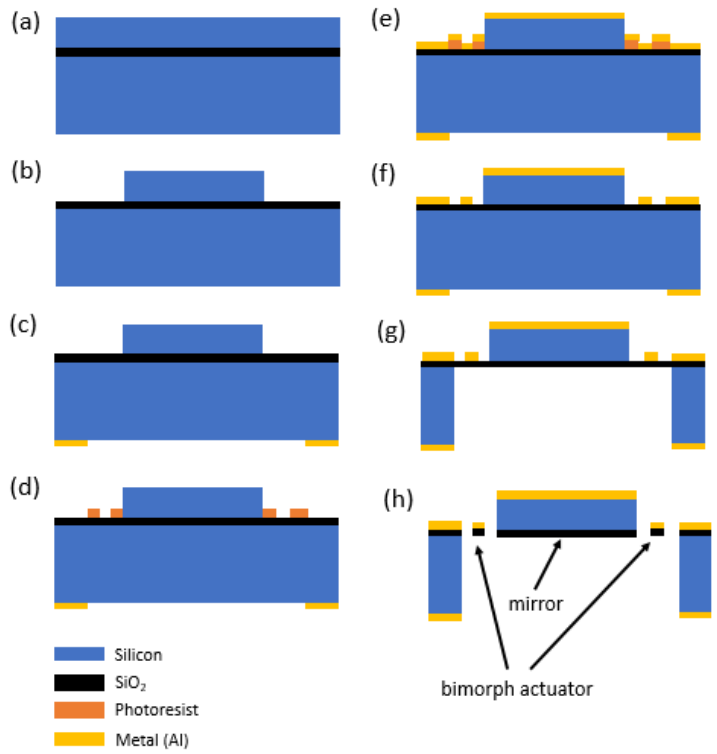

Figure 4.5. Microfabrication steps of the modified micromirror device with lift-off process:

(a) SOI wafer
(b) Si patterned for mirror structure and etched via Si-DRIE
(c) Al (0.5 µm) deposition, pattern, and etch on backside
(d) Photoresist spin coat and photolithograph with inversely pattern on frontside
(e) Al deposition
(f) Photoresist stripping for lift off
(g) Backside Si-DRIE up to oxide etch stop
(h) Frontside SiO_2 etch with DRIE to release

After (b) the device layer is patterned, 0.5 µm of aluminum is sputtered, patterned with photoresist, and wet-etched using the PAN solution similarly to the previous steps. Then, (d) photoresist, spin-coated at 2000 rpm, is patterned, but this time, negative photoresist, AZ nLOF 2035, is used to inverse the pattern. Next, 1 µm of aluminum is sputtered, and (f) the lift-off is preceded by the stripper solution. After, the wafer is diced, and the silicon and oxide layers are etched in the similar manner as the previous process. For the deposition during lift-off process, E-beam evaporation is typically used rather than sputtering because E-beam evaporation is more directional. If the deposition is not directional, the sidewall of photoresist will be covered with the metal, which prevents the stripper to attack the photoresist. Nonetheless, it is still feasible to execute lift-off process with sputtering if the photoresist is thick enough. Hence, for the frontside aluminum layer, lift-off process is implemented to resolve issues in dry and wet etch.

4.1.2. Deep Reactive Ion Etch

Deep Reactive Ion Etch (DRIE) is one of the most essential equipment used in the process for the devices. The DRIE process, unlike the conventional reactive ion etch (RIE), allows deep etch for the opening on the backside to release the structure by Bosch process. Bosch process involves cycles of two-steps to increase the anisotropy of the etch profile. Each cycle includes the etch step and the passivation step. The etch step removes the unmasked silicon while the passivation step deposits polymer to protect the sidewalls, which is displayed in Figure 4.6 (a).

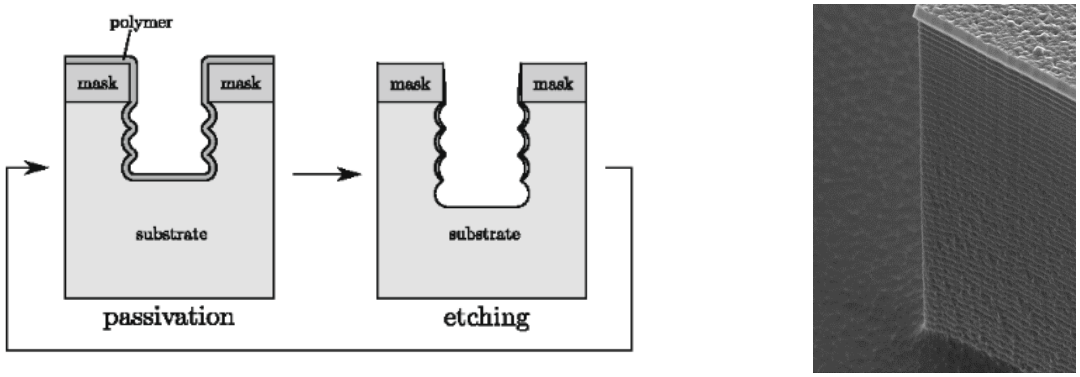

(a) (b)

Figure 4.6. (a) Passivation and etch cycles of Bosch process [37]. (b) SEM image of scallop effect on sidewall from Bosch process.

The passivation layer protects the side wall enabling further anisotropic etch. After many cycles, deep etch profile with a high aspect ratio can be achieved. One of the commonly mentioned issues in DRIE is scallop effect. After numerous cycles, the sidewall will not be completely straight, but will have some wavy curves as shown in Figure 4.6 (b). However, as the sidewall flatness does not influence the operation of the micromirror in this paper, the scallop effect is acceptable.

For the final micromirror device, DRIE is run three times in total, for mirror structure, backside etch, and finally oxide etch. There is a reason why the backside Si is etched prior to the oxide even though the reverse order produces the same structure. Before the DRIE process, the wafer is diced into each die because the vibration from dicing will damage the released structured. However, the DRIE can generally only etch wafer size samples, and a carrier wafer must be used. When using a carrier wafer, each die is attached to the carrier wafer with an adhesive and is detached after the DRIE process. If the oxide is etched first, during the backside etch, the frontside will stick to the carrier wafer. Once the backside etch

is complete, the structure is fully released while the frontside of the sample is still stuck to the carrier wafer. Detaching the sample from the carrier wafer will break the released structure. Therefore, the backside must be etched prior to the oxide etch.

In conclusion, the deep etch profile is accomplished by the Bosch process using the DRIE equipment. The etched Si on the backside provides the space for the mirror to displace. Despite the scallop effect on the sidewall from the Bosch process, it will not affect the micromirror operation. In addition, the wafers are diced before the DRIE process because once the structure is released, dicing process will damage the samples. Finally, the diced sample is individually bonded to a carrier wafer for the DRIE process, and the backside must be etched prior to the oxide etch to avoid the breakage of the released structure on the frontside.

4.1.3. Residual Stress

Residual stress is a common issue in thin film process due to extrinsic thermal stress induced from the difference in thermal expansion coefficient. For example, during Al sputtering, the substrate temperature is raised while Al is deposited on SiO_2 layer. After the deposition, the substrate cools down to room temperature, which causes both layers to shrink. While both layers shrink, the material with higher coefficient of thermal expansion will shrink more than the one with lower CTE. Therefore, residual stress is induced, and when the device is finally released, the residual stress will elevate the free end of the suspended structure. In fact, bimorph thermal actuators take an advantage of this thermal effect. When the temperature is raised from room temperature, the aluminum will expand more than the oxide, and displace the beam downward.

In Chapter 3, the simulations include the stress between layers. As mentioned, the value of the residual stress depends on a lot of factors from the process and the samples. To keep the mirror flat, the device layer from the SOI wafer is present between Al and SiO_2. Without the additional structure, the curved mirror will not be able to function as a reliable mirror. Figure 4.7 compares the SEM images of the devices (a) with, and (b) without the Si layer and suggests that the mirror can remain flat with the thick Si layer.

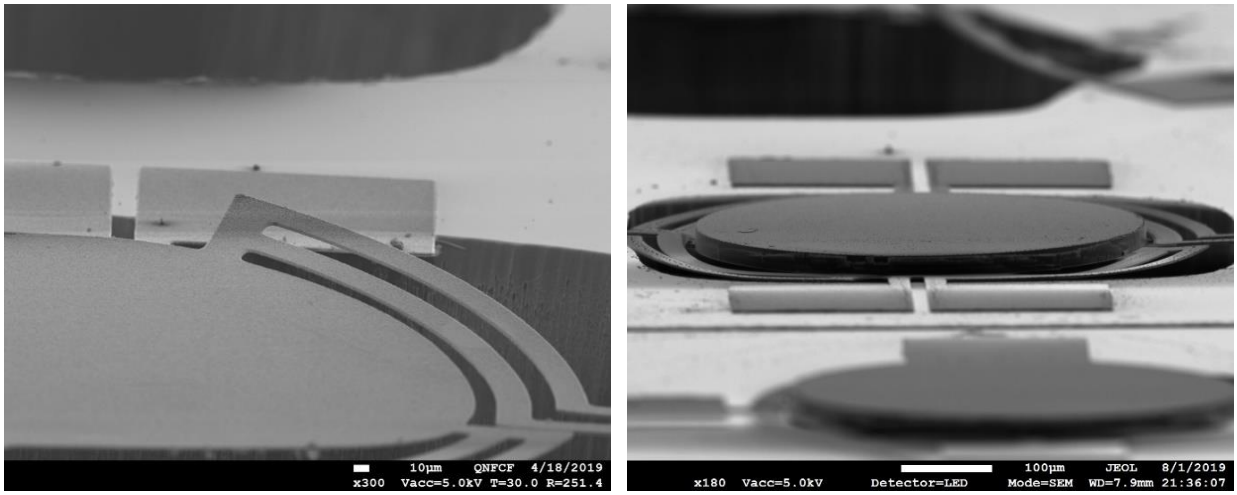

(a) (b)

Figure 4.7. SEM images (sideview) of micromirror device showing the effect of residual thermal stress (a) with, and (b) without silicon device layer

As shown in Figure 4.7 (a), the device without an additional silicon layer shows curvature not only on the actuator beams, but also on the mirror itself. This is undesired as a micromirror as the reflective surface needs to remain flat during the operation. In contrast, the mirror that has silicon device layer sandwiched between Al and SiO_2 remains flat despite the residual stress from fabrication while the bimorph beams are still curved. Therefore, the micromirror device takes an advantage of the Si device layer from the SOI substrate to prevent the curvature of the mirror from residual stress during fabrication. For the Si layer, 20 µm is thick enough to avoid curving. Thinner or thicker layer may be used depending on the initial substrate and the process conditions. At this point, the SEM results suggest that 20 µm of Si layer is sufficient to flatten the mirror from the residual stress. This topic is revisited in the later chapter to ensure the flatness of the mirror with quantified measurement using an optical profiler.

4.2. Characterization

After the fabrication of the proposed design of micromirror devices, the devices are characterized. To ensure that fabrication is successfully completed, and the devices are released properly, SEM images of each design of the fabricated devices are shown in Figure 4.8.

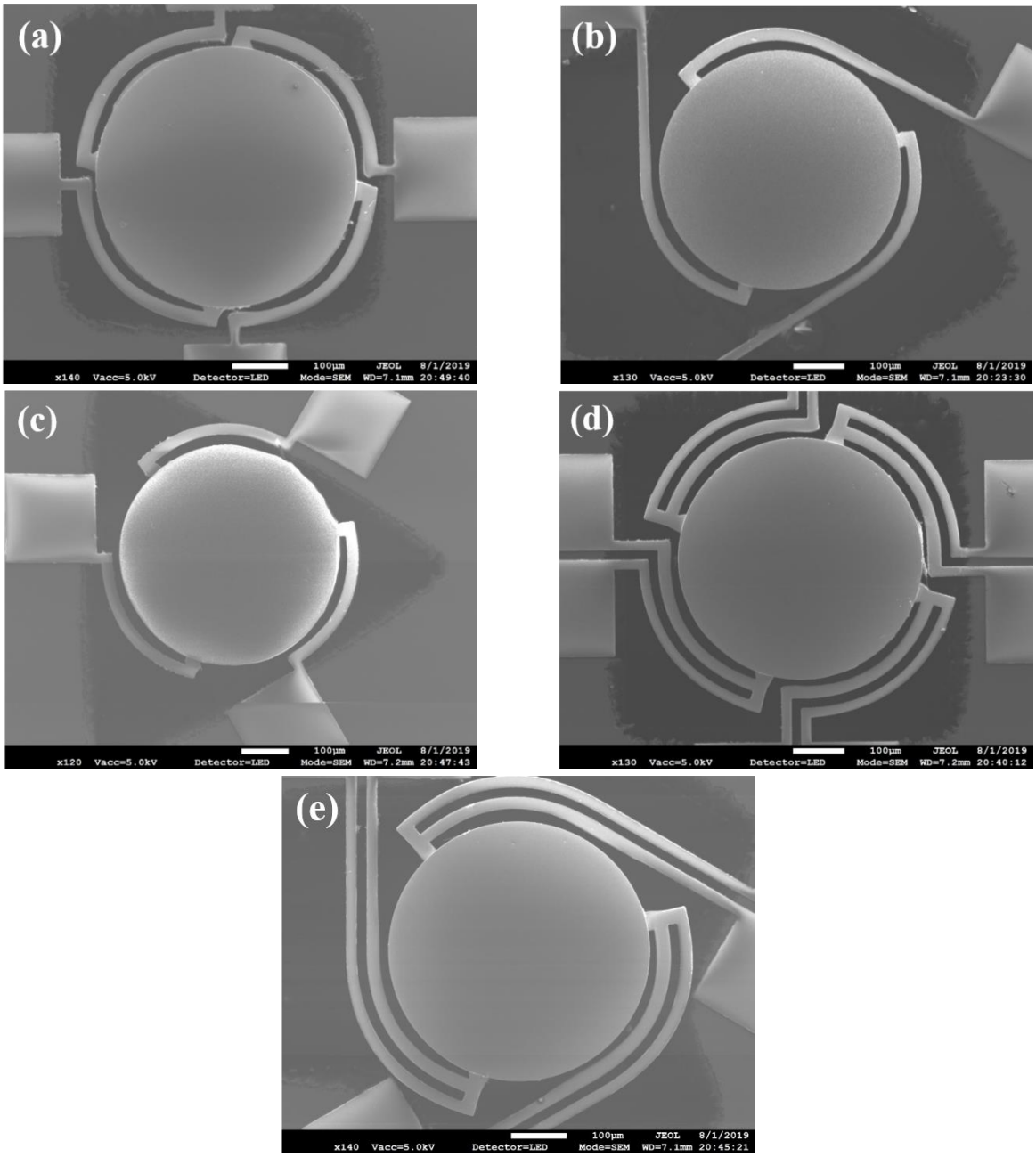

Figure 4.8. SEM images (top view) of complete micromirror devices of Design (a) A, (b) B, (c) C, (d) D, and (e) E.

After successful fabrication, the devices are visualized under an optical microscope to verify that the mirrors can tilt with voltage. For this validation, sinusoidal AC voltage is applied at 1 Hz, and the screenshots of the recorded video are displayed in Figure 4.9 and Figure 4.10 for Design D and E with applied voltage of 4 $V_{p\text{-}p}$ and 5 $V_{p\text{-}p}$, respectively.

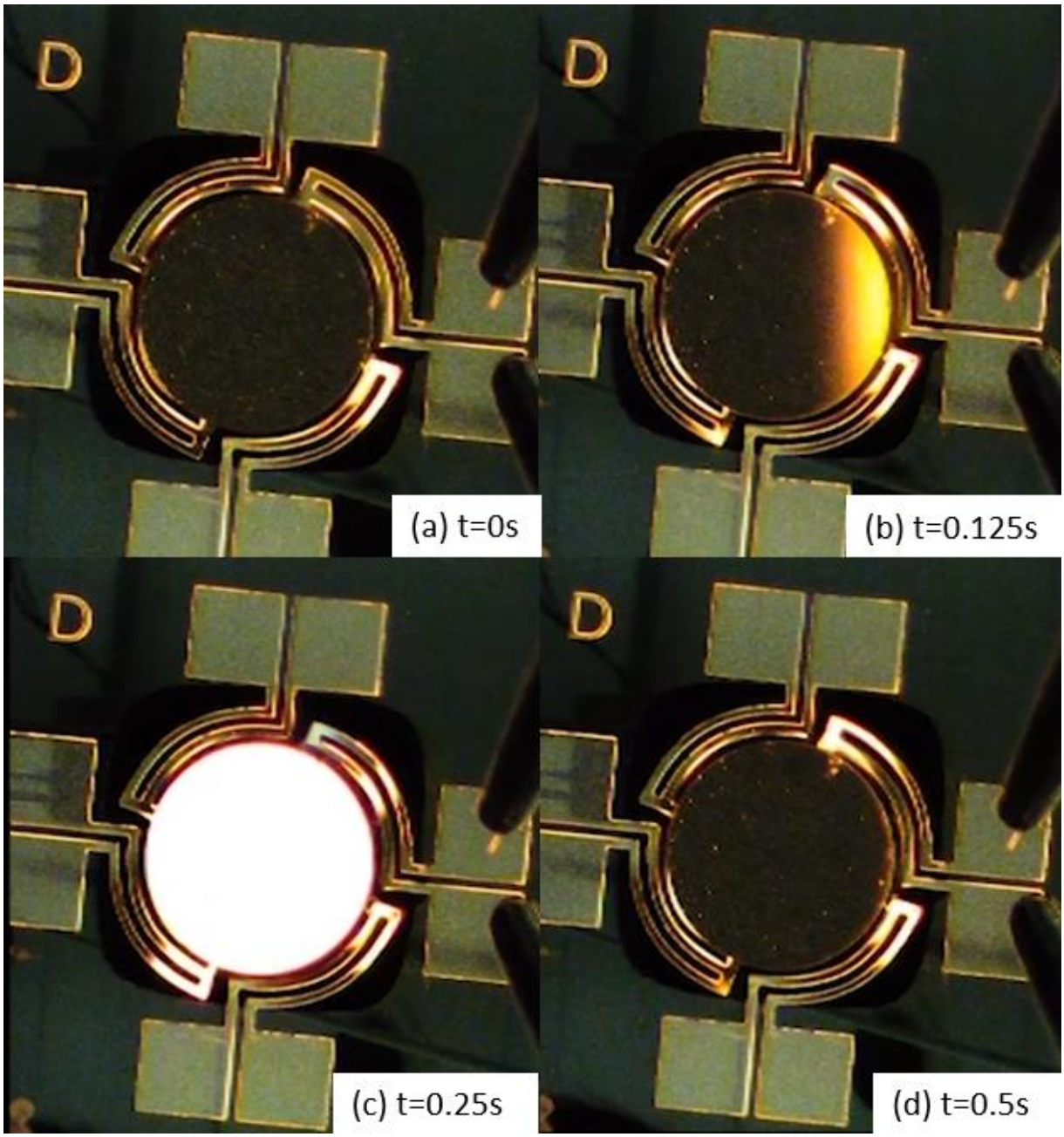

Figure 4.9. Optical microscopic images showing micromirror device at different time points with applied voltage of 4 $V_{ac,\,sin}$ at 1 Hz for Design D

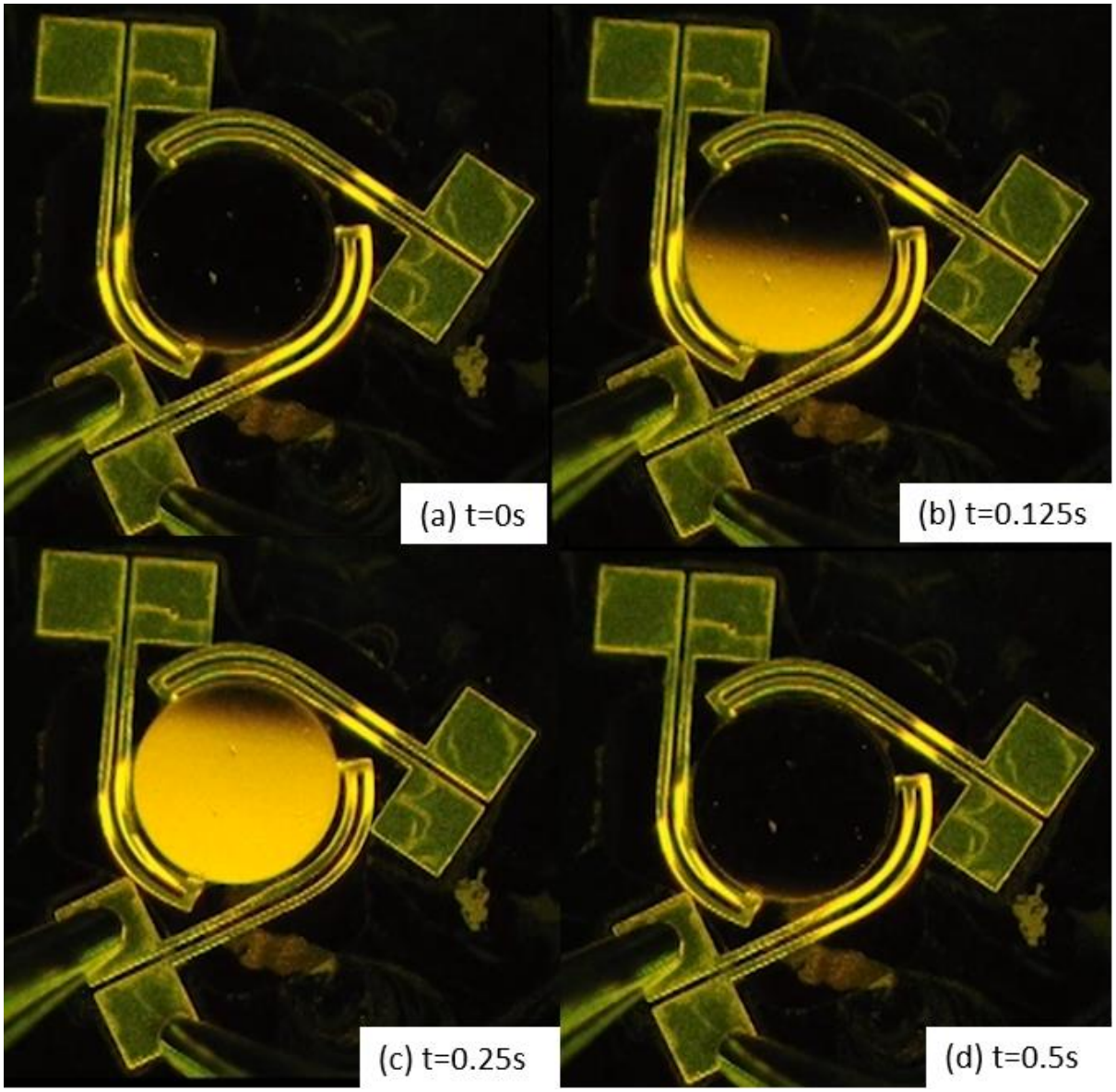

Figure 4.10. Optical microscopic images showing micromirror device at different time points with applied voltage of 5 $V_{ac, sin}$ at 1 Hz for Design E

Figure 4.9 and 4.10 verify the capability of the tilting motion of micromirrors. They also suggest that the applied voltage at 1 Hz results the actuation at 2 Hz. With the voltage at 1 Hz, after 1/8 seconds, the actuation is half of the full tilt, and after a quarter seconds, the tilt is at the maximum peak. After a half of period, the mirror is back to the initial state. Then, the same cycle will repeat as the voltage drops, and this is reasonable since the resistive heating occurs in the same manner when the voltage is negative. This may differ with higher frequency as the device takes time for the heated section to cool down. Nevertheless, the optical microscopy images confirm the operation of the micromirror devices.

Despite the validation of the actuation of the devices, it is also important to quantify the displacement or the tilt angle with respect to the applied voltage. To obtain quantitative measurement, an optical profiler is used to characterize the surface profile of the samples. The optical profiler can also compare the flatness of the mirror between the devices with and without the silicon layer.

4.2.1. Experimental Set-up and Results

To investigate the surface profile of the micromirror devices, a Bruker contour optical profiler, based on white light interferometry, is employed. Principle of white light interferometer is based on the measurement of the inference of the two beams in different phase, and the picture of the profiler are displayed in Figure 4.11 (a).

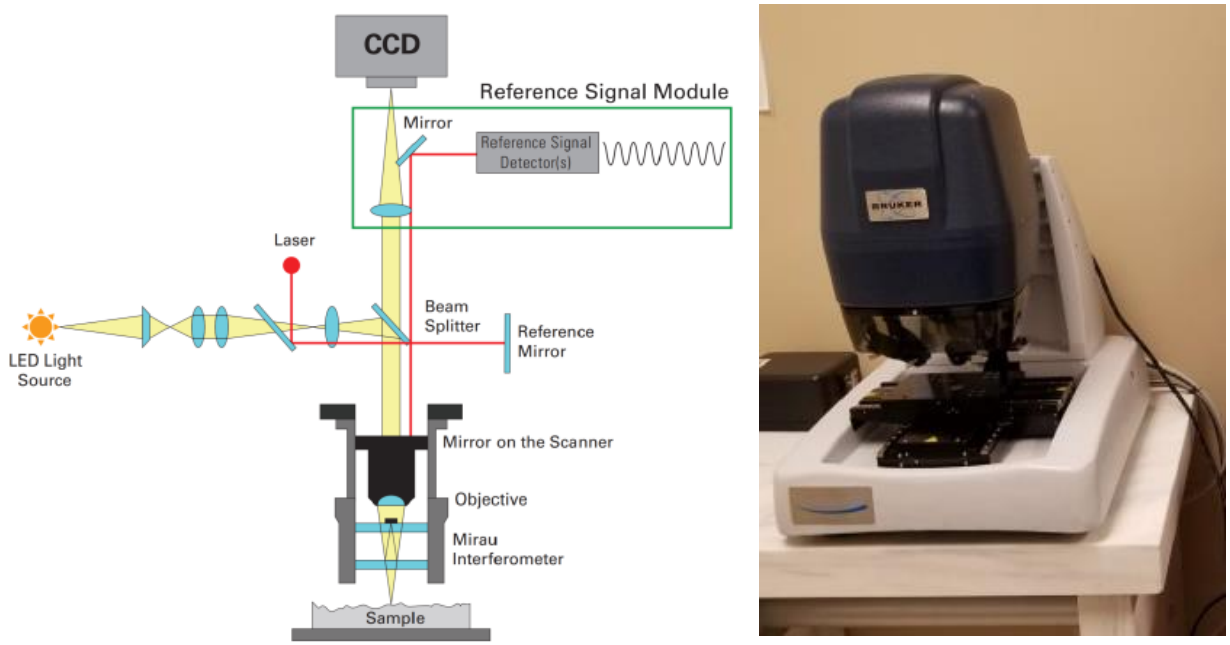

Figure 4.11. (a) Schematic of white interferometer principle, (b) Image of Bruker optical profiler [38]

As shown in Figure 4.11 (a), two beams are split into separate optical paths, which lead to a difference in the optical path length resulting a difference in phase. When those two beams are recombined, the constructive and destructive interference is produced generating a set of fringes with different spacing. This set of fringes are sensitive to change in height. Based on this white light interferometry principle, the optical profiler can characterize the vertical surface profile of samples. For the test of micromirrors, it is

suitable for the optical profiler to operate in a Vertical Scanning Interferometry (VSI) mode, which can handle abrupt steps and surface variations [38]. Using the VSI mode, the surface profile of the two samples; with and without the Si layer are obtained as pictured in Figure 4.12.

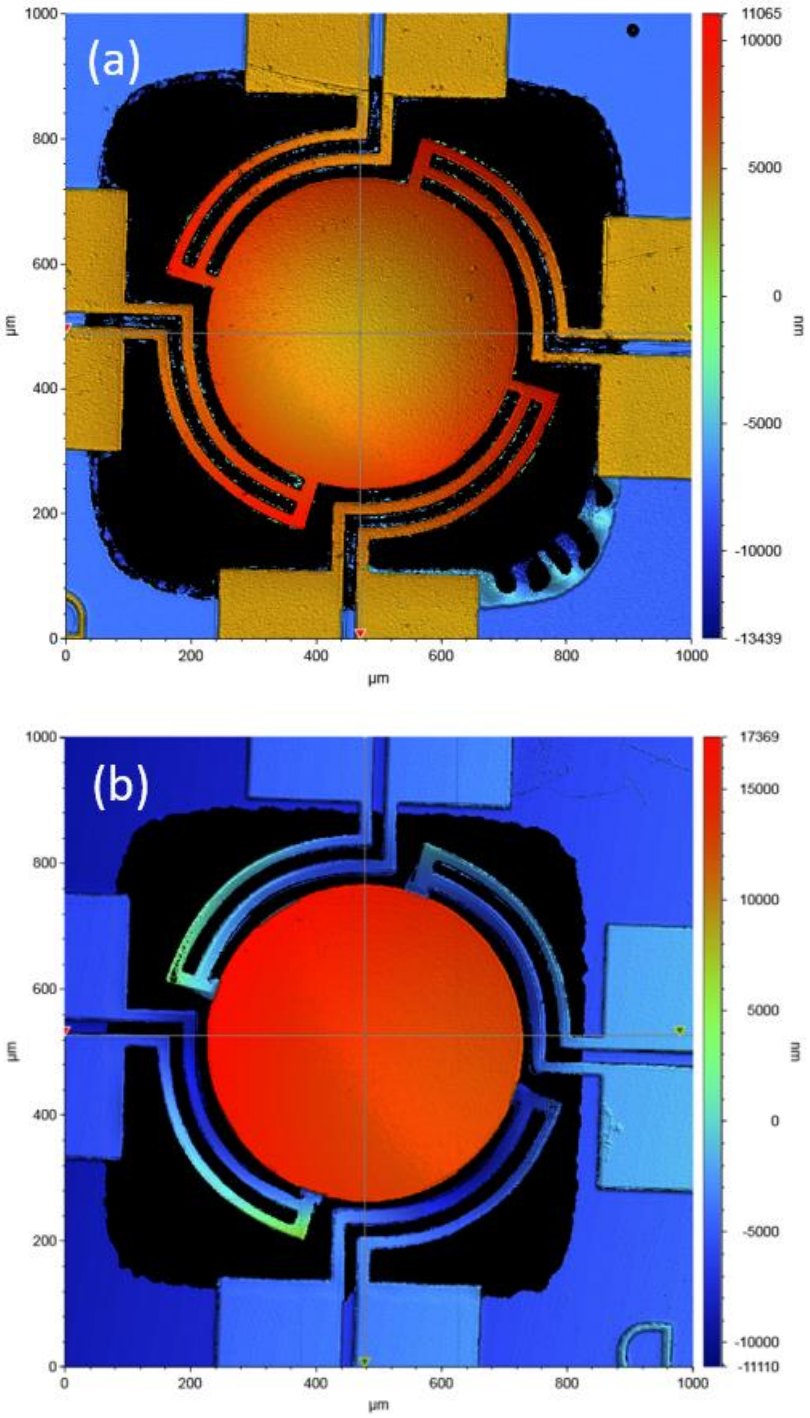

Figure 4.12. Surface profile of micromirror device, Design D, (a) without, (b) with Si layer

The profile images displayed in Figure 4.12 include the two axes in the centre of the mirrors. The plot in Figure 4.13 graphs the X and Y profiles along those axes including both with and without Si layer for comparison.

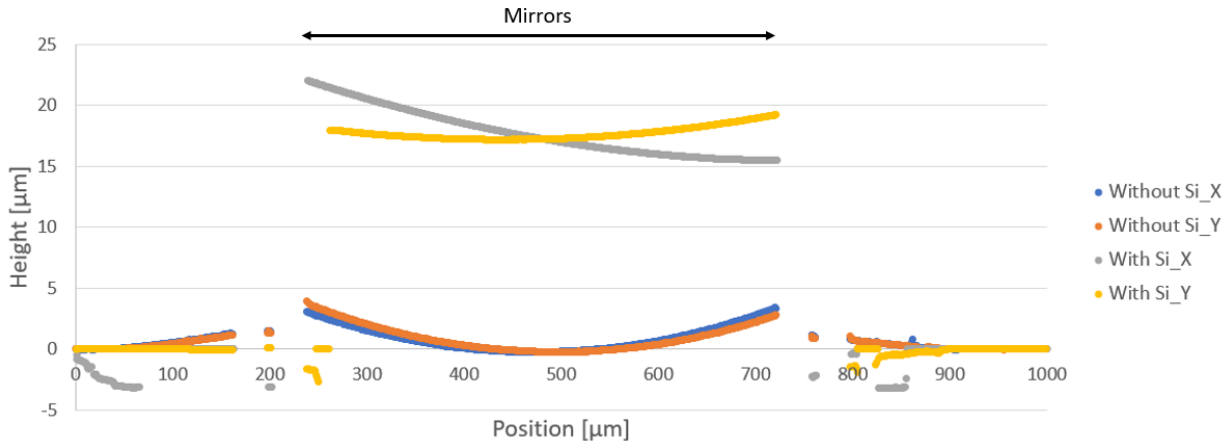

(a)

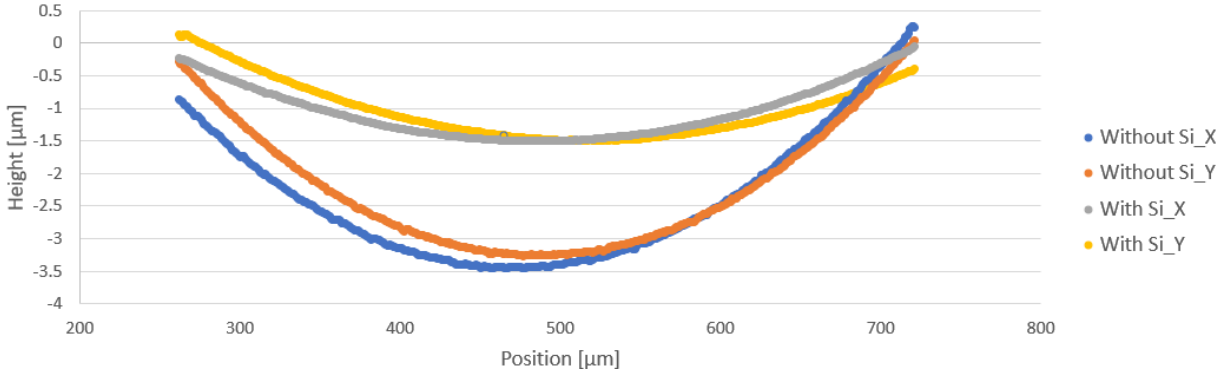

(b)

Figure 4.13. X and Y profiles, Design D, along the axes crossing at the centre of the mirror for without and with Si layer including (a) overall device, (b) mirror only

Figure 4.13 (a) includes the contact pads, the bimorph beams, and the mirrors as indicated on the plot. As the thickness of the silicon layer is 20 µm, the mirror with Si is lifted. The X profile suggests that the mirror even with Si layer is tilted. This does not necessarily imply that the mirror is curved. In fact, the mirror is tilted from non-uniformity of stress on the beams. In Figure 4.12 (b), the beams on the left side is more lifted than the right side. This is expected to improve with better alignment and uniformity during fabrication. To compare the flatness of the mirrors more closely disregarding the tilt, the data points for the mirror section is replotted with a two-point linear fit. As suggested in Figure 4.13 (b), the differences between the lowest and the highest points for without and with Si are approximately 1.5 µm and 3.5 µm, respectively. This concludes that the addition of silicon layer inhibits the curvature of the mirror caused

by residual stress from fabrication. It should also be noted that the mirror with 3 beams would curve more than the one with 4 beams as there is less constraints to the mirror. More results of optical profiler to study the effect of silicon layer can be found in Appendix.

After the investigation of the effect of the presence of the silicon layer, the surface profile of the micromirrors with the silicon layer is studied in a similar manner with the response to the voltage. One of the challenges in this study is delivering the voltage to samples while the samples are under the optical profiler because the profiler does not have a probe station as shown in Figure 4.11 (b). To properly apply actuation voltage on each device, the contact pads are wire bonded to an adapter, which can be mounted on a breadboard as described in Figure 4.14. Gold is used as the wire-bonding material to connect between the aluminum contact pads on the chip to the adapter.

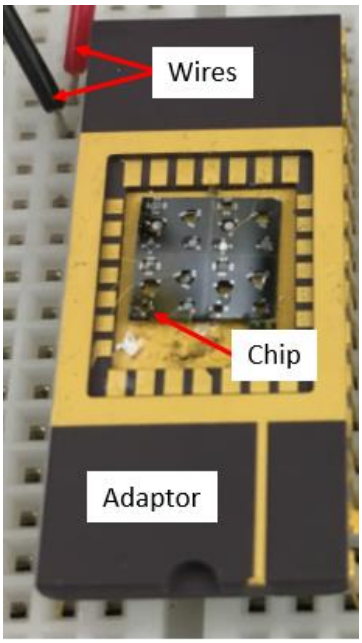

Figure 4.14. Image of chip wire-bonded to adapter mounted on breadboard for applying voltage

After wire-bonding, the wires are connected to the holes, on the breadboard, that correspond to the contact pads of the sample. Finally, DC voltage is applied to the wires to measure the actuation of the micromirrors with the optical profiler. The polarity does not matter for the bimorph actuation because the resistive heating does not depend on the polarity of the voltage as mentioned previously. To obtain the displacement of the mirror, the device without voltage is first scanned. Then, while the device remains in the same position, the DC voltage is applied. It is important to obtain the measurement at the off state to be used as reference. In Figure 4.15, the surface profiles of the micromirror device, Design D, are presented.

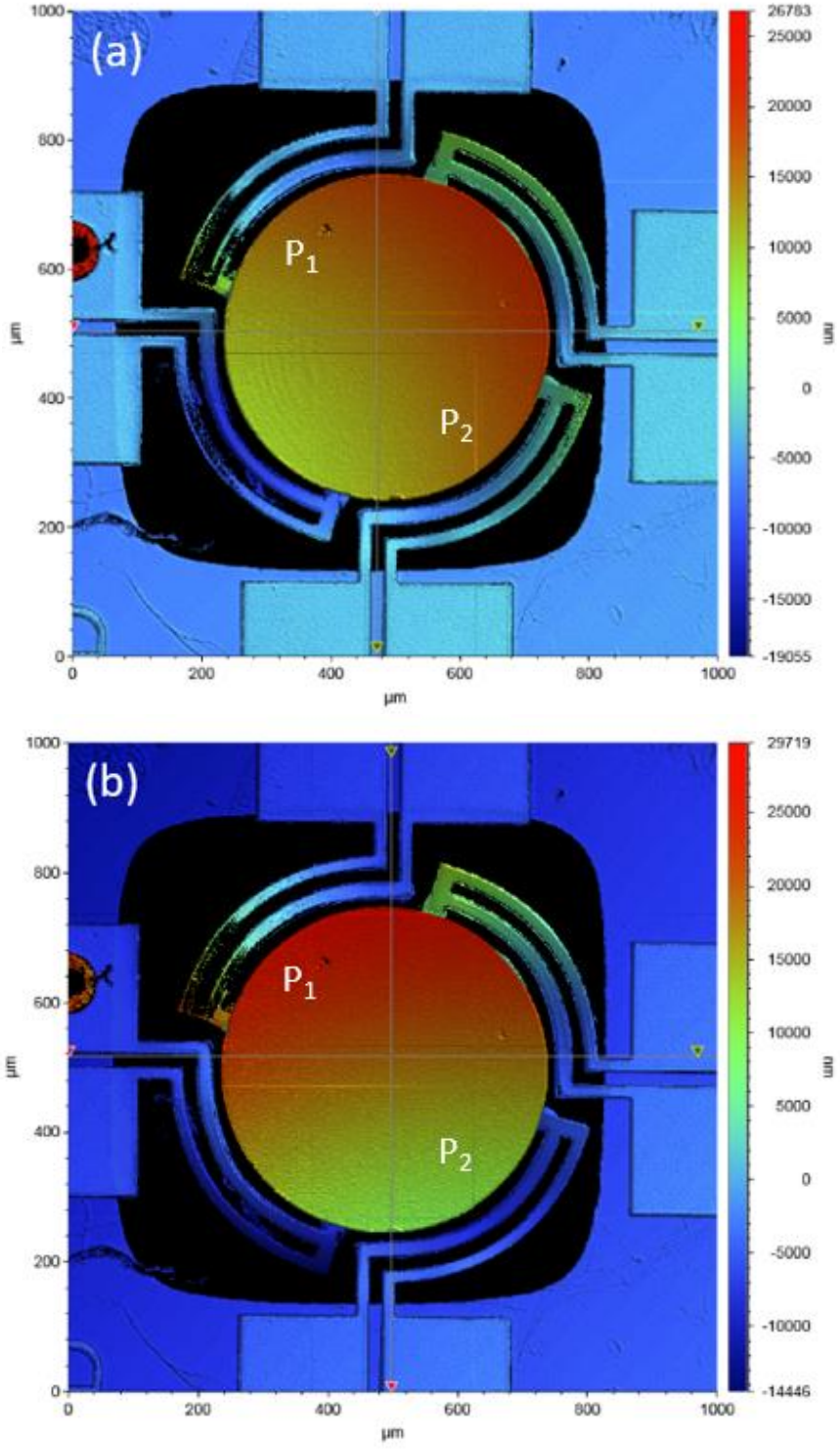

Figure 4.15. Surface profile of micromirror devices, Design D, (a) at off state, (b) with 0.5 V_{DC}

Figure 4.15 (a) without any applied voltage, the profile shows that the mirror is already slightly tilted due to non-uniformity from the beams. Then, 0.5 V_{DC} is applied on the pair of the electrodes on the left side of

the sample, which results in the downward displacement of the corresponding beam through resistive heating. To closely investigate the profile, like the graphs in Figure 4.13, the X and Y profiles are plotted along the axes crossing at the centre of the mirror as shown in Figure 4.16.

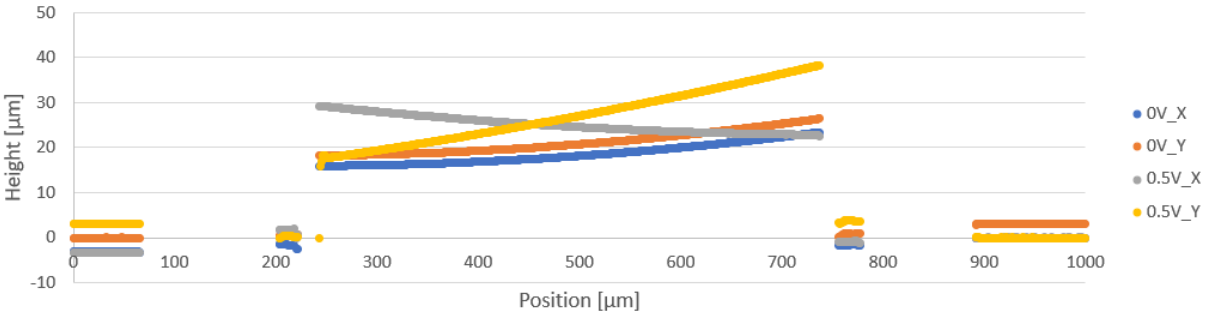

Figure 4.16. X and Y profiles, Design D, along the axes crossing at the centre of the mirror with response to applied voltage

As depicted in Figure 4.16, the mirror is tilted even without any voltage showing that the top right part of the mirror is lifted while the left bottom is lowered. With the voltage applied, it suggests that the top left, P_1, is raised while the bottom right, P_2, area is dropped. The vertical positions at P_1 and P_2 with 0.5 V_{DC} are 37 µm and 15 µm, and the ones without voltage, used as reference, are 21 µm and 19 µm, respectively. Therefore, the vertical displacement at the two points are 16 µm, and -4 µm resulting the total vertical displacement of 20 µm. These values can be converted to the equilibrium angle using a simple trigonometry and the diameter of the mirror as illustrated in Figure 4.17 and Equation (4.1).

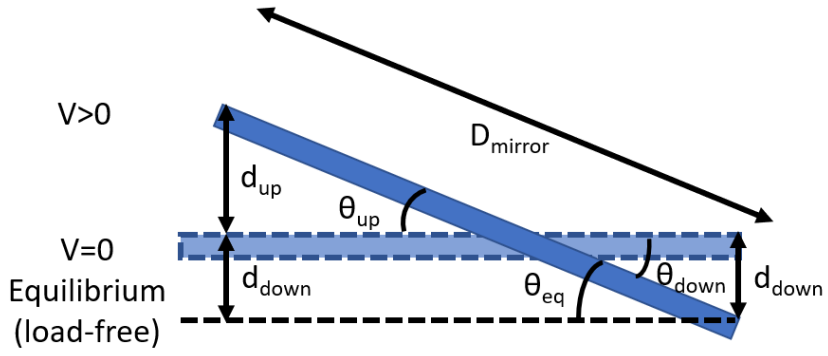

Figure 4.17. Schematic of micromirror showing the definitions of angular and linear displacements during on and off states

$$\theta_{eq} = \sin^{-1}\left(\frac{d_{up} + d_{down}}{D_{mirror}}\right) = \sin^{-1}\left(\frac{d_{total}}{D_{mirror}}\right) \quad (4.1)$$

As a result, the change of the tilt angle is 2.29° in response to 0.5 V_{DC}. It is also found that the initial tilt angle at off state using the above values is 0.23° and the tile angle with 0.5 V_{DC} is 2.52° as visualized in Figure 4.18. In addition, the axis of the maximum tilt angle of 0.69° for the off-state is shown in Figure 4.18 (a).

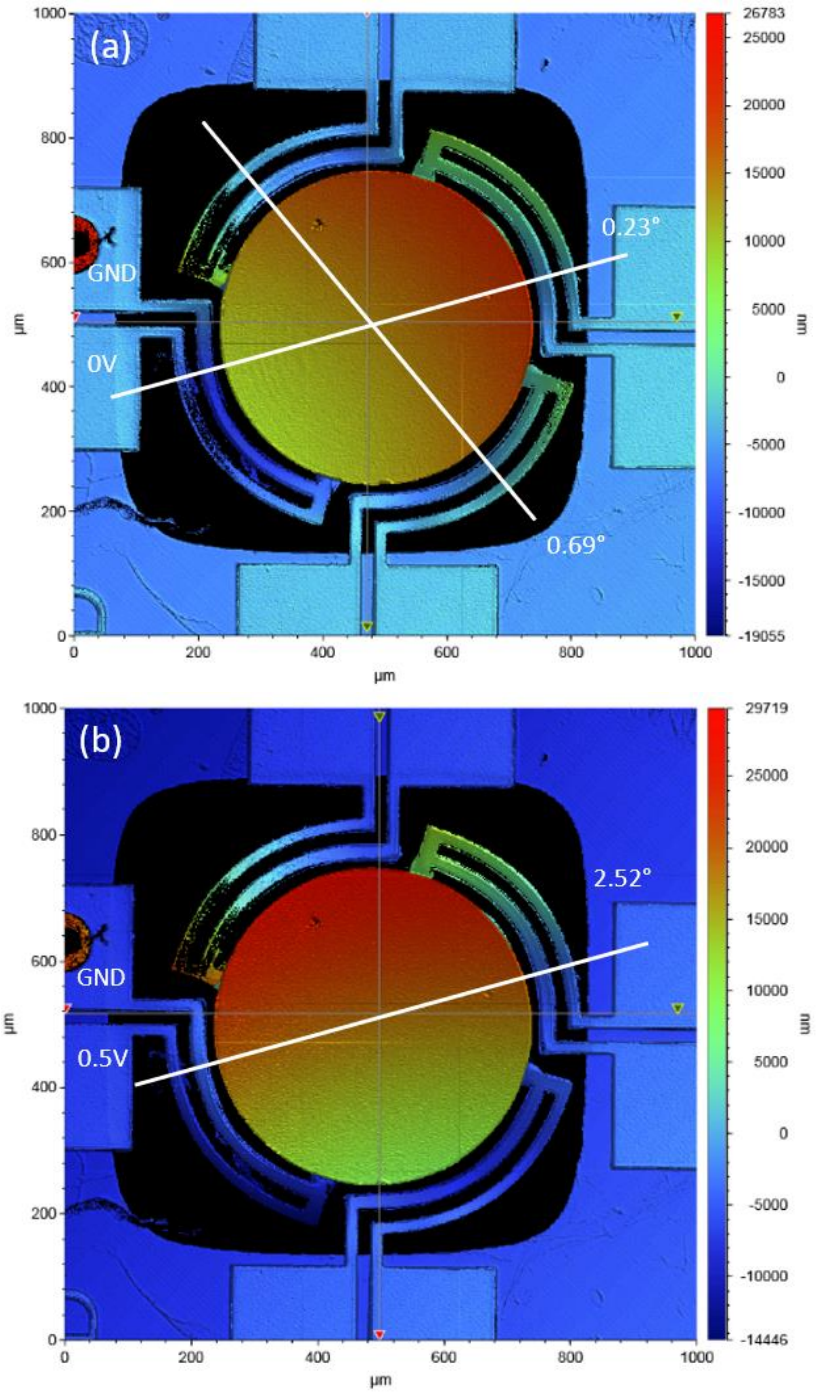

Figure 4.18. Tilt angle and axes of micromirror devices, Design D, (a) at off state, (b) with 0.5 V_{DC}

Finally, the mechanical angular displacement is obtained. However, in literature, there are several different terms to describe the angular displacement for micromirrors. It is important to signify the definition of the range of motion for both rotational and translational motion especially when comparing devices as data can be misleading if the measurement method is not clear. The range of motion in degrees can be represented in several different methods listed in Table 4.1 [2].

Table 4.1. Definitions of range of motion for rotational and translational motion

	Equilibrium Range	Full Range	Resonant amplitudes	Optical range
Definition	One extreme to equilibrium position	One extreme to the other extreme	Amplitude at a natural frequency	Range over reflection of light
Rotational	θ_{eq}	$\theta_{full} = 2\theta_{eq}$, if $\theta_{eq,up} = \theta_{eq,down}$	$\theta_{res} = \frac{\theta_{full} Q_\theta}{2}$	$\theta_{optical} = 2\theta_{full}$
Translational	d_{eq}	d_{full}	$d_{res} = \frac{d_{full} Q_d}{2}$	d_{full}

Table 4.1 suggests that the translational equilibrium range of motion is the range in piston DOF from the maximum distance that the mirror can move translationally to the equilibrium position without any load. Similarly, rotational equilibrium range of motion is the rotational range of motion from the maximum angle to the equilibrium position. Translational and rotational full range of motion are similarly determined except that it is from one extreme to the other extreme. If the devices can actuate to the same extent on both directions, full range of motion is twice of the equilibrium range of motion. These metrics are for analog or digital MEMS mirrors, which will be different in devices based on resonant approach. Resonant operation is not covered in this thesis but would be beneficial to explore in the future.

For Design D, it is possible to produce the rotational motion in two opposite directions due to the symmetric structure. This implies that the full range of rotational motion for Design D is approximately twice of the equilibrium range of rotational motion. Piston motion is possible for Design D and E, and the equilibrium range of translational motion is equal to the full range of translational motion as the mirror displaces downward with higher voltage. Another consideration is the axes of rotation, for Design A and D, including four sides where mirror can be directed, the axes of rotation are perpendicular to each other. On the other hand, the rotation axes of Design B, C, and E are 60° to each other, not perpendicular.

The rotation displacement of Design D, previously found with optical profiler, is 2.29°, which is the equilibrium range of rotational motion. Assuming the same displacement can be achieved by applying the same voltage on the opposite side of the mirror, the full range of rotational motion is 4.59°, and the optical range is 9.17° with 0.5 V_{DC}. The range of motion can surely increase with higher voltage.

However, during the experiment, the device has failed to operate when the voltage is raised to 1 V_{DC}. This could be due to disconnection from wire bonding or breakage of the beams due to stress and heat. Nevertheless, this does not agree with the previous validation with sinusoidal AC voltage, in which the device has shown actuation with 4 V_{ac} at 1 Hz and breaks down with 5 V_{ac}. To produce the same resistive heating effect for DC and AC voltage, the RMS value of a sinusoidal AC voltage need to equal the DC voltage [39], and 4 V of sinusoidal peak-to-peak AC voltage is equivalent to 1.41 DC voltage. In addition, the variation of dimensions among the samples also affect the heating of the bimorph, and the maximum applicable voltage. Therefore, more measurements would be helpful to study the consistency of the sample.

4.2.2. Experimental Validation

Considering that the maximum applicable voltage from the COMSOL simulation, shown in Figure 3.9, is 10 V_{DC} for Design D, the applicable voltage from the experiment is significantly lower. This is due to a couple of assumptions during the simulation, which could only be assessed experimentally. First assumption is that the heat transfer coefficient (htc) is 400 W/(m^2K) and 20000 W/(m^2K) for upper surface and other surfaces, respectively, using the values from literature [40]. The applicable voltage and the actuation are highly dependent on the heat transfer coefficient as the temperature significantly is influenced by this coefficient. It is also greatly challenging to estimate the values because heat transfer coefficient varies with numerous factors such as mechanical structure, surroundings, and the temperature of the sample itself. Secondly, the simulation is conducted with stress to account the residual stress from fabrication. Because the thermal properties of all the materials in the device are known, the direction of stress and bending can be predicted, but it is still difficult to determine the numerical value of it. The residual stress of the film is assumed to be 200 MPa uniformly and isotopically. This stress is approximated using the initial design by varying the stress and matching the displacement from fabrication and simulation. However, residual stress is influenced by number of factors such as process conditions and uniformity of a wafer, which cannot be easily predicted. There is always a variation of samples when the samples have processed together due to countless factors in microfabrication.

Despite the noticeable mismatch between the simulation and experimental results, the simulation can be corrected with iterative adjustments so that the new simulation can produce more accurate results for the next iterations. Additionally, the experimental results, in fact, demonstrate remarkably better outcome in

terms of required voltage. Experimentally for Design D, the total vertical displacement with 0.5 V_{DC} applied is 20 μm, which can achieve 9.17° in terms of the optical range of rotational motion. According to simulation, to accomplish the same vertical displacement, the required voltage is approximately 5 V_{DC}.

4.3. Summary

The microfabrication process and the mask layouts required for the proposed designs are highlighted. In the final process, some steps are modified and replaced due to fabrication issues. One of them involves patterning the aluminum layer on the frontside, which faces issues with removal of photoresist for dry etch or isotropic profile for wet etch. This is resolved by implementing the lift-off process. Secondly, the DRIE process is emphasized and the importance of it is justified. Lastly, residual stress from thermal expansion, which is a common problem in thin film fabrication, is explained. This problem is addressed by an additional thick silicon layer from an SOI wafer, which keeps the mirror flat. In conclusion, the final microfabrication process resolves the mentioned problems and assures the fabrication feasibility of the proposed micromirror device. The completed micromirror devices are visualized through the SEM images convincing that the flatness of the mirror can be enhanced by the additional silicon layer. In addition, the tilt motion of the mirrors with applied voltage is verified under the optical microscope and quantified with the optical profiler. The presented data for Design D suggest that the total vertical displacement of 20 μm can be accomplished with the actuation voltage of 0.5 V_{DC} which is equivalent to 9.17° in terms of optical range of rotational motion. Despite the disagreement with the simulation due to a couple of assumptions, the required voltage experimentally acquired is significantly lower than the simulated voltage, 5 V_{DC}.

Chapter 5. Conclusion

5.1. Summary of Research

This thesis can be summarized into the following three main topics:

1. Designs of SOI-based micromirrors, that are thermally actuated with Al/SiO_2 bimorph structures, are proposed with advantages of simpler fabrication method. Based on simulation, the micromirrors show capability of producing three DOF including tip, tilt, and piston motion. Simulation results with various alternative materials for the bilayer suggest that aluminum and silicon dioxide are the most suitable choice for providing larger displacement, high reflectivity, and fabrication compatibility. Dimensional sweep has been simulated as well showing the trade offs of dimensional parameters of the device.
2. The proposed designs are successfully fabricated, and the fabrication process is introduced. Some of the essential processes such as Bosch process and lift-off method are highlighted. The issue of residual stress from thermal mismatch during fabrication are addressed by taking advantage of device silicon layer from an SOI wafer.
3. The fabricated micromirror devices are first validated with optical microscope from a top view while voltages are applied. The SEM images of them show the off state micromirrors. Finally, the micromirror devices are characterized with the optical profiler using white light interferometry mode. There are still disadvantages and limitations of the devices. One of the disadvantages is the challenge in fabrication as the Al and SiO_2 are very thin, which may require robustness and also cause non-uniformity in dimensions after the release. In addition, compared to the other thermally actuated micromirror introduced, the tilt angle is not as large. Despite these limitations, the fabrication process has been greatly simplified with only 3 masks reducing the cost of the device, and the actuation voltage is much lower than the previous micromirrors. The results from the optical profiler show that the achievable optical range is 9.17° with 0.5 V_{DC}. These numbers convince that the micromirror device in this work is a promising approach.

5.2. Future Work

The future work of this research includes the following:

1. Further characterization and validation of other designs using a surface profiler.
2. Dynamic analysis and testing of micromirror have not been completed. It would be beneficial to understand the device performance at various frequencies including the resonant frequency.
3. Simulation of the design with adjusted constants for more accurate prediction of actuation.

Reference

[1] Petersen, K. E. (1980). “Silicon Torsional Scanning Mirror,” IBM Journal of Research and Development, vol. 20(5), pp. 631-637 doi:10.1147/rd.245.0631
[2] Song, Y., Panas, R. M., & Hopkins, J. B. (2018). “A review of micromirror arrays,” Precision Engineering 51, pp. 729-761
[3] Prime Faraday Partnership. (2002). “An Introduction to MEMS (Micro-electromechanical Systems),” Loughborough University, http://www.primetechnologywatch.org.uk
[4] Thielicke, E., & Obermeier, E. (2000). “Microactuator and their technologies,” *Elsevier Science Mechatronics,* vol. 10, Issues. 4-5, pp. 431-455 doi.org/10.1016/S0957-4158(99)00063-X
[5] Hiroyuki, F. (1998). “Microactuators and Micromachines,” *Proceedings of IEEE,* vol. 86, no. 8, pp. 1721-1732 doi: 10.1109/5.704278
[6] Bell, D.J., Lu, T.J., Fleck, N.A., & Spearing, S.M. (2005). “MEMS actuators and sensors: observations on their performance and selection for purpose,” Journal of Micromech. Microeng, vol. 15, S153-S164 doi: 10.1088/0960-1317/15/7/022
[7] Livermore, C. (2007). “6.777J / 2.372J: Design and Fabrication of Microelectromechanical Devices,” [Course Presentation]. Retrieved from MIT OpenCourseWare: https://ocw.mit.edu/courses/electrical-engineering-and-computer-science/6-777j-design-and-fabrication-of-microelectromechanical-devices-spring-2007/lecture-notes/07lecture21.pdf
[8] Kumar, C. (2015, October 8). “Modeling Microresonators with Electrostatic Actuation,” Retrieved from https://www.comsol.com/blogs/modeling-microresonators-with-electrostatic-actuation/
[9] Vaxevanidis, N. M., Vortselas, A. K., Koutsomichalis, A., & Petropoulos, G. (2010). “Advances in micro-manufacturing applying tribological principles,” Journal of the Balkan Tribological Association, vol. 16, no. 2, 161-179
[10] Dechev, N. (n.d). “MECH 466: Lecture 5: Electrostatic Sensors and Actuators,” [Course Presentation]. Retrieved from https://www.engr.uvic.ca/~mech466/MECH466-Lecture-5.pdf
[11] Boussey, J. (2003). “Microsystems Technology: Fabrication, Test & Reliability,” London, UK: Kogan Page. Retrieved from https://www.globalspec.com/reference/70614/203279/3-comb-drive-actuator
[12] Dechev, N. (n.d). “MECH 466: Lecture 8: Thermal Sensors & Actuators,” [Course Presentation]. Retrieved from https://www.engr.uvic.ca/~mech466/MECH466-Lecture-8.pdf
[13] Adams, T.M., & Layton R. A. (2010). “Introductory MEMS Fabrication and Applications,” New York, NY: Springer doi 10.1007/978-0-387-09511-0
[14] Buttgenbach, S. (2014). “Electromagnetic Micromotors – Design, Fabrication and Applications,” MDPI-Micromachines 5, 929-942 doi:10.3390/mi5040929
[15] Dempsey, N. M. (n.d.). "Magnetic MEMS," The European Magnetism Association, Retrived from http://magnetism.eu/esm/2007-cluj/abs/Dempsey2-abs.pdf
[16] Arnold, D. P., & Wang, N. (2009). "Permanent Magnets for MEMS," Journal of Microelectrochemical Systems, vol. 18, no. 6, 1255-1266
[17] Korvink, J.G., & Paul, O. (2006). “MEMS a practical guide to design, analysis and applications,” Springer doi: 10.1007/978-3-540-33655-6
[18] Weinberg, M. S. (1999). “Working Equations for Piezoelectric Actuators and Sensors,” Journal of Microelectromechanical systems, vol. 8, no. 4, pp. 529-533 doi: 10.1109/84.809069
[19] Lee, B. (2008) – revised (2018). “Introduction to +/-12 Degree Orthogonal Digital Micromirror Devices (DMDs),” Texas Instruments. Retrieved from http://www.ti.com/lit/an/dlpa008b/dlpa008b.pdf
[20] Silva, G. et al. (2015). “Optical Detection of the Electromechanical Response of MEMS Micromirrors Designed for Scanning Picoprojectors,” IEEE Journal of Selected Topics in Quantum Electronics, vol. 21, no. 4, 2800110

[21] Jia, K., Samuelson, S.R., & Xie, H. (2011). “High-Fill-Factor Micromirror Array with Hidden Bimorph Actuators and Tip-Tilt-Piston Capability,” Journal of Microelectromechanical Systems, vol. 20, no.3, 573-582
[22] Aoyagi, I. et al. (2011). “2-Axis MEMS Scanner for a Laser Range Finder,” IEEE 16th International Conference on Optical MEMS and Nanophotonics, pp. 39-40.
[23] Baran, U. et al. (2012). “Resonant PZT MEMS Scanner for High-Resolution Displays,” Journal of Microelectrochemical Systems, vol. 21, no. 6, 1303-1310
[24] Sakurai, T., Matsuzawa, A., & Douseki, T. (2006). “Fully-Depleted SOI CMOS Circuits and Technology for Ultralow-Power Applications,” Springer doi: 10.1007/978-0-387-29218-2
[25] Laconte, J., Flandre, D., & Raskin, J. (2006) “Micromachined Thin-Film Sensors for SOI-CMOS Co-Integration,” Springer doi: 10.1007/0-387-28843-0
[26] Janwadkar, S. (2017) “SOI Silicon on Insulator Technology,” Retrieved from https://www.slideshare.net/shudhanshu29/silicon-on-insulator-soi-technology
[27] https://soiconsortium.org/2011/03/25/soi-for-mems-a-promising-material/
[28] Fedder, G.K., Howe, R. T., Liu, T.K.,, & Quevy, E.P. (2008). “Technologies for Cofabricating MEMS and Electronics”, In Proceedings of the IEEE International Conference on Micro Electro Mechanical Systems (MEMS), vol. 96, no. 2, pp. 306-322 doi: 10.1109/JPROC.2007.911064
[29] SOI Industry Consortium. (n.d.). “MEMS on SOI – Growing Fast and Faster,” Retrieved from https://soiconsortium.org/2011/04/06/mems-on-soi-growing-fast-and-faster/
[30] Filipovic, L. (2012). “Topography Simulation of Novel Processing Techniques,” (Doctoral dissertation). Retrived from http://www.iue.tuwien.ac.at/phd/filipovic/node26.html
[31] The Engineering ToolBox. (n.d). “Thermal Expansion of Metals,” Retrieved from https://www.engineeringtoolbox.com/thermal-expansion-metals-d_859.html
[32] The Engineering ToolBox. (n.d.). “Metals – Melting Temperatures,” Retrieved from https://www.engineeringtoolbox.com/melting-temperature-metals-d_860.html
[33] Goncalves, A. D. (2019). “Metallic Reflection,” Retrieved from https://eng.libretexts.org/Bookshelves/Materials_Science/Supplemental_Modules_(Materials_Science)/Optical_Properties/Metallic_Reflection
[34] Laseroptik. (n.d.). “Metal coatings,” Retrieved from https://www.laseroptik.de/en/coatings/metal-coatings
[35] Accuratus. (n.d.). “Silicon Nitride, Si_3N_4 Ceramic Properties,” Retrieved from https://www.accuratus.com/silinit.html
[36] Accuratus. (n.d.). “Aluminum Oxide, Al_2O_3 Ceramic Properties,” Retrieved from https://www.accuratus.com/alumox.html
[37] Otmar, E., & Selberherr, S. (2010). “Three-dimensional level set based Bosch process simulations using ray tracing for flux calculation,” Elsevier, Microelectronic Engineering, vol. 87, issue. 1, pp. 20-29 doi.org/10.1016/j.mee.2009.05.011
[38] Gibson, S. (2019). “Bruker Contour GT-1 Optical Profiler” [Standard Operating Procedure]. Retrieved from https://fab.qnc.uwaterloo.ca/equip/rac2-bruker-contour/manuals/internal/2012-10-11_ContourGT-IUser.pdf/view
[39] Aspencore. (n.d.). “RMS Voltage Tutorial,” Retrieved from https://www.electronics-tutorials.ws/accircuits/rms-voltage.html
[40] Ivanova, R. (2016). “NE 454B Nanoelectronics Winter 2016 Lab Manual,” [Course Presentation]. Retrieved from https://learn.uwaterloo.ca

Appendices

Appendix A – Mask Layout of each Design

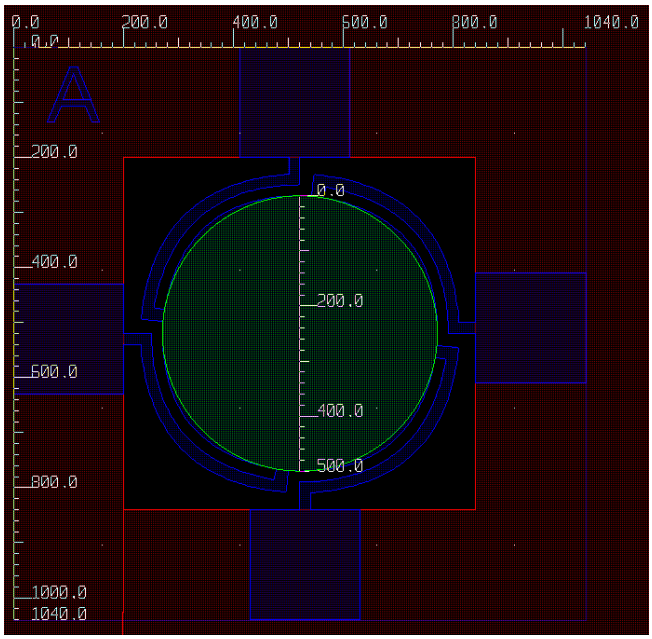

(a) Design A

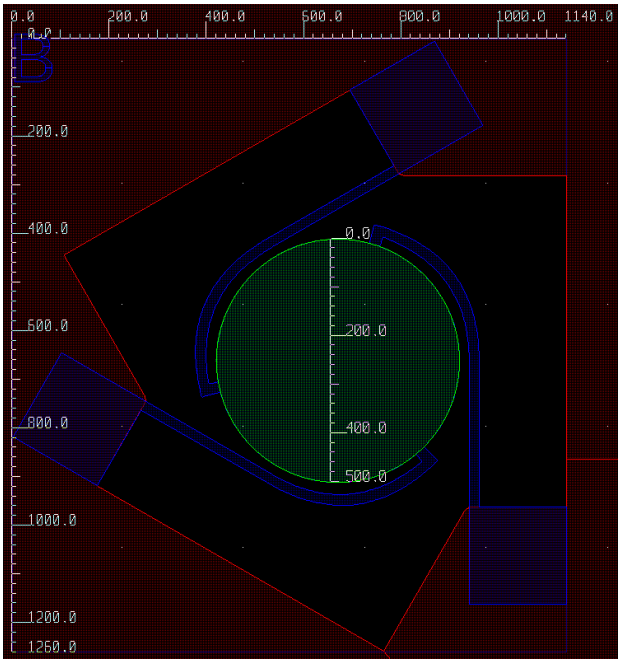

(b) Design B

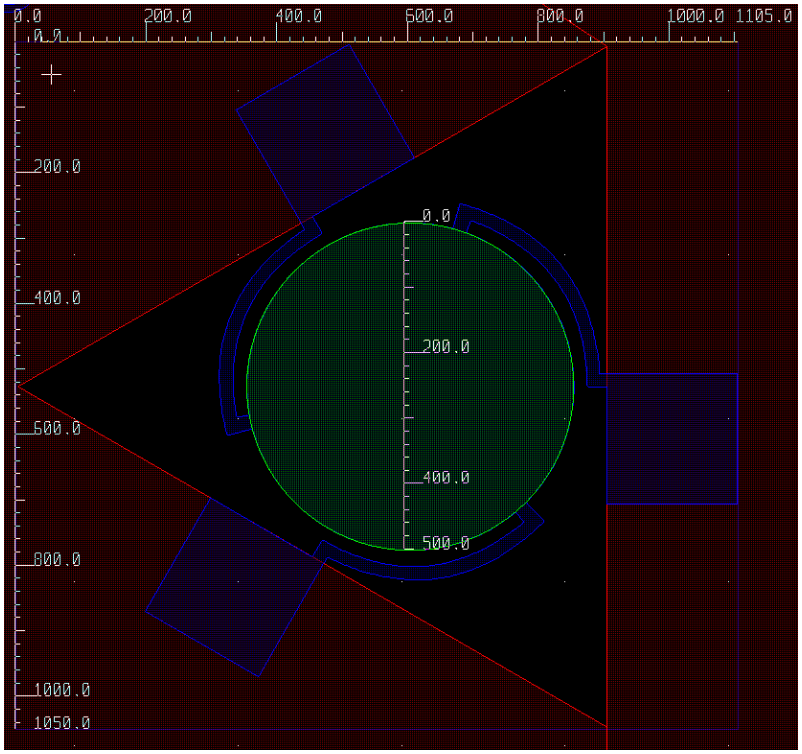

(c) Design C

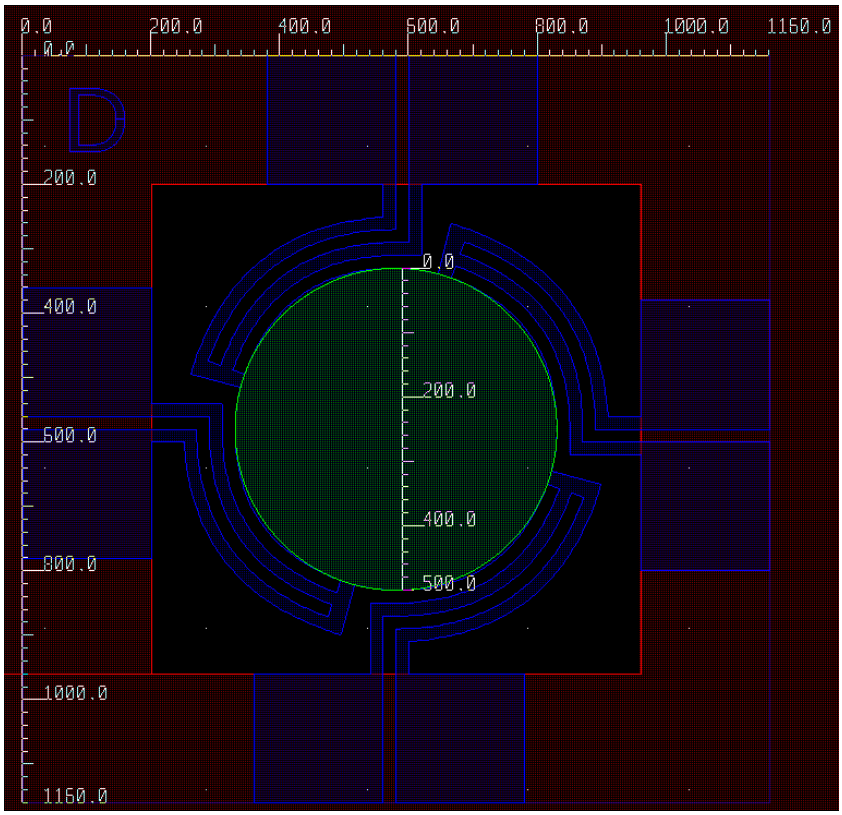

(d) Design D

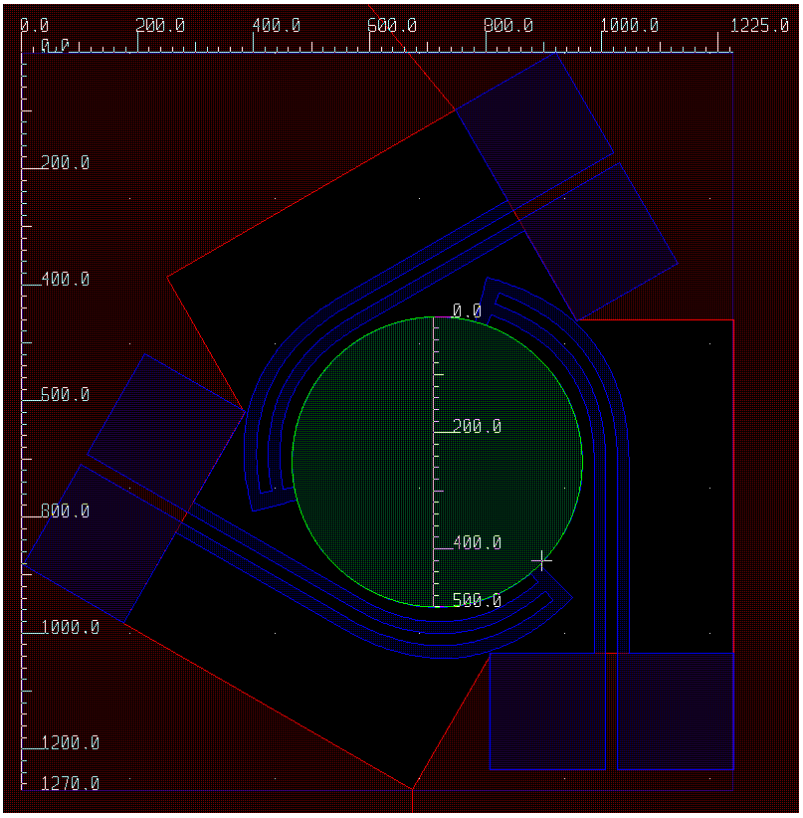

(e) Design E

Figure A.1. Mask layout of each design with the total length and width including the contact pads

Appendix B – Surface Profile without and with Si layer

The purpose of Appendix B is to provide the surface profiles of other designs, comparing the devices without and with Si layer, as the experiment results section mainly highlights on Design D.

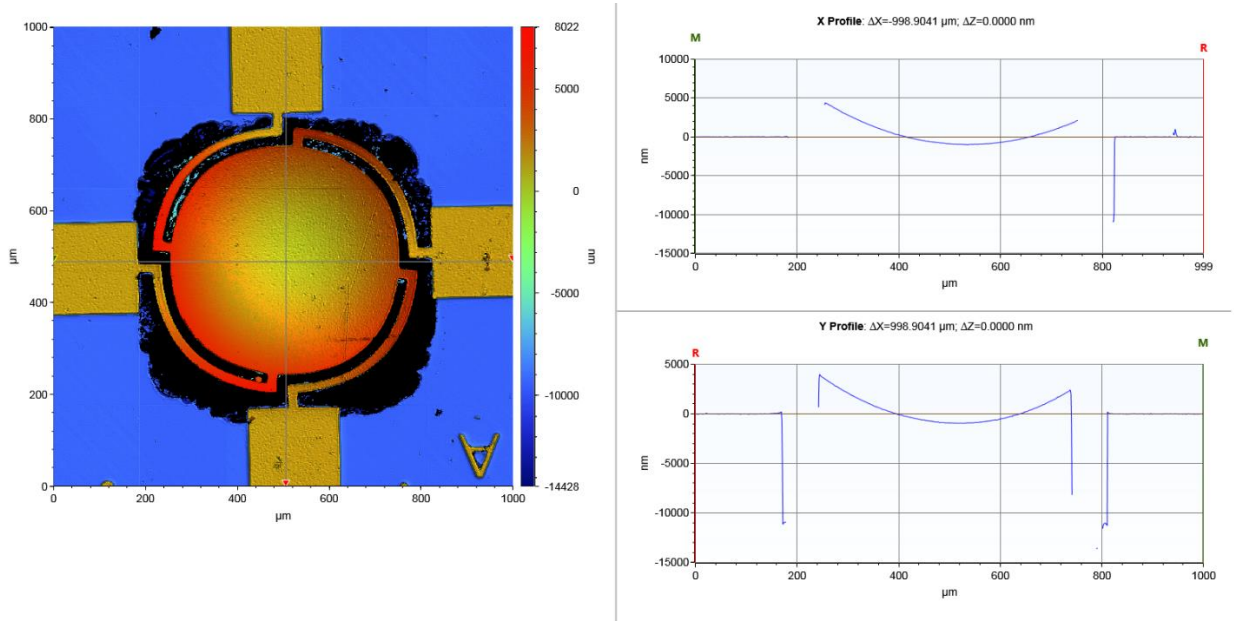

(a)

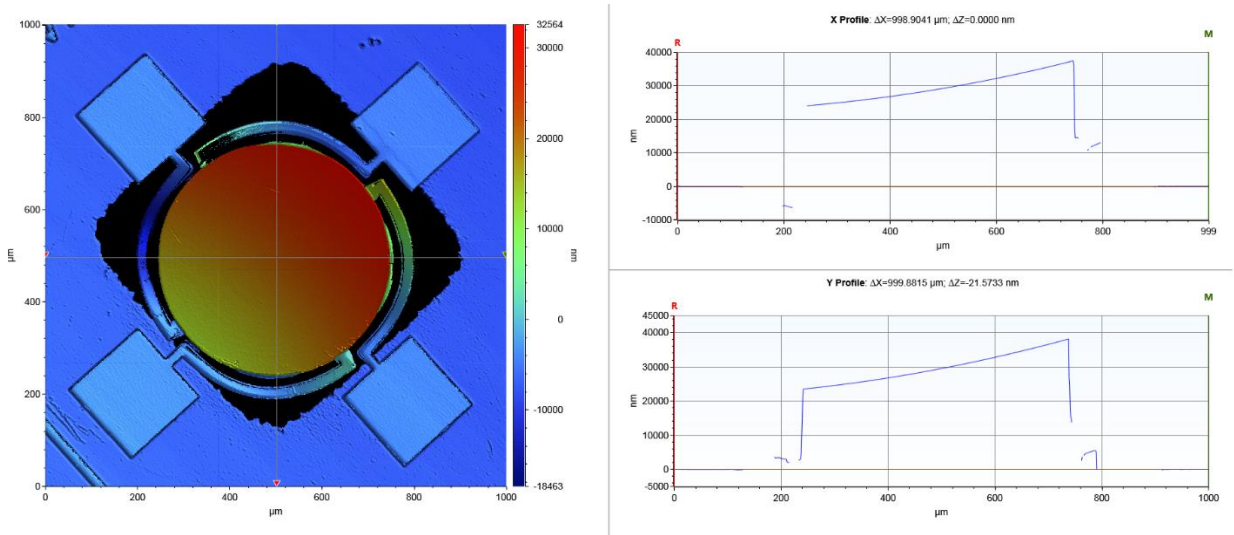

(b)

Figure B.1. Surface profile of Design A (a) without, (b) with Si layer

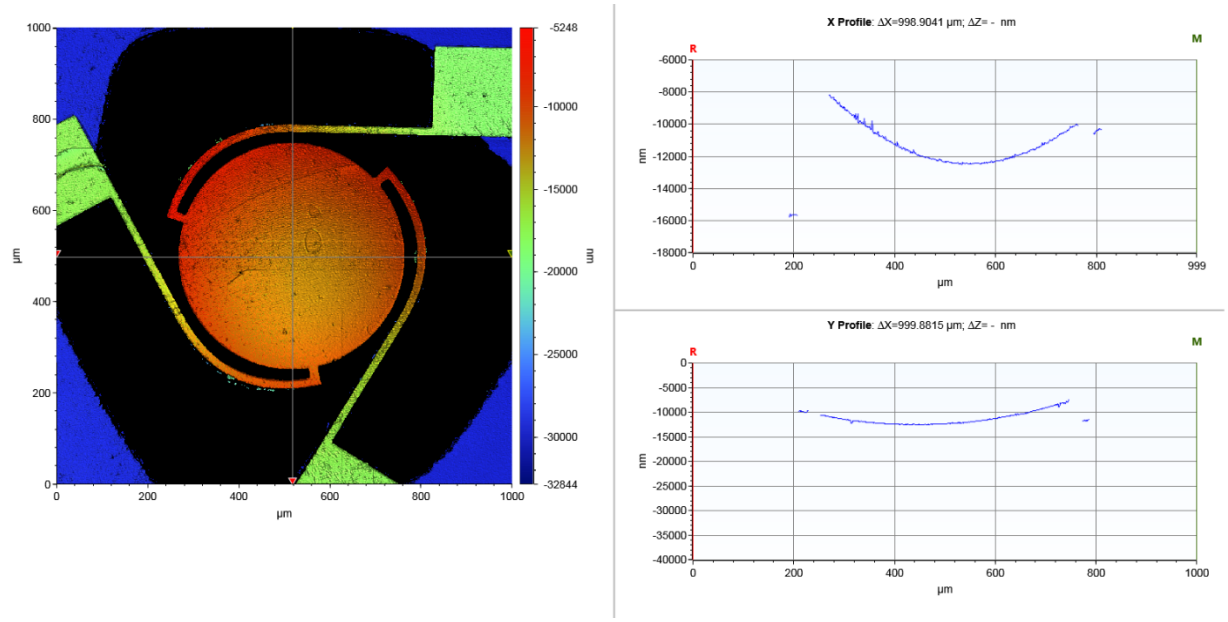

(a)

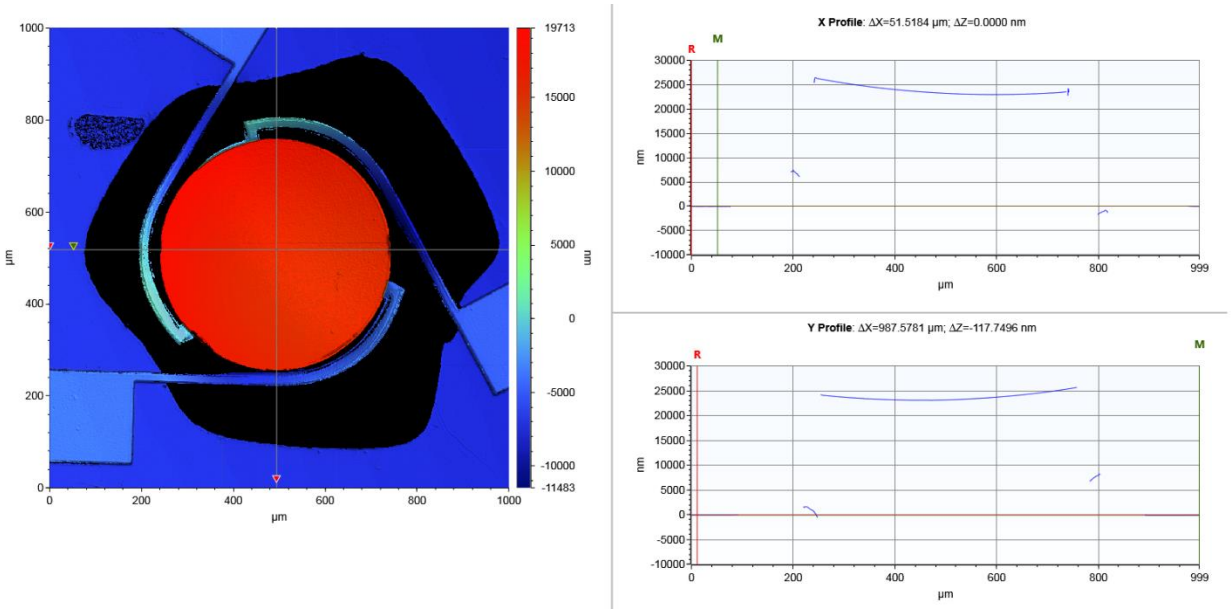

(b)

Figure B.2. Surface profile of Design B (a) without, (b) with Si layer

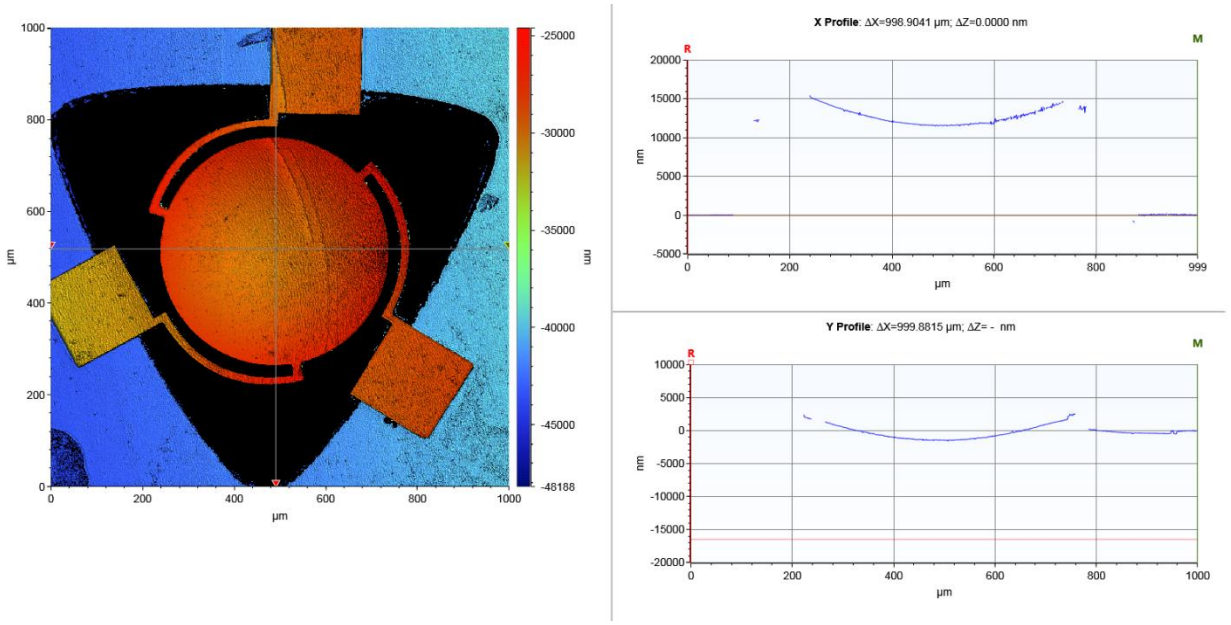

(a)

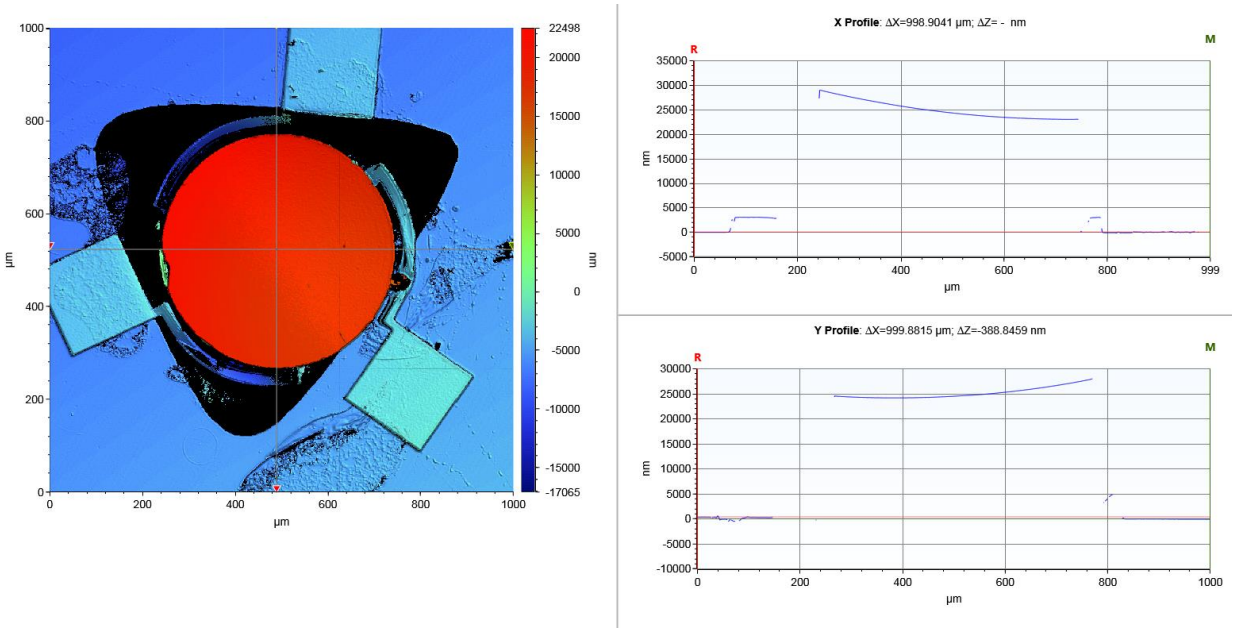

(b)

Figure B.3. Surface profile of Design C (a) without, (b) with Si layer

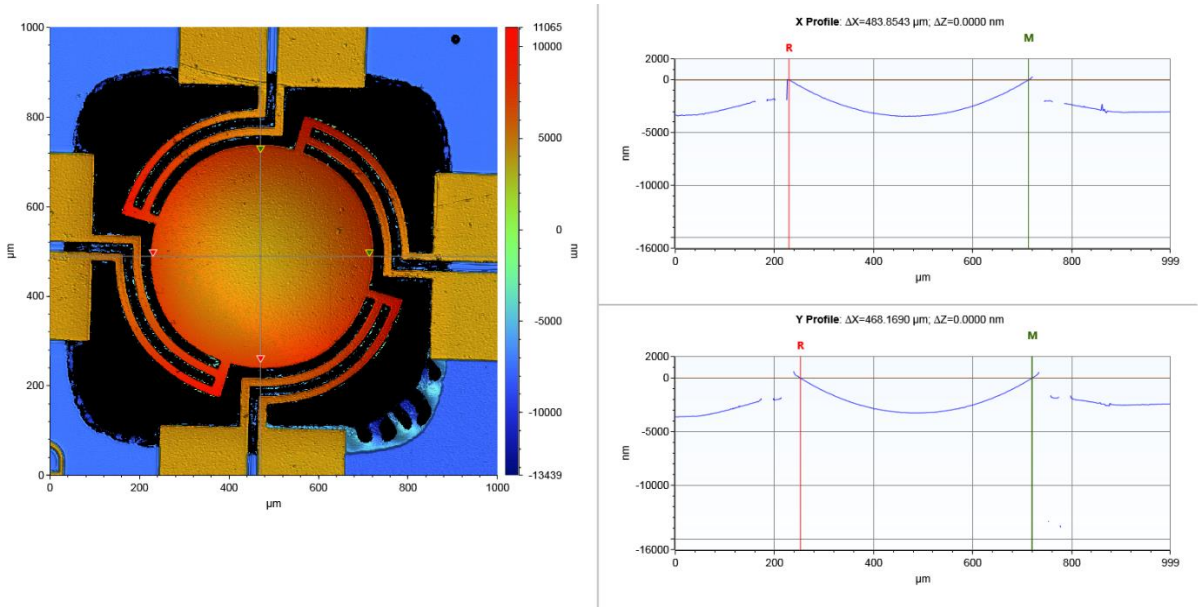

(a)

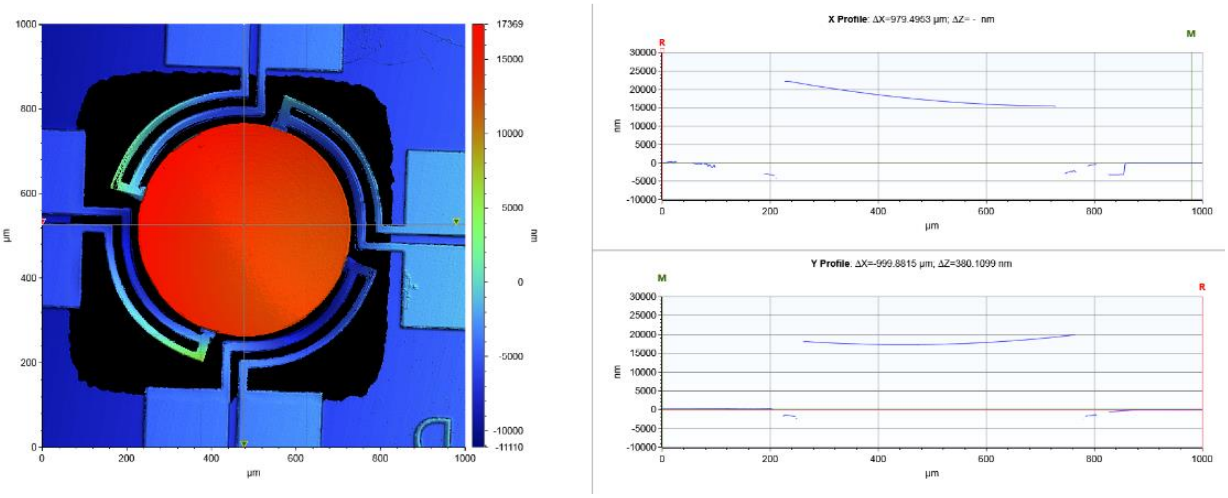

(b)

Figure B.4. Surface profile of Design D (a) without, (b) with Si layer

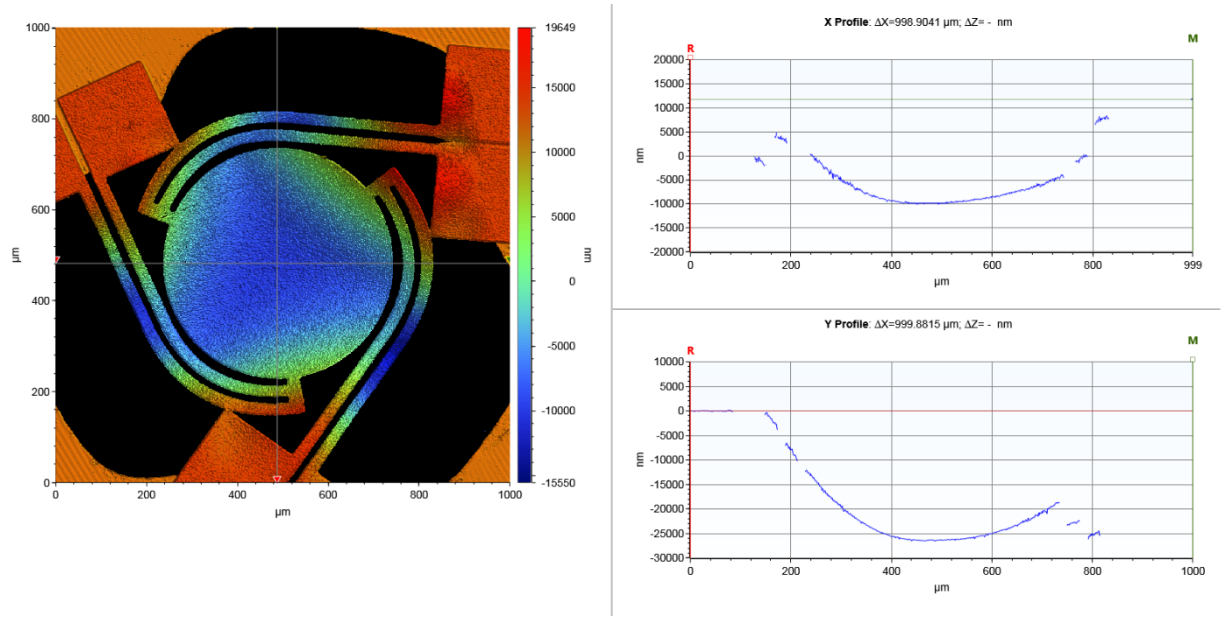

(a)

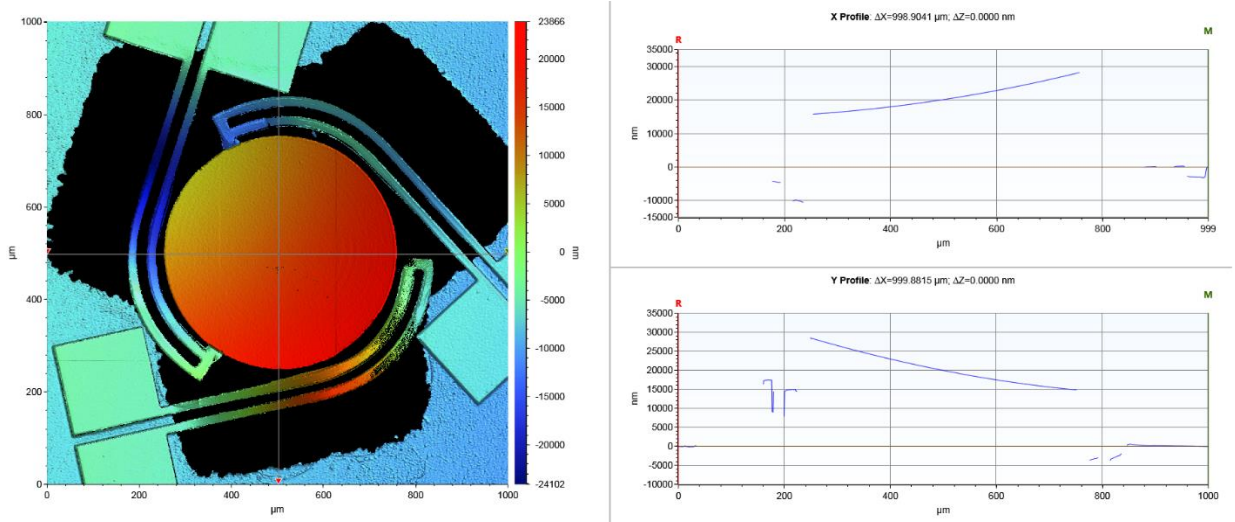

(b)

Figure B.5. Surface profile of Design E (a) without, (b) with Si layer

As the above Figures show, the mirror is much more curved without the Si layer suggesting that the thick silicon layer will enhance the flatness of the mirror surface. Some designs with three actuators, as opposed to four, show that the mirror is tilted after release although the surface is flat. This is due to the asymmetry of structure as mentioned in Chapter 4. For instance, Design E in Figure B.5, two beams are lowered due to residual stress while the other beam (the bottom one) is lifted upward resulting significant tilt of the mirror even at off state.